Collective dynamics of molecular motors and passive cross-linkers on microtubules

Dissertation

zur Erlangung des Grades
des Doktors der Naturwissenschaften
der Naturwissenschaftlich-Technischen Fakultät II
- Physik und Mechatronik -
der Universität des Saarlandes
von

Denis Johann

Saarbrücken, 2015

Tag des Kolloqiums:	10.06.2016
Dekan:	Univ.-Prof. Dr. Georg Frey
Mitglieder des	Univ.-Prof. Dr. Dr. Karsten Kruse
Prüfungsausschusses	Univ.-Prof. Dr. Ludger Santen
	Univ.-Prof. Dr. Albrecht Ott
	Dr. Andreas Christ

Hiermit versichere ich an Eides statt, dass ich die vorliegende Arbeit selbstständig und ohne Benutzung anderer als der angegebenen Hilfsmittel angefertigt habe. Die aus anderen Quellen oder indirekt übernommenen Daten und Konzepte sind unter Angabe der Quelle gekennzeichnet. Die Arbeit wurde bisher weder im In- noch im Ausland in gleicher oder ähnlicher Form in einem Verfahren zur Erlangung eines akademischen Grades vorgelegt.

Saarbrücken, 13.06.2016

Denis Johann

Abstract

Understanding how biological cells grow and divide is a major interest of biophysical research. One aspect is the self-organization of the cytoskeleton, a dynamic assembly consisting of biological filaments as well as other proteins, that generates essential structures for the proliferation of cells.

A prominent example in this context is the mitotic spindle formed during cell division, which is vital in eukaryotes, for instance by defining the division site. It is built of overlapping microtubules that steadily grow and shrink. Nonetheless, due to proteins regulating the length of filaments and the overlap between them, the spindle size is well defined. While filament length regulation was studied before, the overlap dynamics are still poorly understood.

After introducing the main components of the cytoskeleton and presenting past research on sterically interacting particles and overlapping filaments, we show that diffusive and directionally moving particles segregate along a filament under steric interactions. If these particles generate cross-links between antiparallel microtubules, they are able to generate stable partial overlaps, with or without steric interactions, that are in agreement with experimental results. Based on the understanding of overlap regulation between filament pairs, a coarse-grained theory for filament bundles is derived, reproducing essential features of the spindle.

Parts of this work have already been published [1, 2].

Zusammenfassung

Das Hauptinteresse biophysikalischer Forschung ist das Verständnis der Funktionsweise von Zellen, der Basis aller lebenden Organismen. Ein wichtiger Aspekt zum Verständnis von Zellen ist deren Lebenszyklus, während dessen das Zytoskelett, also biologische Filamente mit assoziierten Proteinen, Strukturen wie den Spindelapparat erzeugt. Letzterer bestimmt unter anderem die Ebene der Zellteilung und besteht aus sich überlappenden Mikrotubuli, die stetig wachsen und schrumpfen. Dennoch ist die Größe der Gesamtstruktur durch Proteine, welche Länge und Überlapp der Filamente regulieren, stabilisiert. Während Längenregulation von Filamenten bereits untersucht wurde, ist das Verständnis der Überlappdynamik noch lückenhaft.

Nach der Vorstellung der Bestandteile des Zytoskeletts und bereits bekannter Phänomene wechselwirkender Partikel und überlappender Filamenten zeige ich, dass sterisch wechselwirkende, diffusive und gerichtet bewegte Partikel sich entlang eines Filaments in zwei Phasen trennen. Verbinden diese Partikel antiparallele Filamente, so können sie stabile Überlappe erzeugen, sowohl mit als auch ohne sterische Wechselwirkung zwischen den Spezies. Die Ergebnisse der Simulationen sind im Einklang mit Experimenten. Basierend auf der Analyse der Interaktion zweier Filamente wird eine vergröberte Theorie für Filamentbündel entwickelt, welche wesentliche Charakteristika von Spindeln reproduzieren kann.

Teile dieser Arbeit wurden bereits veröffentlicht [1, 2].

Contents

Chapter 1

The cytoskeleton can self-organize into structures

Living biological cells are complex multicomponent systems [3–5] and an important fundamental structure allowing cells to react to their surrounding environment is the cytoskeleton [6]. It is a network of biological string-like polymer-chains called filaments, interacting with numerous other proteins and molecules under the consumption of chemical energy. This energy is usually stored as energy rich triphosphate compounds. The cytoskeleton is therefore highly dynamic and out of thermodynamic equilibrium, hence non-equilibrium physical methods need to be applied to describe the structure's properties and functionality.
In the first chapter of this work, we present some of the molecular components of the cytoskeleton and the structures formed, which are relevant to understand the effects studied in our research.

1.1 Filaments are the main components of the cytoskeleton

The principal components of the cytoskeleton are biological filaments, where one distinguishes between actin filaments, microtubules and intermediate filaments. These filaments may serve as tracks for cellular transport of organelles [5, 7]. On top of that, their length and network structure can influence and determine physical properties of the cell. For example, the effective elasticity of the actin cortex, which forms below the cell membrane and determines its physical properties like surface tension and bending rigidity, is controlled by the length of individual filaments and how they are cross-linked together [8, 9]. Filaments can also induce cell motility [10] or change the char-

acter of filamentous solutions *in vitro* [8, 11, 12]. This again emphasizes their dynamic nature and the importance of understanding the functionality of the cytoskeleton to understand the behavior of cells.

The three different classes of filaments can be distinguished through the chemical structure of the monomers, which build the filament. Nonetheless, all types share common properties. First of all, they are elongated aggregates of polymer subunits that by themselves assemble and disassemble at the ends of the filaments by addition or removal of single subunits, annealing of smaller filaments, and in the bulk of the filaments by severing. The chemical generation or destruction of bonds between individual subunits can be modified by other proteins bound to the monomers, influencing the subunits' internal structure [5]. The monomers building up the filament may be chemically apolar or polar. If they are polar, their polarity is transferred to the whole filament by the way the polymer chains are assembled. Whereas intermediate filaments are apolar, actin filaments and microtubules aggregate in a polar manner. On top of that, the polarity of the monomers allows for directed motion of proteins along the filaments, making them an ideal track for cellular transport [5].

We first focus on intermediate filaments. This filament class is again divided into several subfamilies, for example vimentin or keratin. The main role of these filaments is to make cells resistant to external stresses [3, 5]. Therefore they are often found in cells of vertebrates lacking an external skeleton [13–15]. In most cells, intermediate filaments form a network concentrated close to the nucleus and extending towards the cell edges [16]. Vimentin is also known to play a role during wound healing when blood platelets are activated [17].
The diameter of intermediate filaments is usually approximately 10-12 nm, which lies between that of actin filaments (7-10 nm) and microtubules (25 nm). That is also the origin of their name [18].
Although the details of the three-dimensional structure of intermediate filaments are still discussed [19, 20], they are assumed to be elongated assemblies of subunits of a specific type, for example vimentin filaments consist of vimentin dimers, where every dimer has a length of approximately 60 nm [21]. The dimer itself consists of an N-terminal domain, which is referred to as head and a C-terminal domain, also called tail. Head and tail are linked together via an α-helical coiled-coil rod, see Fig 1.1.
Intermediate filaments are flexible with a persistence length of approximately

Figure 1.1: **Structure of a vimentin dimer**. The chemically highly disordered tail and head are linked via two α-helical coiled-coil rods. The structure of the head domain was modeled *ab initio*. From [19], modified. Copyright 2015 by Elsevier.

1 μm. The persistence length is a measure for the rigidity of a polymer chain and describes, how fast correlations between the directions of monomers change along the chain. Nonetheless, in dense solutions of more than 10 $^{\mathrm{mg}}/_{\mathrm{ml}}$ together with appropriate cross-linking proteins generating a network, keratins can form hoofs and nails with a bending modulus in the range of giga Pascal. On top of their flexibility, intermediate filaments can be stretched up to 3.5 fold and can sustain forces of 1-2 nN before they break, which is two to three times larger than the forces observed for microtubules [20, 22].

Actin filaments, also known as microfilaments or F-actin, are built of globular actin monomers (G-actin), assembling in a helical double-stranded structure with a diameter of 5-9 nm and a distance of repeated twists at 37 nm [5, 23], see Fig. 1.2(a).
The persistence length of actin is approximately 15 μm [24]. Thus single actin filaments are semiflexible in the sence that they are stiffer than intermediate filaments but less stiff than microtubules.
Actin is for example known to play a role in the motility of single cells [25, 26] and the formation of protrusions of the cell membrane like stereocilia [27] in the inner ear that are relevant for hearing, or microvilli [28] that increase the surface area of the intestine. Besides that, actin forms a dense network close to the cell membrane, the cell cortex, influencing the mechanical properties of the membrane [29].

Microtubules are tube-like assemblies of typically 13 protofilaments, linear chains of tubulin dimers. Each dimer consists of α- and β-tubulin [5], see Fig. 1.2(b).
Microtubules are much stiffer than actin filaments and intermediate filaments with a persistence length in the order of several millimeters [30]. Due to their increased stiffness, microtubules are often used as tracks for intracellular transport together with molecular motors [31, 32]. On top of that,

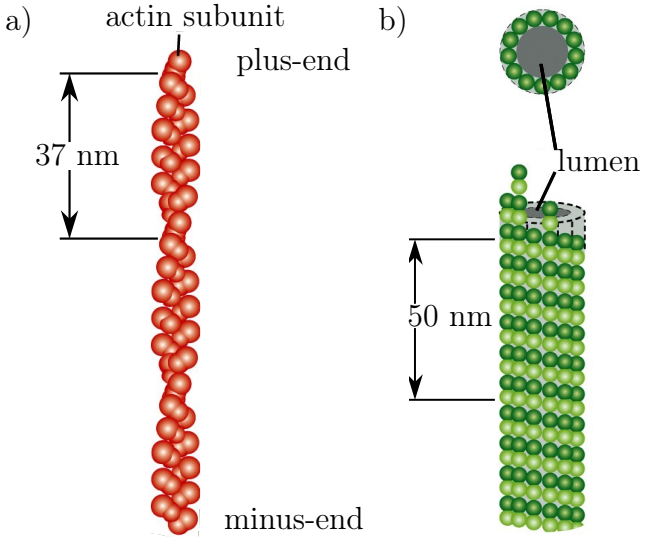

Figure 1.2: (a) **Structure of an actin filament**. The filament assembles from actin monomers (red globes) to a helical structure of two parallel strands. (b) **Structure of a microtubule**. 13 Protofilaments align with a slight offset to a tube surrounding the lumen. The periodicity of the structure is approximately 50 nm. α-tubulin is labeled in light green, β-tubulin in dark green. ©2007 from [5]. Reproduced by permission of Garland Science/Taylor & Francis Group LLC.

microtubules play a crucial role during cell division as they form the bipolar mitotic spindle that is located around the cell division site and is necessary to divide genetic material onto the daughter cells during cell division of eukaryotic cells. [5].

Actin and tubulin can bind nucleotides, adenosine triphosphate (ATP) and adenosine diphosphate (ADP) in the case of actin, guanosine triphosphate (GTP) and guanosine diphosphate (GDP) in the case of microtubules. The triphosphates can hydrolyze into diphosphates upon release of chemical energy,

$$\mathrm{ATP} \longrightarrow \mathrm{ADP}{-}\mathrm{P_i}{\uparrow}\,\Delta\mathrm{E}_0 \longrightarrow \mathrm{ADP} + \mathrm{P_i}{\uparrow}\,\Delta\mathrm{E}_1 \tag{1.1}$$

and

$$\mathrm{GTP} \longrightarrow \mathrm{GDP}{-}\mathrm{P_i}{\uparrow}\,\Delta\mathrm{E}_0 \longrightarrow \mathrm{GDP} + \mathrm{P_i}{\uparrow}\,\Delta\mathrm{E}_1\ , \tag{1.2}$$

consequently filaments are considered active. The bound nucleotide may also influence the chemical structure of the subunits and hence the bond between different monomers [5].

1.2 Biological filaments are dynamic structures

All filament types are permanently growing and shrinking by the processes mentioned above, namely assembly and disassembly of subunits at the ends, annealing of smaller filaments, or by severing of the filaments at any position. These length dynamics together with the filaments' activity can already suffice to show interesting phenomena like well regulated filament lengths [33]. As mentioned above, all filaments are aggregates of identical subunits. G-actin and tubulin monomers have a structural polarity that allows to distinguish between two chemically different ends named plus and minus. For actin, this polarity is caused by chemical domains within the actin monomer, whereas for tubulin, it results from the structure of tubulin dimers being composed of the two chemically different monomers α- and β-tubulin. Using this polar order, filaments assemble in a head-to-tail manner, where plus-ends of subunits always bind to minus-ends of a neighboring monomer and vice versa, rendering an overall polarity to the filament, with a well defined plus and minus-end. In the case of actin, those ends are also named barbed and pointed end, respectively, based on observation on actin filaments decorated with myosin motors using electron microscopy, where actin filaments present an "arrowhead configuration" [34].

Single filament subunits can polymerize and depolymerize both at the plus-end and at the minus-end. If the polymerization and depolymerization rates are denoted as $\nu_{\mathrm{p}}^{\pm}$ and $\nu_{\mathrm{d}}^{\pm}$ respectively, then those rates need to fulfill detailed balance,

$$\frac{\nu_{\mathrm{d}}^{+}}{\nu_{\mathrm{p}}^{+}} = \frac{\nu_{\mathrm{d}}^{-}}{\nu_{\mathrm{p}}^{-}} = \exp\left(-\frac{\Delta G}{k_{\mathrm{B}}T}\right) , \tag{1.3}$$

where $k_{\mathrm{B}} \simeq 1.38 \cdot 10^{-23}\mathrm{J}/\mathrm{K}$ is the Boltzmann constant, T is the temperature and ΔG is the free energy difference between the bound and unbound state of a filament subunit. Their polar nature also influences the rates of Eq. (1.3) such that $\nu_{\mathrm{d}}^{+} > \nu_{\mathrm{d}}^{-}$. The monomers and dimers incorporated into the filament have a triphosphate bound and can release a phosphate while in the filament. Apart from that, due to the fact that triphosphate-bound (T-state) subunits preferably polymerize at the plus-end, the chance of finding ADP- or GDP-bound (D-state) subunits at the minus-end is larger than at the plus-end. Hence, the depolymerization rate at the minus-end is mainly dependent on the weakly bound D-units. The dissociation constant, corresponding to the critical concentration above which a net growth can be expected, lies between 0.1 and 0.5 μM for T-units and is approximately 2 μM for D-units of actin [35]. Given the right concentration of nucleotides and monomers, the filament's

polarity can lead to treadmilling, where the filament in general grows at the plus-end and shrinks at the minus-end, causing the filament to travel through the cytosol although the individual subunits do not change their position. A theoretical analysis that explicitly accounts for the spatial gradient of T- and D-subunits along the filament can show that during treadmilling, dependent on the effective rates of phosphate release, length regulation of the filament can occur [33]. A subsequent study that incorporates details of the phosphate release identifies regimes of regulated length together with treadmilling, infinitely growing filaments and exponential length distributions with filaments that typically completely disintegrate in the course of time [36]. A central outcome of this study is that one should not expect length regulated treadmilling actin filaments for typical parameter values *in vitro* with intrinsic filament dynamics only. This gives rise to the investigation of the influence of associated proteins, discussed in section 1.3.

A remarkable feature of microtubules is that the depolymerization rate of GDP-bound subunits is large, whereas that of GTP-bound monomers is negligible [37]. As mentioned above, filaments usually incorporate subunits in T-state at the plus-end. After being polymerized, a dimer may hydrolyze GTP to GDP after some time. As this processes is stochastic and therefore happens at different times for individual subunits, some monomers at the filament's minus-end might still be in T-state, forming a stable cap to a large region of D-state subunits. If the tightly bound cap of GTP-bound subunits now disappears by hydrolysis into D-state and depolymerization, the large region of D-state subunits depolymerizes quickly in a catastrophe until again a cap of T-state monomers is at the minus-end as a rescue.

All filament types are dynamic polymer assemblies, constantly growing and shrinking, in steady interaction with their surrounding medium, which is usually the cytosol. These interactions come together with proteins attaching and detaching along the filaments, cross-linking them, influencing the rates of filament growth and shrinkage and enabling the transport of organelles and other cargo through the cell interior. In the next section, we present some general properties of the proteins relevant for the latter work.

1.3 Molecular motors can interact with single filaments

In section 1.1, filaments are introduced as the main components of the cytoskeleton. However, those filaments need associated proteins to finally self-organize into complicated structures [5] like the actin cortex or the mitotic spindle [38, 39]. In addition to molecular motors, using chemical energy to travel directionally along filaments, also non-motile proteins or passive particles, changing their position along the filament, disregarding the filament's polarity and without consuming chemical energy, play a a role during structure formation.

Proteins are usually in a solution surrounding the filament, from where they can bind to it. This binding may appear anywhere along the lattice or at specific binding sites, as it is known for capping proteins binding specifically to the barbed end of actin filaments [40]. Some protein types might promote the nucleation of new filaments. As an example, the Arp2/3-complex binds to existing actin filaments and serves as a nucleator to new ones. This way, Arp2/3 is an important ingredient in the generation of actin meshes like the actin cortex [41] below the cell membrane, where they enhance the cortex' stiffness [42], or the branched actin network in dendritic spines [43, 44], protrusion of neurons that are necessary in the formation of synapses in the neuronal system.

After being bound, some proteins can use chemical energy to directionally hop along the filament [45]. In the case of microtubules, two characteristic families of molecular motors often studied to investigate motile properties are kinesins and dyneins, see Fig. 1.3, as well as myosins in the case of actin filaments. Although the details of their individual design may differ, all members of these protein families share common properties. They have a motor domain consisting of one to four globular heavy protein chains called heads, which can bind to a filament and determine the motile behavior, as well as light and intermediate chains, which may serve different purposes like cargo binding and are in some cases referred to as tail domain. Dyneins differ from kinesins and myosins through the fact that they often need other proteins to be activated [46].

Myosins play an essential role in the contraction of striated muscle cells, where they form myosin filaments that reduce the end-to-end distance of muscle sarcomeres [46]. Apart from that, they may transport cargo, such as myosin-10 transporting VASP in filopodia [47], structures necessary for amoe-

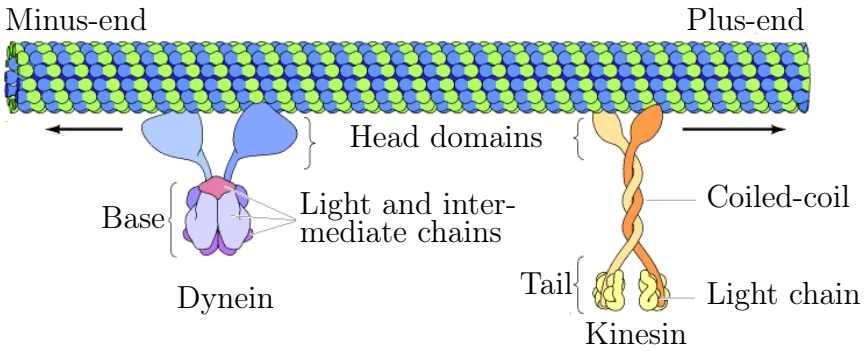

Figure 1.3: **Structure of kinesin and dynein proteins**. The typical hopping direction of the proteins is indicated by black arrows. From [46], changed. Copyright 2000 by Sinauer Associates.

boid movement. Kinesins and dyneins are also involved in the translocation of material. Furthermore, the proteins can generate a link between different nearby filaments, thus enhancing the generation of structures such as the mitotic spindle, where motors are involved in the regulation of microtubule overlaps [39, 48, 49], or the 9+2 axoneme in flagella. Here, microtubules are aligned in a circle of nine parallel filament pairs surrounding two central filament pairs. Dyneins activated by kinases and phosphates slide the filaments against each other, leading to stress in the network that causes flagella beads [50], which is again necessary for the movement of cellular swimmers [51].

In addition to the intrinsic dynamics of microtubules, molecular motors can interact with the filament and influence polymerization and depolymerization. This effect has been shown to play a role in the mitotic spindle, as tubules are constantly polymerizing and depolymerizing while maintaining their length. A knock-out of specific molecular motors can lead to a loss of length regulation and hence cause defects in the spindle [7, 39, 52–56]. These findings motivated studies *in vitro* to identify the molecular details of these mechanisms [57–61]. They prove that notably minus-end directed kinesin motors are able to destabilize the minus-end of microtubules and thus enhance depolymerization of subunits. Theoretical investigations of this class of systems reveal that with molecular motors, length dependent depolymerization rates can be established allowing for length regulation of actin filaments or microtubules [36, 62–64]. Apart from molecular motors, also capping proteins have been shown to influence the polymerization and depolymerization kinetics of filaments. As an example, CapZ is able to shorten the length of actin filaments [65].

Other than that, proteins might use the filaments as tracks to travel along in order to transport cargo or generate mechanical stresses [66]. As discussed above, molecular motors are often used to generate forces. Hence, we now shed light on the working principles of these machines in order to better understand which purposes they can fulfill inside cells. This requires investigation of their behavior under an external load.

A molecular motor is a machine, which transfers chemical energy, often provided by ATP, into mechanical energy. This power stroke is a sequence of chemical reactions, during which the triphosphate is hydrolyzed and conformational changes in the chemical structure of the motor lead to an effective displacement [67, 68]. The details of the power stroke may differ between different kinds of motors. Furthermore, some motors only perform a single power stroke and detach again from the filament, whereas others are processive. They perform several power strokes after binding to a filament, such that they travel along it and detach afterwards [69]. Nonetheless, an intrinsic feature of all motors is the discreteness of step sizes resulting from the nature of the power stroke. Hence, when dealing with motors, one of the first steps is to determine the step size of a single motor using optical tweezers together with fluorescence microscopy [70] or atomic force microscopy [67]. To perform these measurements, a silicon bead is chemically attached to the neck- or tail-domain of a single motor, see Fig. 1.4(a). This bead can be pulled via a focused laser beam exerting an harmonic force on the bead by inducing an electric dipole moment. If the properties of the optical tweezer and the link between the motor and the bead are known, both the position of the motor and the force acting on it can be derived through the displacement of the bead. For kinesins, a typical step size of 8 nm has been observed [70], see Fig. 1.4(b) and each step corresponds to a single ATP hydrolysis [71, 72].

As mentioned above, either in filament networks or during cargo transport, motors act under the influence of an external force, so it is important to analyze their behavior if a force is applied. This can be achieved by using optical tweezers [72], see Fig. 1.4(a). The results of these measurements show that molecular motors and also other filament associated proteins may have a qualitative difference in their behavior in presence of an external force and two major regimes can be identified: Slip bonds, where the lifetime of a bond is lowered by an external force, and catch bonds, whose lifetimes are increased up to a critical force and decrease for even larger forces. In the

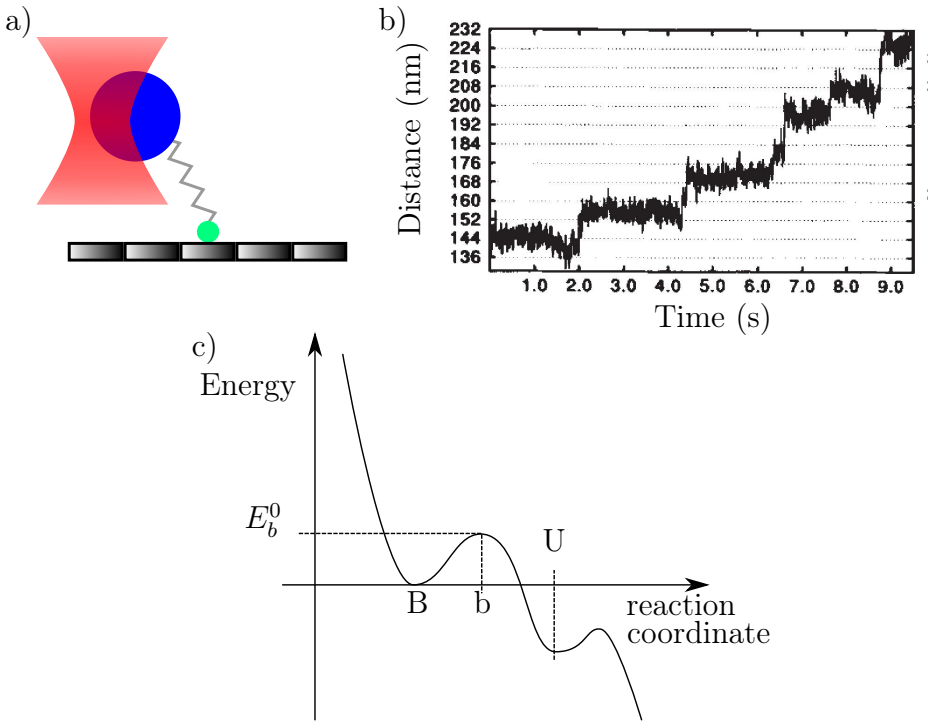

Figure 1.4: **Measurements on single motors**. (a) Preparation of a single motor for measurements with an optical tweezer. A silicon bead (blue) is attached to the neck or tail domain (gray) of a motor (green) traveling along a filament (gray rectangles). The bead is controlled via a focused laser beam (red). (b) Distance traveled by a single kinesin as a function of time. From [70]. Copyright 1993 by Nature Publishing Group. (c) Potential landscape for Kramer's rate theory. Stable bound (B) and unbound (U) states are separated by the instable state (b) with height E_b of the energy barrier.

same way, motor velocities can be affected by an external force. Note that motors are indeed able to change between those regimes depending on their environment [73, 74].

The behavior of slip bonds can be explained by considering Kramers' rate theory [75, 76]. The transition rate τ between the bound state and the unbound state of a protein is influenced by the energy barrier E_b^0 between those states

$$\tau \propto \exp(-E_b^0/k_\mathrm{B}T) \ , \tag{1.4}$$

see Fig. 1.4(c). If a force is applied, the energy barrier is diminished as the protein is stretched, leading to an increase in the detachment rate. In

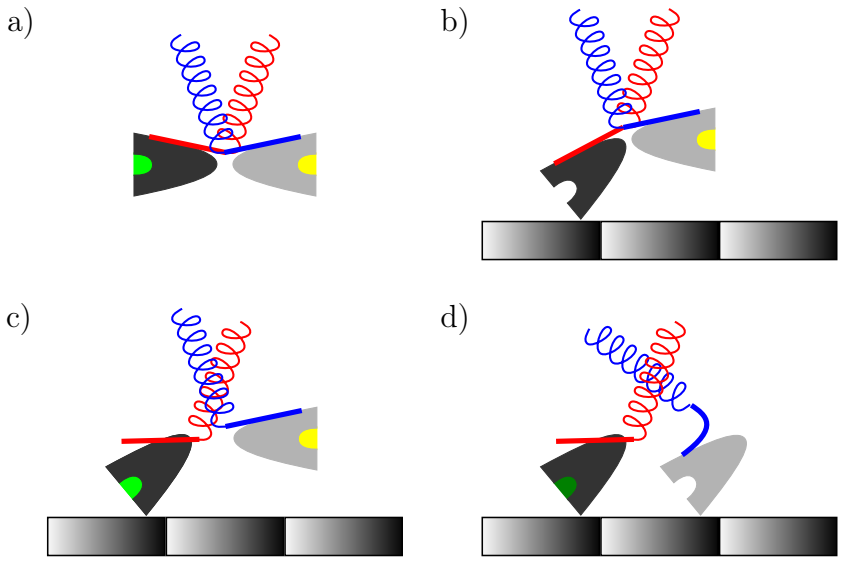

Figure 1.5: **Illustration of a hand-over-hand-model**. (a) A kinesin is represented via two heads (dark and light gray) that are connected via neck linkers and a spring-like tail domain (blue and red). Each head can individually bind ATP (light green), ADP (yellow) or ADP together with an inorganic phosphate (dark green) or neither of those nucleotides. (b) In the first step, one head is attached to the filament without a nucleotide, the free head has a diphosphate bound. (c) The attached head binds ATP leading to a conformational change. (d) The free head releases ADP and attaches to the filament while ATP in the attached head is transferred to ADP and P_i. After [67].

the case of catch bonds, the external force leads to a conformational change in the protein. This change can induce new binding sites and thus change the free energy antagonistically to the external force, leading to an effective decrease of the detachment rate until a critical force, after which those conformational changes are not able to compensate any additional force applied and the protein exerts a slip bond behavior again [77].

For a long time, it was unknown how processive motors walk along a microtubule. Two major models were proposed, one in which the motor walks in a hand-over-hand manner and the inchworm model, in which the motor walks like a caterpillar, one head always following the other one. Kinesins have been shown to move according to the hand-over-hand model [78], and a large variety of those models exists [79]. Here, an example of such a model is introduced, see Fig. 1.5, that can be solved analytically and is able to reproduce experimental findings as well [67].

In this model, a kinesin motor is described via two heads, which are connected by their neck linkers and tail domains. Each of the two heads is able to bind a nucleotide independent of the other head, where the nucleotides can be either an ATP- or an ADP-molecule or ADP in combination with an inorganic phosphate. Binding and unbinding of nucleotides happens with the surrounding medium that is assumed to contain neither ADP nor inorganic phosphate. In the beginning, a motor is in state K, meaning that one head is attached to the filament without a nucleotide bound. Meanwhile, the other free head is oriented towards the plus-end and has ADP bound. To get to the next state K·T, the attached head binds ATP leading to a conformational change of the motor and a displacement $\delta_1 = 1\,\mathrm{nm}$. In the next step, ATP in the attached head is hydrolyzed to ADP and inorganic phosphate. Meanwhile, the free head releases its ADP and attaches to the adjacent filament site. This process leads to a further displacement $\delta_2 = 1\,\mathrm{nm}$ of the motor, which is now in state K·P. Afterwards, the originally attached motor detaches from the filament and the motor goes back to the conformation K with a displacement $\delta_3 = 6\,\mathrm{nm}$, completing the cycle of motor states. This leads to a total displacement of

$$\Delta = \sum_{i=1}^{3} \delta_i = 8\,\mathrm{nm}\ . \tag{1.5}$$

The respective reactions are described by

$$\mathrm{K} \underset{k_{-1}}{\overset{k_1[\mathrm{ATP}]}{\rightleftharpoons}} \mathrm{K}\cdot\mathrm{T} \xrightarrow{k_2} \mathrm{K}\cdot\mathrm{P} \xrightarrow{k_3} \mathrm{K}\ , \tag{1.6}$$

with the rates k_1 for ATP binding, k_{-1} for ATP release, k_2 for the transition from states $\mathrm{K}\cdot\mathrm{T}$ to $\mathrm{K}\cdot\mathrm{P}$ and k_3 from state $\mathrm{K}\cdot\mathrm{P}$ to the original state K. Note that the third step is associated with the largest displacement of the motor. The total reaction rate follows from the principles of Michaelis-Menten kinetics [67]:

$$k_{\mathrm{total}} = k_{\mathrm{cat}} \frac{[\mathrm{ATP}]}{k_{\mathrm{M}} + [\mathrm{ATP}]}\ , \tag{1.7}$$

where

$$k_{\mathrm{cat}} = (k_2^{-1} + k_3^{-1})^{-1} \tag{1.8}$$

is the effective rate to go from the K·T-state to the original K-state and

$$k_{\mathrm{M}} = \frac{k_3(k_2 + k_{-1})}{k_1(k_2 + k_3)} \tag{1.9}$$

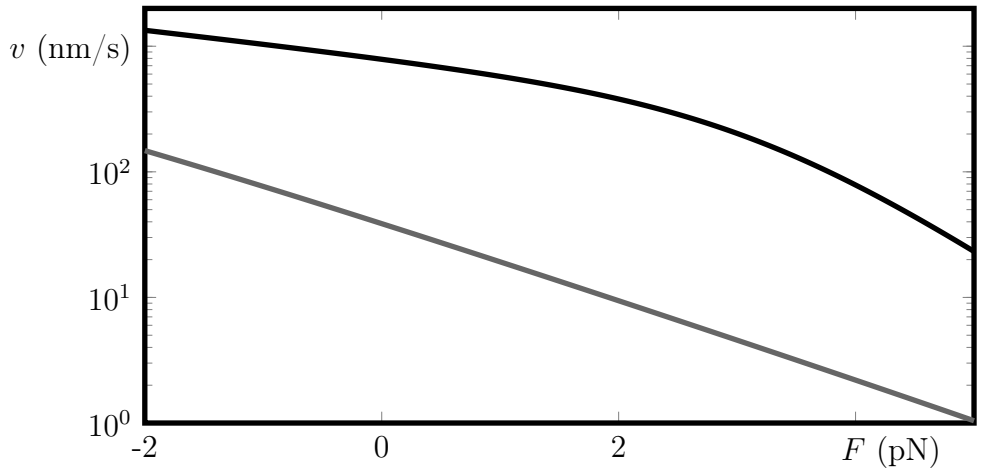

.

Figure 1.6: **Force-velocity plot** of the hand-over-hand model presented. The lines illustrate the velocity as a function of the applied external force, see Eq. (1.12). Different lines are for varying concentrations of ATP: [ATP] = 670 μM (black), 1.5 μM (gray). Other parameters are $k_{\mathrm{B}}T = 4.11\,\mathrm{pN}\cdot\mathrm{nm}$, $\bar{k}_1 = 100\,\mu\mathrm{M}^{-1}\mathrm{s}^{-1}$, $\bar{k}_{-1} = 3000\,\mathrm{s}^{-1}$, $\bar{k}_2 = 105\,\mathrm{s}^{-1}$, $\bar{k}_3 = 5000\,\mathrm{s}^{-1}$. Parameters taken from [67, 80]

is the corresponding Michaelis constant.
An external force f_{ext} would change the free energy barrier associated to the proteins and thus influence the rates according to [75, 76]

$$k_i = \bar{k}_i \exp\left(-\frac{F\delta_i}{k_{\mathrm{b}}T}\right) \tag{1.10}$$

for $i \in \{1, 2\}$ and

$$k_{-1} = \bar{k}_{-1} \exp\left(\frac{F\delta_1}{k_{\mathrm{b}}T}\right) \ . \tag{1.11}$$

In these equations, the rates with a bar represent bare rates in absence of an external force. This allows to calculate the effective motor velocity

$$v = \Delta k_{\mathrm{total}} \tag{1.12}$$

with k_{total} as given by Eqs. (1.7)–(1.11), see Fig. 1.6.

Numerous extensions and variations of this model exist [67, 79, 81]. In general, they share the common feature that they relate the chemical reactions

happening during a power stroke with the displacement of the molecule using standard reaction kinetics. One further description is based on a two-state model only considering the bound and unbound state of motors together with an energy landscape reflecting the discrete nature of the filament [82]. This allows to incorporate collective dynamics of motors.

After looking on the behavior of single molecular motors, the discussion will now focus on collective phenomena. This way, we can address the question which effects can arise from the interplay of several proteins of the same type. In the theoretical description of such systems, lattice gas models have proven to be a proper approach for the investigation of discrete processes. One of the most-studied models introduced in this context is the totally asymmetric simple exclusion process (TASEP), originally used to describe the "kinetics of biopolymerization on kinetic acids" [83].
Since its introduction 1968, the TASEP has been studied in detail and a full solution was found [84]. However, instead of solving the full problem, mean-field approximations are also able to solve the system [85]. In a meanfield *ansatz*, correlations between neighboring sites of a lattice are only considered up to a certain order. To illustrate this, consider a one-dimensional lattice of N sites with a lattice constant Δ, where particles enter the lattice at site $i = 1$ at a rate α and leave the lattice at rate β from site $i = N$. A particle can hop from site i to $i + 1$ at rate 1, if the target site is empty. Hence, the master equation for the occupation density n_i at site i reads

$$\partial_t n_1 = \alpha(1 - n_1) - n_{1,\bar{2}} \ , \tag{1.13}$$

$$\partial_t n_i = n_{i-1,\bar{i}} - n_{i,\overline{i+1}} \qquad \forall\ 1 < i < N \ , \tag{1.14}$$

$$\partial_t n_N = n_{N-1,\overline{N}} - \beta n_N \ , \tag{1.15}$$

where $n_{i,\overline{i+1}}$ is the probability of site i to be occupied while site $i + 1$ is empty. The meanfield assumption now is that $n_{i,\overline{i+1}}$ can be rewritten as the probability n_i of site i to be occupied multiplied with the probability $1-n_{i+1}$ of site $i + 1$ to be empty. With this, the particle current between sites i and $i + 1$ can be written as $J_i = n_i(1 - n_{i+1})$.
In the stationary state $\partial_t n_i = 0$, the current in the bulk is constant since there is no loss of particles, hence $J_i \equiv J_0$. This allows to distinguish several phases depending on J_0, see Fig. 1.7(a). If $\alpha < \beta < 1/2$, a low density phase emerges, where the density $\rho_{\mathrm{LD}} = \alpha$ is given by the entry rate of particles only, see Fig. 1.7(b). Otherwise, if $\beta < \alpha < 1/2$, a high density phase arises with $\rho_{\mathrm{HD}} = 1 - \beta$. In the case of $1/2 < \alpha < 1$ and $1/2 < \beta < 1$, a phase of maximum current appears, as the current is given as $n_i = 1/2$ and hence

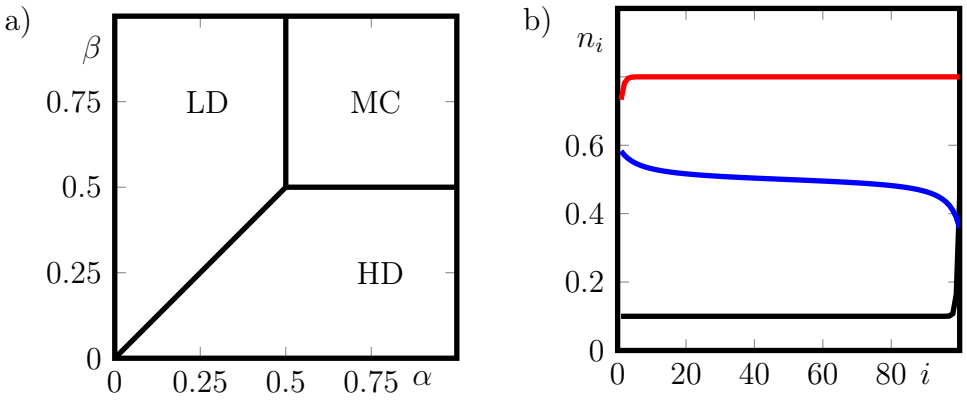

Figure 1.7: **TASEP** (a) Phase diagram of the TASEP with the high density phase (HD), low density phase (LD) and maximum current phase (MC). (b) Meanfield densities for $\alpha = 0.1$ (black) and 0.6 (red and blue) and $\beta = 0.2$ (black and red) and 0.7 (blue).

$J = 1/4$.

The TASEP has been applied to numerous systems with appropriate modifications. In particular, it has been used in traffic models [86–90]. Apart from that, the TASEP with extensions and modifications is of large relevance in studying the behavior of molecular motors hopping along filamentous tracks. Modifications include particle generation in the bulk, corresponding to adsorption of molecular motors on the filament [91–94]. These studies are able to show that crowding of motors may appear with discontinuities in the density of motors along the filament. The existence and position of this domain wall depends on the adsorption and desorption rate of proteins. Other studies investigate the influence of several lattices that interact [95] or consider the lattice itself to be dynamic, thus new lattice sites can be added or removed at the filament ends representing polymerization and depolymerization [36, 62–64, 96, 97]. Our previous studies [62] and the work by Melbinger et al. [63] consider molecular motors hopping directionally towards the filament end and enhance depolymerization of the end monomer. This way, due to accumulation of proteins in the bulk and transport towards the end, a depolymerization rate that depends on the filament length can be generated. Together with a constant polymerization rate, this can lead to length regulation of individual filaments, which is supported by experimental findings as well [60, 61].

To recapitulate, filaments are highly dynamic and due to the constant hydrolysis of ATP or GTP, they are furthermore driven out of thermodynamic equilibrium. This can already generate interesting effects such as treadmilling or dynamic instabilities.
In combination with additional proteins, filaments can self-organize into networks and generate tensile forces [67]. Moreover they organize into dynamic structures such as waves of polymerizing actin that can induce cell motility [98–102]. Apart from that, dynamic filament assemblies are also important in the neuronal system as branched actin meshes are necessary to shape dendritic spines in synapses [103]. This work focuses on the mitotic spindle, which is described in detail in the next section.

1.4 Life cycle of a cell and the mitotic spindle

After we have introduced the generic properties of the interplay between biological filaments and associated proteins, we will now shed light light on the interactions taking place in the mitotic spindle. Understanding this specific structure first requires a short introduction to the life cycle of higher cellular organisms.

The life cycle of healthy single cells as well as cells of multicellular organisms comprises phases of proliferation and division. The general purpose of this complex process is the replication of the cells by cell division. In order to guarantee correct replications, the cells need to ensure that cellular material is distributed in an "optimal" and well controlled manner onto the new cells. In this case, the term optimal does not imply that both daughter cells necessarily need to be identical after the division. Especially for tissues or stem cells, division can be asymmetric.
In the case of eukaryotic cells, the cell cycle can be divided into two major parts. At first, a new cell starts with its metabolism and grows during the interphase. This phase spans the time between two subsequent cell divisions and is in itself again subdivided into resting phases G_1 and G_2 that appear before and after the synthesis phase S [5, 46]. Afterwards, cells enter the mitotic phase, in which they distribute genetic and other material between the two daughter cells prior to their physical division.
The details of cell division differ for different classes of cells. Major differences exist between prokaryotes and eukaryotes, as the latter have a nucleus,

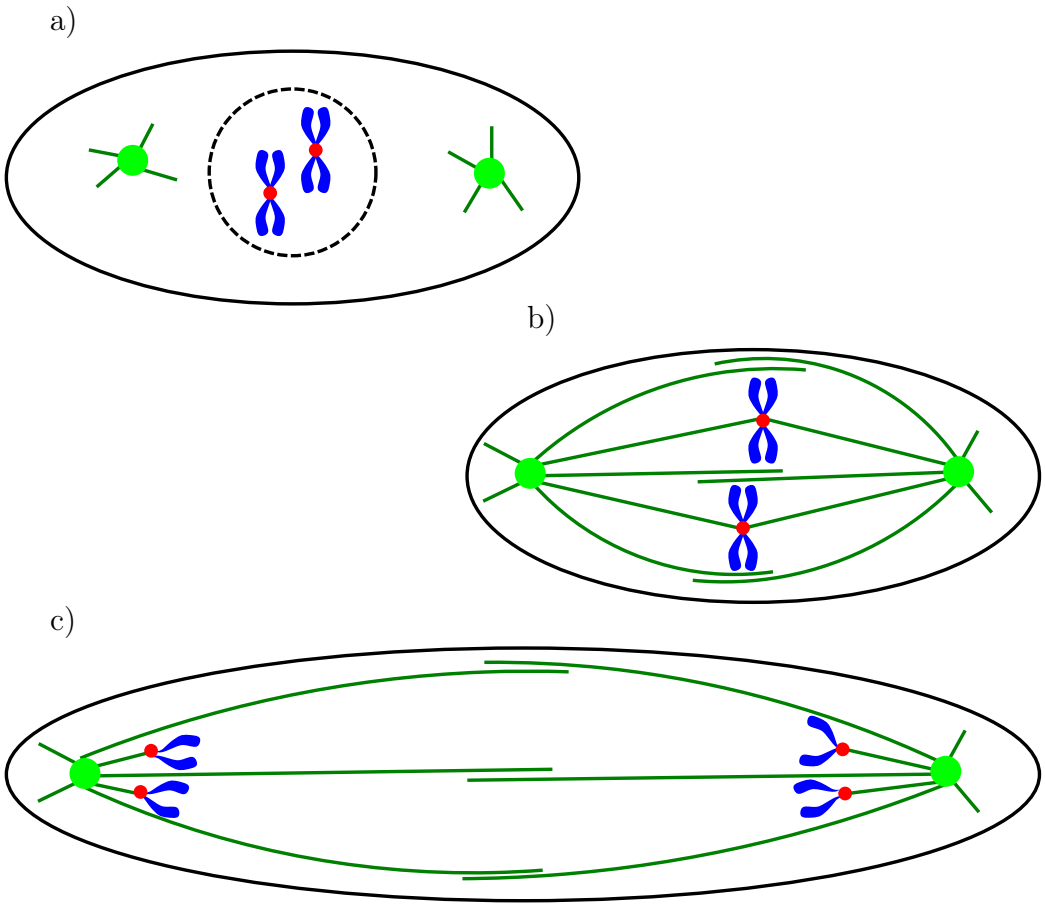

Figure 1.8: **Mitotic spindle during cell division**. (a) Prophase. The nucleus (black dashed line) is in the cell (black ellipse) center, chromosomes (blue) with kinetochores (red) are confined by the nucleus. The MTOCs (light green) with microtubules (dark green) are outside the nucleus. (b) Metaphase. Microtubules are connected to kinetochores and overlapping in the metaphase plate. The membrane of the nucleus is disintegrated. (c) Anaphase. Interpolar microtubules elongate, while filaments connected to kinetochores shorten and separate the chromatids.

whereas in prokaryotes, the genetic material is not confined by a membrane, but entangled. For the following work, we consider in detail only the cell division of eukaryotes.

Most cells enter cell division through the prophase [5], see Fig. 1.8(a), when chromatin fibers that contain the genetic material condense into chromosomes observable by standard light microscopy [104, 105]. Plant cells can additionally have a preceding preprophase, in which the nucleus is aligned close to the cell center.
During prophase, the nuclear envelope starts its disintegration to later enable segregation of genetic material in the form of chromosomes. Meanwhile, microtubules that later form the mitotic spindle start growing. The details of spindle formation and functionality are discussed later in this section. The prophase is followed by the prometaphase, when microtubules invade the area of the former nucleus and search for chromosomal kinetochores. Kinetochores are structures between the two sister chromatids that form a chromosome. They are important for generating tension within the spindle to localize chromosomes in the cell's equatorial plate. Attachment of kinetochores to filaments extends to the subsequent metaphase. Tension produced by the activity of molecular motors in kinetochores [106] together with polymerization and depolymerization of spindle microtubules now aligns chromosomes in the cell midzone, forming the metaphase plate, see Fig. 1.8(b).
The completion of the metaphase plate triggers the spindle assembly checkpoint [107], to ensure that genetic material is later equally distributed amongst the two daughter cells. This is connected to the onset of anaphase and the segregation of the genetic material towards the cell poles. Also during anaphase, some of the microtubules that build the mitotic spindle start to grow and thus lead to an elongation of the cell perpendicular to the metaphase plate, see Fig. 1.8(c). This process continues throughout telophase. In the meantime, the nuclei of the daughter cells are formed from the former nuclear envelope of the parent cell. After nuclei formation finishes, the chromosomes decondense, which completes mitosis and is followed by cytokinesis, the physical separation of the daughter cells by formation of a new cell wall in between the two daughter cells and contraction of cell membrane towards the cell center.
In animal and yeast cells, an actomyosin ring is contracting from the original cell membrane towards the cell center along the mid zone and either pulls the cell membrane or induces growth of new membrane material. In the actomyosin ring, actin filaments align along the equatorial plate and are pulled together by myosin-2 motor proteins [108].

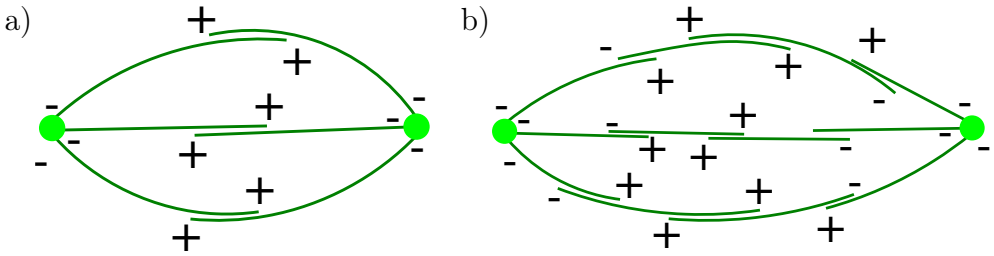

Figure 1.9: **General shapes of mitotic spindle**. (a) Microtubules (green lines) extending from the microtubule organizing center (green circles) towards the midzone. Filament polarity indicated by plus- and minus-signs. (b) Several microtubules with parallel overlaps, antiparallel overlaps only in the midzone.

In plant cells, phragmoplasts align in the middle of the equatorial plane and assemble a new cell wall in concentric rings starting from the cell center. The details of cytokinesis, especially of the contraction of the actomyosin ring are still not completely understood and a subject to current research [109–111].

During all mitotic processes of plant cells and eukaryotic cells, the mitotic spindle, also known as the spindle apparatus, plays a major role. It is a bipolar assembly of mostly microtubules, with the minus-ends of microtubules oriented towards the cell poles and filament plus-ends overlapping at the mid zone of the cell [5, 39, 112, 113]. In general, two different types of spindles can be found. The first type consists of long interpolar microtubules extending directly from the spindle poles to the equatorial plate of the cell, where they either attach to kinetochores or form stable overlaps with antiparallel tubules extending from the opposite cell pole, see Fig. 1.9(a). Yet, especially in larger spindles, the long microtubules are replaced by several short microtubules of same polarity, thus maintaining the overall bipolar nature of the spindle apparatus, see Fig. 1.9(b). For reasons of clarity, we will only refer to the case of long microtubules extending from centrosomes towards the cell mid zone, which corresponds to the case of numerous healthy eukaryotic cells.

In cells with centrosomes as microtubule organizing centers (MTOCs), minus-ends can be linked to the centrosomes and further tubules extend as astral microtubules around the center, see Fig. 1.10. Centrosomes are organelles containing two orthogonally oriented centrioles, tubular structures built of tubulin surrounded by a collection of proteins, the pericentriolar material. The centrosomes serve as nucleators for microtubules extending in asters

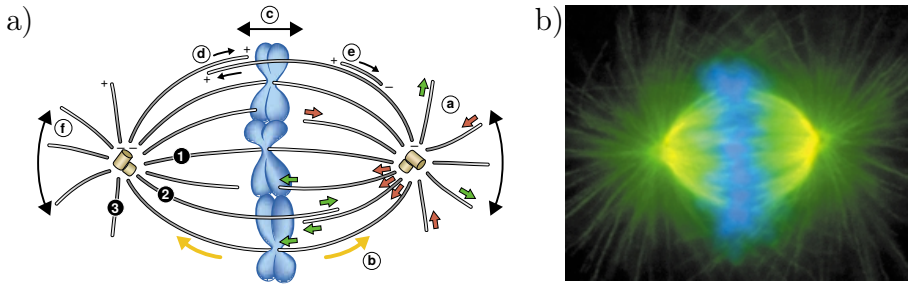

Figure 1.10: **Mitotic spindle**. (a) Sketch of spindle constituents and functionality. It is built of kinetochore microtubules (1), interpolar tubules (2), and astral microtubules (3). Green and red arrows represent polymerization and depolymerization activity, respectively ⓐ, yellow arrows indicate poleward microtubule flux ⓑ. Black arrows symbolize chromosome movements ⓒ, antiparallel microtubule sliding ⓓ, minus-end directed transport of microtubules ⓔ and fluctuations of the astral tubules ⓕ. (b) Fluorescence image of a mitotic spindle. Tubulin is labeled in green, chromosomes blue and TPX2, a targeting protein for the plus-end directed kinesin-like protein Xklp2 in red. Both figures from [39], modified. Copyright 2001, reprinted with permission from Nature Publishing Group.

from the centrosomes into the cytosol.
However, plant cells lack microtubule organizing centers and it has been shown that they are not necessary in eukaryotic cells either [114, 115].
Mitotic spindles are built by the polymerization of microtubules from the centrosomes with the growing plus-end pointing away from the MTOCs [116]. If microtubules get into contact with one another, cross-linking proteins start to organize the two formerly independent asters into the bipolar metaphase spindle structure [117, 118]. This structure is now able to guide the alignment of the chromosomes via molecular motors bound to the kinetochores that are attached to oppositely oriented filaments [5].

The mechanisms involved in the formation of the spindle apparatus are not completely clear yet. First of all, microtubules need to generate the bipolar structure, which is too slow if tubules only randomly search for kinetochores or other antiparallel filaments [119]. Instead, during the formation of the spindle, several proteins have been identified to play a role and foster spindle formation. For this work, we mention the passive cross-linker Ase1 as well as the molecular motors Ncd together with proteins that show a similar behavior, since they are used in the experiments presented in section 2.3. Besides those, numerous other proteins are known to influence spindle growth, size regulation and structure [113, 120].

Ase1 is a microtubule associated protein known to play a role in the formation of microtubule bundles and can be found for example in spindles of fission yeast [121]. It can suppress the disassembly of microtubules and promote growth and nucleation of new filaments [122]. Additionally, it decreases the rigidity of microtubules and hence assists in the alignment of bundles [122]. Due to the decreased rigidity, it is easier to bend microtubules, growing from the MTOCs, towards an antiparallel shape in the overlap regime of the spindle, see Figs. 1.9 and 1.10. Other experimental studies show that Ase1 diffuses along microtubules without any preferred direction at a very high rate and preferentially assembles in the overlap of microtubules [123]. Other cross-linkers with similar effects are MAP65 or PRC1 [122].

Ncd is a minus-end directed kinesin-14 protein [124] that probably binds to the β-tubulin of tubulin dimer [125]. It plays a role in anaphase spindle assembly and its correct functionality [126, 127], both in meiotic and mitotic cells. Similar to Ncd, also the kinesin-5 Eg5 and the kinesin-4 Xklp1 have been observed in the context of spindle size regulation [128, 129].

1.5 Biophysical aspects of spindle formation

Within the metaphase spindle, microtubules are constantly growing and shrinking [130, 131], leading to an effective poleward tubulin flux in the order of $1\,{}^{\mu\mathrm{m}}/_{\mathrm{min}}$ [132]. In contrast to that, the structure of the apparatus is maintained and well controlled during the mitotic phase, whose duration is in the order of minutes up to hours. So both the length of the dynamic microtubules as well as the overlap between pairs of microtubules must be regulated. Length regulation of dynamic microtubules has been studied *in vitro*, showing that molecular motors can influence growth and shrinkage of filaments [60, 61], which gives rise to length regulation of the filaments [62, 63]. In order to identify the mechanisms of overlap regulation, biological experiments have focused either on the influence of chromosomes and motors associated with them [133] or on the activity of molecular motors, such as Ncd or the kinesin-11 Eg5. They have observed that changing the motor activity indeed influences the spindle size and structure [55, 134–136]. Furthermore, these motors maintain their position relative to the spindle independent of the tubulin flux [137], again indicating that they have a regulatory function. However, it has been shown that also non-motor proteins are important to

enable a stable spindle structure *in vivo* [116, 138, 139]. In this case, proteins are not only generating cross-links between microtubules but are also influencing polymerization and depolymerization of dimers and thus regulating the filaments' lengths [116].

These biological characteristics — the microtubules' properties together with associated proteins — influence the size and structure of the spindle that depends on the overlap both of parallel and antiparallel filaments. The mechanism provided by these components must ensure the construction of a bipolar and highly dynamic structure of the right size.

Based on the experiments mentioned above, several physical models try to explain how components of the cytoskeleton can self-organize into the highly dynamic apparatus. Self-organization is a general aspect of many structures in cells. For example, cell motility can be explained by polymerizing actin waves that result from principles of chemical reactions [25, 26, 101, 102, 140]. Physical descriptions of actin networks help to explain how cells can generate forces to change the shape of the cell membrane. This way, it has been shown that filopodia can be produced with actin polymerization only [141]. Considering in addition an interaction between the cell membrane and the growing filaments allows to explain the stable length of filopodia [142–144]. All those description try to analyze biological systems with mathematical methods and couple the appearance of different structures to physical properties of their components. For example, the rigidity of filament networks depends on the length distribution of the underlying filaments [65] and the elasticity can show a number of surprising phenomena like nonlinear elasticity and negative normal stresses [145].

As far as the mitotic spindle is concerned, there is still a lack of bottom-up approaches that derive the apparatus' property from microscopic principles. Theoretical descriptions so far are able to reconstitute spindle-like bipolar assemblies based on assumptions on the interaction of microtubules. Minus-end directed motors are able to align antiparallel microtubules [49]. Stochastic simulations with bidirectional motors and microtubules growing as asters from MTOCs indicate that spatial regulation enhances the quality of spindles [146]. If molecular motors act together with passive cross-linkers, they are able to reconstitute a stable, bipolar spindle-like structure with spatially constricted microtubules [138].

The analysis in these models is based on complex simulations of all individual components. Therefore, investigating the sensitivity of the resulting structure

on input parameters is very time consuming and it is complicated to check for the robustness of a mechanism. It is necessary to identify not only important components, but additionally the properties of these components that are necessary for spindle formation. This way, a study was able to show that the length of a spindle constituted of microtubules and molecular motors depends on the speed of growth and shrinkage of the filaments involved [147]. Still it is not clear, which mechanisms are necessary in this case to enable spindle formation [120]. For example, the study by Loughlin et al. [147] incorporates several molecular motors with different other proteins and it remains unclear, why individual components need to be present.
Other theoretical models try to use a higher level of abstraction. Coarse-grained descriptions do not account for individual molecules, neither do they explicitly contain information on the detailed properties of the particles involved. Instead, they rely on phenomenological parameters describing characteristic effects. One of these approaches interprets the mitotic spindle as a droplet of an active material [148] based on the observation of a positive correlation between the size of centrosomes and the spindle length [149]. Although they are able to reproduce dependences on characteristic quantities, these approaches do not provide a deeper understanding of the underlying molecular mechanisms.

The mitotic spindle is a very complex and dynamic structure, and its functionality requires fine orchestration of all processes involved in its formation and maintenance. Instead of trying to reconstitute a spindle as a whole, the work presented in this thesis is in line with other approaches that are discussed in the next chapter. In this context, experiments and theoretical investigations try to identify key components and minimal systems, showing a specific behavior relevant for spindle formation.
Recent *in-vitro* experiments investigated how stable overlaps between interpolar and hence antiparallel microtubules could be generated and regulated. The experimental studies together with theoretical analysis of similar systems are recapitulated in the next chapter. Together with our results presented in section 3.3, they build the base upon which in chapter 4 a physical model is introduced and analyzed that identifies the requirements to maintain a stable overlap between antiparallel microtubules. Together with length regulation of microtubules, this analysis provides a minimal system to generate a stable spindle with a well defined length.

Chapter 2

Molecular motors and passive cross-linkers influence the overlap between mobile and aligned microtubules.

As shown in chapter 1, microtubule overlaps are important to understand the behavior of the mitotic spindle *in vivo*. This chapter reviews both experiments *in vitro* and theoretical studies, investigating the impact of cross-linking proteins on the overlap of filaments and analyze forces generated in this context.

2.1 Molecular motors can increase and decrease the overlap between microtubules

As introduced in section 1.3, molecular motors are a key ingredient in many cellular structures and often involved in the generation of stresses [9]. If they are present in networks, they can affect stiffness by several orders of magnitude [150]. Yet, a full understanding of effects in a network requires a detailed analysis of the less complex system of two aligned filaments coupled via molecular motors. A theoretical study by Kruse and Sekimoto [151] shows that motor cross-linkers slide apart antiparallel filaments, while they may generate full or vanishing overlaps between parallel filaments depending on particle densities, motor processivity and boundary conditions.
To describe the system, the authors introduce a filament as an oriented linear

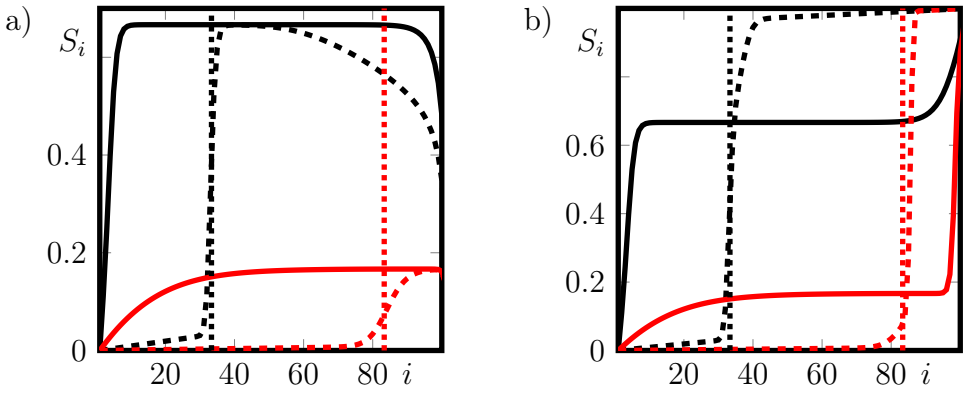

Figure 2.1: **Particle densities** S_i in steady state for $\sigma = 0$ (a) and 1 (b). Parameters are $K = 0.2$ (red), 2 (black), $\omega_a = 0.05\gamma$ (solid lines), 0.0005γ (dashed lines), $N = 100$. Vertical dotted lines indicate the solution of Eq. (2.3).

lattice with N sites. Molecular motors can attach at rate ω_a to any lattice site i, given that it is not yet occupied by another particle. The state S_i of a site is defined such that $S_i = 0$, if no motor is present at site i and $S_i = 1$ otherwise. If $S_i = 1$, the motor at site i can either detach at rate ω_d or hop towards site $i + 1$ at rate γ, given that the target site is empty. Hence, the meanfield equation reads

$$\partial_t S_i = \gamma S_{i-1}(1 - S_i) - \gamma S_i(1 - S_{i+1}) + \omega_\mathrm{a}(1 - S_i) - \omega_\mathrm{d} S_i \ . \tag{2.1}$$

This way, the authors combine the TASEP introduced in section 1.3 with Langmuir kinetics describing the attachment and detachment kinetics of proteins to a surface [67]. To complete the description, the boundary conditions are $S_0 = 0$ and $S_{N+1} = \sigma \in [0, 1]$.
Equation (2.1), describing the evolution of motor densities on a single filament, already shows an interesting behavior and a rich phase space if motors can hop off at the filament end, $\sigma = 0$ [92, 94]. If $\gamma = 0$, the solution to Eq. (2.1) is

$$S_i(t) = \frac{K}{1 + K} \left(1 - \exp(-(\omega_a + \omega_d)t)\right) \ , \tag{2.2}$$

given that site i is empty at $t = 0$. This solution corresponds to Langmuir kinetics. In Eq. (2.2), $K = \omega_\mathrm{a}/\omega_\mathrm{d}$ is the Langmuir constant. In the case $\gamma > 0$, the solution can either be attained numerically or via a continuum limit [92]. Here, only the numerical solution is presented.
As long as the hopping rate is small compared to attachment and detachment rates, the density S_i increases monotonically with increasing values of i until

it reaches its maximum value. Close to $i = N$, there is again a sharp decrease of the density towards 0, see solid lines is Fig. 2.1(a). The typical length scale, at which the particle density increases, increases with the processivity of motors $\gamma/\omega_{\mathrm{d}}$. If now motors are highly processive, this length scale may be in the order of the lattice size and a new behavior of the particle density is observed. The density increases up to a position x_{s}, where the density profile shows a discontinuous change called a "shock". At this domain wall between a region of low and high density, the density abruptly reaches the Langmuir steady state value $K(1+K)^{-1}$, see Eq. (2.2), and decays monotonically for $i > x_{\mathrm{s}}$ towards a vanishing value close to site N, see dashed lines in Fig. 2.1(a).
If a shock is present, its position can be extracted from the numerical solution of Eq. (2.1). However, the emergence and positioning of the domain wall can be analyzed by a continuous limit for the density profile [91, 93]. With this, the position of the shock x_s can be determined analytically to be at [93]

$$x_s = N\frac{1}{1+K} \ , \tag{2.3}$$

see vertical lines in Fig. 2.1. The position of the shock is independent of the boundary condition σ, compare Fig. 2.1(a) and (b).
Existence of a domain wall can be important for length regulation by molecular motors [62, 63]. If they enhance the depolymerization of subunits and make it faster than polymerization, the steady state length in this system is essentially determined by the domain wall, if one is present. The position of the domain wall and its fluctuations, together with the fluctuations in the polymerization and depolymerization of subunits can be described by analytic formulas. They allow to predict the average length of the filament together with the width of the fluctuations around the mean value.

Coming back to a pair of filaments, in order to describe cross-links between the two filaments **I** and **II**, the description is extended such that $s_i^{(k)}$ denotes the state of site i on filament k. A cross-link between two facing sites i on filament **I** and k on filament **II** is established with a probability p_{cl} and the resulting gliding velocity v is given by hopping of any of the two motor heads that generate the cross-link. The gliding velocity v therefore reads

$$v = \sum_{(i,k)\in\mathcal{L}} p_{\mathrm{cl}}\gamma \left\langle j_i^{\mathbf{I}} s_k^{\mathbf{II}} \pm s_i^{\mathbf{I}} j_k^{\mathbf{II}} \right\rangle \ , \tag{2.4}$$

where $\mathcal{L}$ is the overlap region, $j_i^k = s_i^k(1-s_{i+1}^k)$ is the current from site i to site $i+1$ on filament k, and $\langle\cdot\rangle$ denotes the ensemble average. The plus sign

in Eq. (2.4) applies for antiparallel microtubules whereas the minus sign is used in the case of parallel filaments.
Close to steady state, the densities s_i^k on the two filaments are assumed to be symmetric, therefore

$$s_i^{\mathbf{I}} = s_i^{\mathbf{II}} = S_i \tag{2.5}$$

and

$$j_i^{\mathbf{I}} = j_i^{\mathbf{II}} = J_i = \gamma S_i(1 - S_{i+1}) \ . \tag{2.6}$$

The approach in Eq. (2.4) neglects the dynamics of the cross-links themselves. Instead, it only assumes that a given ratio of the motors is always bound. This way, the authors are not able to describe force-induced deformation of cross-links if the filaments slide against each other. Still, this theory provides an intuitive means to analyze a system of filament pairs interacting via cross-linking molecular motors and allows to identify possible interesting characteristics.

Using the density profiles S_i, the current J_i can be calculated using Eq. (2.6). For a given distance ξ between the minus-ends of the two filaments and using Eqs. (2.5) and (2.6), the velocity defined in Eq. (2.4) can be rewritten as [151]

$$v^{(\mathrm{pa})} = \begin{cases} \mathrm{sgn}(\xi) p_{\mathrm{cl}} \left(\sum_{i=1}^{N-\xi-1} J_{i+\xi} S_i - \sum_{i=1}^{N-\xi} J_i S_{i+\xi} \right) \ , & \text{if } \xi \neq 0 \ , \\ 0 \ , & \text{if } \xi = 0 \end{cases} \tag{2.7}$$

in the case of parallel filaments and

$$v^{(\mathrm{ap})} = 2 p_{\mathrm{cl}} \begin{cases} \sum_{i=1}^{1+\xi} J_i S_{2+\xi-i} \ , & \text{if } 0 \leq \xi \leq N-2 \ , \\ \sum_{i=\xi-L+2}^{L-1} J_i S_{2+\xi-i} \ , & \text{if } N-1 \leq \xi \leq 2N-3 \end{cases} \tag{2.8}$$

in the case of antiparallel filaments. Different ranges of ξ result from the fact that parallel filaments of length N overlap if $|\xi| < N$ whereas antiparallel filaments overlap if $0 \leq \xi \leq 2N-3$.

Numerical solutions of the system show that in the case of antiparallel filaments, the overlap will always vanish independently of σ as the minus-ends

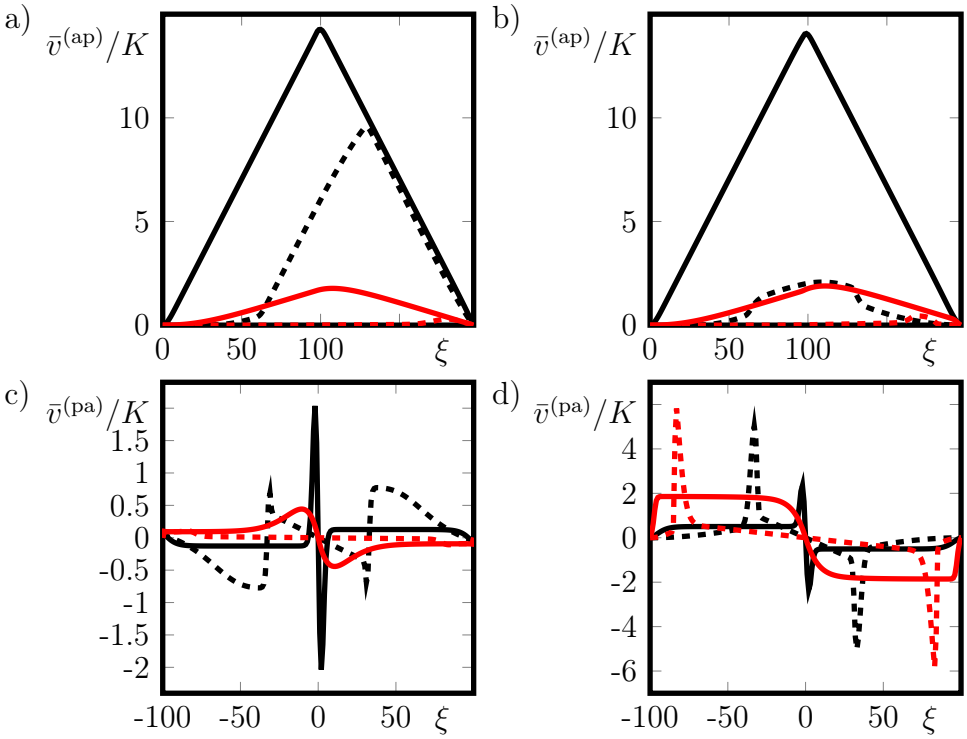

Figure 2.2: **Velocity profiles** for the rescaled velocities $\bar{v}^{(\mathrm{ap})} = v^{(\mathrm{ap})}/(\gamma p_{\mathrm{cl}})$ and $\bar{v}^{(\mathrm{pa})} = v^{(\mathrm{pa})}/(\gamma p_{\mathrm{cl}})$ in the case of antiparallel filaments (a,b) and parallel filaments (c,d) for $\sigma = 0$ (a,c), 1 (b,d), $K = 0.2$ (red), 2 (black), $\omega_a = 0.05\gamma$ (solid lines), 0.0005γ (dashed lines), $N = 100$.

are driven apart by the hopping of motors, see Fig. 2.2(a, b). For parallel filaments, the filaments are pulled towards full overlap if $\sigma = 1$, see Fig. 2.2(d) or if $\sigma = 0$ and the particle density is small, see red curves in Fig. 2.2(c). If the motor density is high, there are critical overlaps $\xi_1 < \xi_2$, with $\xi_1 = -\xi_2$. For initial overlaps between ξ_1 and ξ_2, the filaments are driven towards full overlap. Otherwise, the motors slide the filaments apart, see black curves in Fig. 2.2(c). Notably, the critical overlaps coincide with the maximum position in the particle density profile, see black lines in Fig. 2.1. In the case of profiles with a domain wall, this is also the position of the shock. This emphasizes the importance of investigating the particle behavior on a single filament to understand the forces generated by cross-linkers on a pair of filaments.

The system described above is crucially depending on the boundary conditions, as the value of the parameter σ suffices to switch between full or vanishing overlaps between filaments. As we show in section 4.3, changing

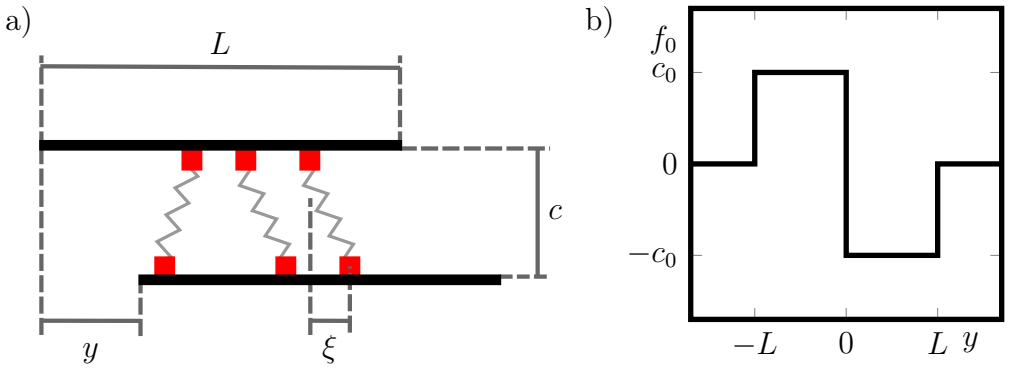

Figure 2.3: **Passive cross-linkers only**. (a) Sketch. Passive cross-linkers (red squares) connected via harmonic springs (light grey), filament as rectangles. For other labels, see text. (b) Force f_0, see Eq. (2.18).

boundary conditions in the case of diffusive cross-linkers can also affect the generation of full or vanishing overlaps. Again, we find full overlaps as soon as particles cannot leave the lattice via hopping, which compares to the case $\sigma = 1$. If particles can leave the lattice, both full and vanishing filament overlap can be stable, depending on particle densities.

2.2 Immobile passive cross-linkers generate forces increasing the overlap between filaments

The model discussed in the previous section considers molecular motors only. Another theoretical study investigates the influence of passive cross-linkers on the overlap between filaments and the forces generated [152]. Walcott and Sun consider two parallel filaments of length L at distance c, with the centers of the filaments displaced by a distance y in the direction of the filaments, see Fig. 2.3(a). Each cross-linker is composed of two heads connected via a linear spring. Any of the two filaments has N_{CL} cross-linker heads attached, which are distributed homogeneously along the filament. Either one of the heads is bound to one of the filaments or both are bound to different filaments. As the distribution of particles is symmetric between the two filaments, only quantities for one filament need to be considered in the preceding calculations. The proportion of cross-linking proteins at position x along the filament with extension ξ is given by $n(\xi, x)$, which evolves according to

$$\partial_t n + v(\partial_\xi - \partial_x)n = p_{\mathrm{a}}(\xi, x)(1 - N(x)) - k_{\mathrm{d}}(\xi)n \ , \tag{2.9}$$

where

$$N(x) = \int_{-\infty}^{\infty} n(\xi,\, x)\; d\xi \;, \tag{2.10}$$

$$k_{\mathrm{d}}(\xi) = k_{\mathrm{d}}^{0} \exp\left[a\left(\sqrt{\xi^2 + c^2} - c\right)\right] \tag{2.11}$$

and

$$\nu_{\mathrm{a}}(\xi,\, x) = \nu_{a}^{0} \exp\left[-bx^2 + a\left(\sqrt{c^2 + x^2} - c\right)\right] S(\xi,\, x) \;. \tag{2.12}$$

The function $S(\xi,\, x) = H(x+\xi) - H(x+\xi-L)$ with the Heaviside function

$$H(x) = \begin{cases} 0 \;\forall\; x < 0 \;, \\ 1 \;\forall\; x \geq 0 \;, \end{cases} \tag{2.13}$$

reflects the finite filament length, allowing only for a limited number of possible binding sites generated at rate ν_{a}. The functional form of $k_{\mathrm{d}}(x)$ describes slip bonds as described in section 1.3 and $N(x)$ is the total number of cross-links at position x. The parameters a, b, ν_{a}^{0}, and k_{d}^{0} are protein specific parameters, while v is a velocity generated by an external force. The authors analyze the force

$$F = N_{\mathrm{CL}} \int_{-\infty}^{\infty} \kappa\xi n \; d\xi \;, \tag{2.14}$$

where κ is the cross-linkers' spring stiffness.
Equation (2.9) can be solved using stochastic Langevin simulations. Additionally, the authors perform a Taylor expansion

$$n = \sum_{i=0}^{\infty} n_i v^i \tag{2.15}$$

of the steady state solution $\partial_t n = 0$ in terms of v and similarly of the force

$$F = \sum_{i=0}^{\infty} f_i v^i \tag{2.16}$$

exerted by the cross-linkers, where

$$f_i = \rho_{\mathrm{c}} \int_{-y}^{L-y} \int_{-x}^{L-x} \kappa\xi n_i(\xi, x) \; d\xi \; dx \;. \tag{2.17}$$

In Eq. (2.17), $\rho_c = N_{CL}/L$ is the effective density of cross-linkers along the filament.
With this *ansatz*, Walcott and Sun find explicit solutions for n_0 and f_0. In the case where the width of cross-linker binding $\sqrt{b}$ is much smaller than the filament length, $\sqrt{b} \ll L$, the force expression reduces to

$$f_0 = \mathrm{sign}(y) c_0 \left[H(y - L) - H(y + L) \right] \ , \tag{2.18}$$

where $c_0 = k_B T \rho_c \log(1 + K)$ and $K = \nu_a^0 \sqrt{\pi} (k_d^0 \sqrt{b})^{-1}$. Hence, the passive cross-linkers generate a force increasing the overlap between the filaments, as soon as they present any overlap in the beginning and as long as no external force drags them apart, see Fig. 2.3(b).
The origin of the shape of the force is essentially that first of all, the bulk of the overlap does not contribute to the actual force for vanishing sliding velocity, since binding of all cross-linkers is symmetric. The only remaining contribution to the force is generated at the boundaries of the overlap region, where the symmetry in cross-linker binding is broken due to the allowed configurations of cross-links. Hence, this work shows that the force exerted by passive cross-linkers on a filament in steady state, see Eq. (2.18), should have a magnitude which is independent of the overlap length and always tries to generate full overlaps. This means that passive cross-linkers are able to generate directed forces in filament networks.

2.3 Molecular motors and passive cross-linkers generate stable overlaps

As the theoretical study presented in section 2.2 shows, passive cross-linkers are able to generate full overlaps between filaments. Similarly, the work presented in 2.1 indicates that molecular motors may separate filaments.
In the experimental studies [153, 154] discussed in this section, *in-vitro* assays show that molecular motors together with passive cross-linkers are able to generate finite stable overlaps between antiparallel microtubules. The authors also provide theoretical descriptions in addition to their experimental work, which is discussed at the end of this section. An experiment conducted on an equivalent system with different types of molecular motors and passive cross-linkers [129] shows similar results.

The experiments try to reconstitute *in-vivo* observations of the mitotic spindle as well as simulations mentioned in 1.2, proving that both molecular mo-

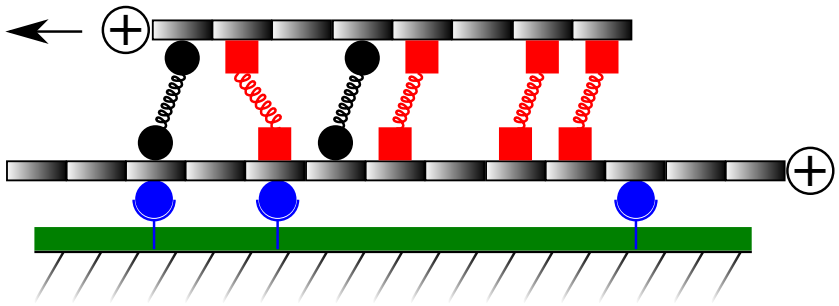

Figure 2.4: **Experimental setup** used in [153] and [154]. A surface (black line) is coated with several chemicals (green), to prevent unspecific binding, and Biotin antibodies (blue). Filaments (black rectangles) coated with Biotin (blue circles) can bind to the antibodies. Ase1 (red squares) and Ncd (black circles) proteins can bind to the filaments and generate a driving force (black arrow) transporting the transport tubule (upper filament) towards the minus-end of the template microtubule (bottom filament). Cross-links between the filaments are indicated via springs.

tors and passive cross-linkers are important to provide a functional spindle apparatus, especially by regulating the overlap of interpolar microtubules.

The setups used in the experiments by Braun et al. [153] and Lansky et al. [154] are similar, see Fig. 2.4. The authors prepare a coated surface with Biotin antibodies and additional chemicals to prevent unspecific binding of tubules to the surface. Afterwards, filaments that have Biotin attached are added to the buffer above the surface. Now Biotin can bind to its antibodies and thus attach the filaments, which are referred as "template microtubules", to the surface. After that, the passive cross-linker Ase1 together with the molecular motor Ncd are flushed into the experimental chamber at their final assay concentrations. In the third preparation step, non-biotinylated microtubules are flushed into the chamber. These "transport microtubules" can then bind to the template microtubules already present, using the cross-linkers bound to the template microtubules. As a last step, the chamber is rinsed with a solution of Ase1 and Ncd, thereby washing out non-bound transport microtubules. Now the generation of overlaps can be observed using fluorescently labeled proteins.

In Braun et al. [153], the transport filament of length L_0 first slides along the template tubule at velocity v_0, until it reaches the end of the template. As soon as the overlap between the filaments is reduced, the sliding velocity decreases, see Fig. 2.5(a). At the same time, the fluorescence intensity of

Ase1 increases in the overlap region. This indicates that Ase1 is able to slow down the sliding of the filaments by an effect that, as the authors state, results from crowding of Ase1 in the overlap. Apart from that, the authors find that the filament ends provide a diffusive barrier for the Ase1, such that they cannot leave the overlap region via diffusion along the filament. Finally, a stable finite overlap between the filaments is generated, see black line in Fig. 2.5(b).
To explain the slowing down of the gliding, the authors introduce a description that accounts for the time evolution of the overlap length L and the number n of Ase1 in the overlap. The effect of motors is introduced via an effective velocity $v(\rho)$ depending on the concentration $\rho = n/L$ of Ase1 in the overlap as $v(\rho) = a\rho + b$. The parameters a and b are fitted to experimental data with knowledge of the initial velocity of the tubule and its length L_0. The resulting equations are

$$\frac{\mathrm{d}n}{\mathrm{d}t} = -(1-\varepsilon)\ v(\rho)\frac{n}{L} + k_{\mathrm{on}}L - k_{\mathrm{off}}n\ , \tag{2.19}$$

$$\frac{\mathrm{d}L}{\mathrm{d}t} = -v(\rho)\ , \tag{2.20}$$

with the adsorption and desorption rates k_{on} and k_{off} of Ase1 and the compaction efficiency ε. The compaction efficiency describes, how well the proteins can be packed. If $\varepsilon = 0$, Ase1 cannot be compacted at all and every sliding leads to a loss of particles out of the overlap. In the opposite case $\varepsilon = 1$, the proteins can be compacted infinitely.

The system of equations Eqs. (2.19) and (2.20) is able to qualitatively reproduce the reduced gliding velocity, see red lines in Fig. 2.5(b). However, the origin of the reduced sliding velocity v for finite overlaps remains unknown. Additionally, this analysis neglects the movement of particles along the filaments, which we introduce in our analysis in chapter 4.
The second experimental study [154] by Lansky et al. explains the origin of the reduced sliding velocity via an entropic force based on the number of available configurations for Ase1 cross-linkers. The force measurements are performed in a similar experimental setup with aligned filaments and cross-linkers together with an optical tweezer enabling force measurements.

This experiment shows that the force exerted by Ase1 cross-linkers increases significantly when the overlap is reduced. The authors explain this effect via an entropic force.

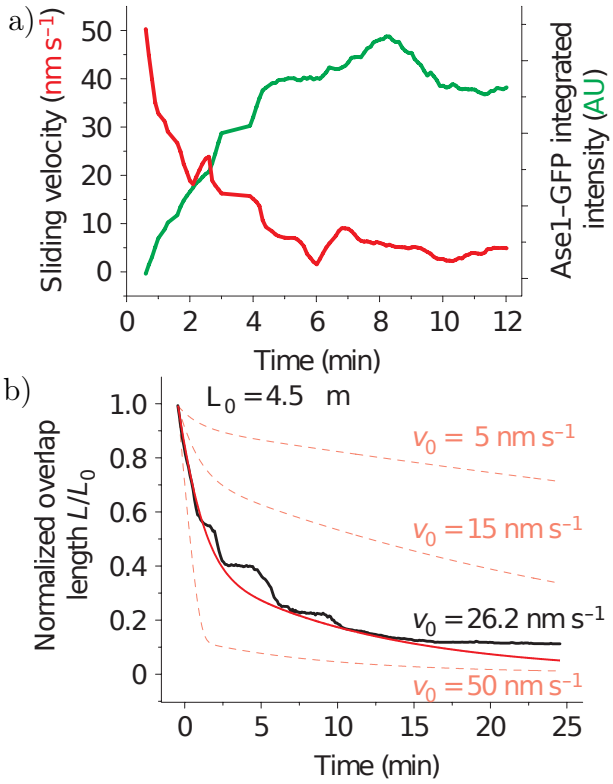

Figure 2.5: **Experimental results**. (a) Sliding velocity and fluorescence intensity of labeled Ase1. The sliding velocity of the transport tubule goes down, while the fluorescence intensity of Ase1 goes up in the overlap region. Experimental conditions: [Ase1-GFP] = 0.39 nm, [Ncd] = 0.29 nM in solution, $L_0 \approx 6 - 7\,\mu$m determined by eye. (b) Time evolution of an overlap from experiments (black lines) and from the theoretical description (red lines) for different initial velocities v_0, as indicated in the plot. Both figures from [153]. Copyright 2015, reprinted with permission from Nature Publishing Group.

The general concept of forces that originate from the attempt of a system to reach maximal entropy has been studied in many contexts during the last decades, starting from explaining the forces observed from the extension of macromolecules [155]. Brownian motion can also be explained as a purely entropic effect, retrieving Einstein's relation for the average displacement of a particle in time and on top of that predicting melting temperatures of crystals and surface tensions of salt melts by accounting for additional interactions between ions [156]. Similar approaches are used to explain forces measured on passive polymer chains [157] or further study the Brownian motion of particles [158]. Recent research tries to derive gravity [159], Coulomb forces [160–162] and intelligence [163] from entropic principles, although the

concept of entropic gravity is still discussed [164].

The theory provided by Lansky et al. only considers cross-linker dissociation within the overlap region of length L of the two filaments, which is in contact to a particle reservoir with dissociation constant $K_{\mathrm{D}}^{\mathrm{d}}$ [154]. Given the finite size δ of the tubulin dimers, the overlap offers $\ell = L/\delta$ possible binding sites for cross-linker heads. Each cross-linker is represented by two identical heads that are connected via a linear spring. Cross-linkers in solution can attach to the overlap region and initiate a cross-link, whereas bound cross-linkers can dissolve again. Assuming that there is steric interaction between individual cross-linkers and the springs connecting the heads of each cross-linker are infinitely stiff, the partition function $Q(n, \ell)$ for any number n of cross-linkers in this case can be written as

$$Q(\ell, n) = \binom{n}{\ell} \left(\frac{[\mathrm{X}]}{K_{\mathrm{D}}^{\mathrm{d}}}\right)^n \ . \tag{2.21}$$

with the concentration [X] of cross-linkers in solution.
The force F on an overlap L hence is

$$\begin{aligned} F &= \frac{k_{\mathrm{B}}T}{\delta} \log\left(\frac{Q(\ell+1, n)}{Q(\ell, n)}\right) \\ &= \frac{k_{\mathrm{B}}T}{\delta} \log\left(\frac{\ell+1-n}{\ell+1}\right) \\ &\overset{\ell \gg n}{\approx} \frac{k_{\mathrm{B}}T}{\delta} \frac{n}{\ell+1} \overset{\ell \gg 1}{\approx} k_{\mathrm{B}}T \frac{n}{L} \ . \end{aligned} \tag{2.22}$$

Equation (2.22) can be compared to that of an ideal gas, where $pV = nk_{\mathrm{B}}T$ and gives rise to forces in the pico Newton range, similar to the forces measured in the experiments.

In the case that cross-linkers attach and detach on timescales comparable to the experiments, such that the particle number n is not fixed anymore, the partition function Q is given as

$$Q(\ell) = \sum_{n=0} Q(\ell, n) = \left(1 + \frac{[\mathrm{X}]}{K_{\mathrm{D}}^{\mathrm{d}}}\right)^{\ell} \tag{2.23}$$

with the associated free energy

$$\mathcal{F} = -k_{\mathrm{B}}T \log(Q(\ell)) = -k_{\mathrm{B}}T\ell \log\left(1 + \frac{[\mathrm{X}]}{K_{\mathrm{D}}^{\mathrm{d}}}\right) \ . \tag{2.24}$$

The force

$$F = -\frac{\partial \mathcal{F}}{\partial \ell} = -\frac{k_\mathrm{B}T}{\delta} \log\left(1 + \frac{[\mathrm{X}]}{K_\mathrm{D}^\mathrm{d}}\right) \tag{2.25}$$

in the case of non-constant particle numbers is thus independent of the overlap length. This result is equivalent to the analysis by Walcott and Sun [152], who also mention explicitly that their work automatically incorporates any possible entropic effects. The results of the entropic analysis in Eqs. (2.22) and (2.25) can only be applied for experiments, where the assumption of a constant particle number is valid, or for very long experiments, where the entropic analysis retrieves the same result as in Eqs. (2.18) and (2.25). For very short experiments, on which the assumption of constant particle numbers may be valid, it is not obvious if entropic principles can be applied. The fast drag velocity extends the cross-linker springs and the implicit assumption made by the authors that individual cross-linkers do not generate a mechanical net force via their spring extensions, is invalid. For a long experimental timescale, the entropic consideration gives a result comparable to that of Walcott and Sun. Yet, the latter theory allows to extent the analysis towards finite drag velocities, whereas the entropic force does not take into account finite sliding velocities of the filaments, see Eq. (2.25). Therefore, considering the forces generated by Ase1 or similar passive cross-linkers, to be a purely entropic effect, does not provide a deeper insight into the system. On top of their analytical calculations, Lansky et al. include stochastic simulations in their work, accounting explicitly for hopping and binding of individual passive cross-linker heads. These stochastic simulations are able to approximate results obtained from experiments under the assumption, that motors exert a force proportional to the overlap, sliding the filaments apart.

The experimental studies mentioned in this section show that stable overlaps between antiparallel filaments can be generated by the interplay of passive cross-linkers and molecular motors connecting the filaments. However, both studies do not explicitly account for the dynamics of molecular motors in their theoretical analysis. The forces generated by molecular motors are always incorporated as effective external forces and only passive cross-linker dynamics are investigated.
The theoretical works presented in this chapter only consider one single particle species at the same time, either molecular motors [151] or passive cross-linkers [152–154] separately. It remains unclear, how the interaction of several particle types can affect the overlap between microtubules.
In the next chapter, we discuss how interactions between directionally moving

and diffusive particles affect particle distributions, leading to segregation of individual species.

Chapter 3

Segregation of different particle species via steric interactions

As can be seen from section 2.1, already the analysis of particles on a single filament reveals interesting phenomena. Domain walls between regimes of high and low particle densities can emerge, and those domain walls can influence the force generated between the filaments, see section 2.1, or allow length regulation of filaments with molecular motors [62, 64, 92, 94]. Before focusing on the interaction between two filaments we therefore first investigate the consequences of different types of proteins interacting on a single filament.
We start with single-file diffusion as an example for a system of purely passive particles, which sterically interact. Afterwards, we shed light on other studies on driven and passive particles in two-dimensional suspensions. Those studies show that domain walls can emerge between high density regimes of either passive or active particles. This provides a framework to our study on active and passive particles in one dimension, which is presented in section 3.3. It is shown that molecular motors and passive particles can segregate along a one-dimensional filament, if steric interactions between species exist. Additionally, we investigate the influence of boundary conditions on segregation phenomena.

3.1 Steric interactions influence the diffusion of particles in one dimension

In order to study the diffusion of particles along one dimensional structures such as biological filaments, single file diffusion — originally introduced to describe diffusion of potassium through channels in the cell membrane [165]

— has become a paradigm to describe a general class of systems where diffusion of interacting particles in one dimension is relevant. Analyzing the diffusion of particles in one dimension shows differences in the time dependence of the mean square displacement and correlations between particle positions depending on the form of the interaction potential [166–168]. Another study focused on the correlation between particle positions for different average particle densities, proving that different algorithms to describe particle movements are valid for high and low densities [169]. Experiments are able to reproduce theoretical predictions [170].

Single file diffusion describes the unbiased motion of particles under the assumption that they interact in a one-dimensional system. The motion of the particles can either be described via hopping on discrete lattices [171, 172] or by a continuous movement of particles in a narrow channel [173]. Single file diffusion can be regarded in the latter context as a generalization of a Tonks gas [174], solely describing the dynamics of gas particles under steric exclusion between individual particles. In the context of single file diffusion, usually particle movement in the course of time is tracked and the mean square displacement

$$\sigma(t) = \frac{1}{N} \sum_{i=1}^{N} ||\mathbf{x}_i(t) - \mathbf{x}_i(0)||^2 \tag{3.1}$$

is analyzed. In Eq. (3.1), $\mathbf{x}_i(t)$ is the position of particle i at time t and the sum averages over the number N of particles present in the system.
The interaction between particles is introduced as a potential $U_i(\mathbf{x})$, such that the force $\mathbf{F}_i$ exerted on particle i is given by

$$\mathbf{F}_i = \sum_{j=0}^{N} \nabla U_j(\mathbf{x}_i) \ . \tag{3.2}$$

For infinite lattices, the mean square displacement is a monotonically increasing function. Typical time scales of the growth depend on the form of the interaction potential. The special case

$$\sigma(t) \sim t \tag{3.3}$$

corresponds to purely diffusive behavior of a particle in one dimension without any interactions. Accordingly, the case

$$\sigma \sim t^{1+\varepsilon} \tag{3.4}$$

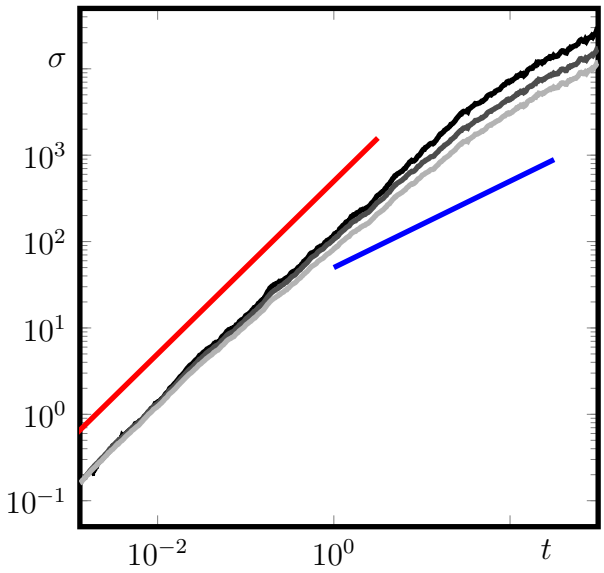

Figure 3.1: **Mean square displacement** σ for $N = 10$ (black), 50 (dark gray) and 200 (light gray) diffusive particles on a periodic lattice with $L = 1000$ sites. Mean square displacements where averaged using 40 independent simulations, where the particles where initially distributed randomly assuming a uniform probability distribution. Colored lines indicate $\sigma \sim t$ (red) and $\sigma \sim t^{1/2}$ (blue).

with $\varepsilon > 0$ is denoted as super-diffusive and sub-diffusive if $\varepsilon < 0$.

For this work, only the case of a hard-core steric interaction potential is of interest, analyzed on a periodic lattice of L sites populated by N particles. A particle can hop to any neighboring lattice site at rate D, provided that it is not yet occupied by another particle. Results from corresponding simulations using Gillespie's algorithm[1] show that the mean square displacement on short time scales is proportional to the time t. After a critical time t_c, it increases as $t^{1/2}$, see Fig. 3.1. From this we conclude that steric interactions are more important on longer time scales, whereas on short time scales particles simply diffuse as if no other particles were present. This is supported by the reduced critical time between the two different phases of motion for larger particle numbers: The denser the packing of particles, the earlier the influence of steric interactions between the particles on the mean square displacement is observable.

[1]Details of the algorithm are given in appendix A.

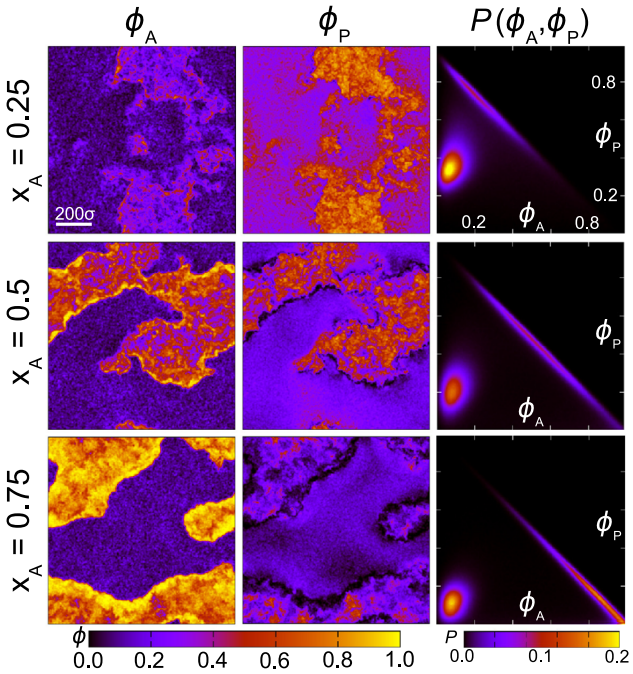

Figure 3.2: **Phase separation** of colloids for varying fractions of active particles x_A. The left column shows the distribution of active particles, the column in the middle the distribution of passive particles, and the right column the probability distribution $P(\Phi_A, \Phi_P)$. The total volume fraction of particles is $\Phi_0 = 0.6$ in all cases with a box size $L = 1000\sigma$. From [177], Copyright 2015 by the American Physical Society.

3.2 Spontaneous segregation of particles in solution

Single file diffusion is a one-dimensional description, only accounting for diffusive particles. Other than that, the interaction of actively driven particles and passive, diffusive particles has been studied in two dimensions. Systems that model the behavior of colloidal suspensions, are for example relevant to understand the behavior of active micro swimmers such as the algae Chlamydomonas Reinhardtii [175]. Usually, studies in this context investigate the influence of fluid properties such as viscosity [175]. Others use a mean-field approach, describing the colloidal suspension containing several individual particles as an active matter [176]. Recent studies proof that diffusive particles together with active, self-propelled ones can induce a phase separation of the different particle types [177, 178].

In [177], particles undergoing Brownian motion are in solution with active

self-propelled particles. The interaction between particles is introduced via a modified Lennard-Jones potential

$$U(r) = 4\varepsilon \left(\left(\frac{\sigma}{r}\right)^{12} - \left(\frac{\sigma}{r}\right)^{6} \right) + \varepsilon \tag{3.5}$$

with the distance r to the center of mass of a particle and positive parameters σ and ε. Furthermore, to simplify computations, the potential was cut off, such that $U(r) = 0$ for any $r > 2^{1/6}\sigma$. The equations of motion for particle i at position $\mathbf{r}_i$ and with orientation Θ_i are

$$\partial_t \mathbf{r}_i = \beta D_\mathrm{t} \left(\mathbf{F}_i + F_\mathrm{A} \mathbf{p}_i \right) + \sqrt{2D_\mathrm{t}} \mathbf{\Lambda}_\mathrm{t} \tag{3.6}$$

and

$$\partial_t \mathbf{\Theta}_i = \sqrt{2D_\mathrm{r}} \Lambda_\mathrm{r} \ . \tag{3.7}$$

In Eqs. (3.6) and (3.7), D_t and $D_\mathrm{r} = 3D_\mathrm{t}/\sigma^2$ are translational and rotational diffusion coefficients with respective unit-variance. $\mathbf{\Lambda}_\mathrm{t}$ and Λ_r are Gaussian white-noise forces accounting for thermal fluctuations. The conservative force $\mathbf{F}_i$ results from summing up all interaction potentials $U(r)$, given by Eq. (3.5), and F_A is the active propulsion force in the direction $\mathbf{p}_i = (\cos(\Theta_i), \sin(\Theta_i))$, which is set to zero in the case of purely passive particles and $F_\mathrm{A} = 24\varepsilon/\sigma$ for active particles. Hydrodynamic interactions are neglected in the dynamics. The authors investigate changes in the fraction of active particles x_A and the Péchlet number $\mathrm{Pe} = 3v_0\tau_\mathrm{r}/\sigma$ with the propulsion speed of active particle v_0 and the rotational relaxation time $\tau_\mathrm{r} = \sigma^2/(3D_\mathrm{t})$.

Numerical solution of the given equation of motion on a periodic quadratic box of length L reveals that depending on the fraction of active particles and the value of Pe, a separation of active and passive particles can be observed, see Fig. 3.2. The authors obtain a phase diagram showing that for larger values of the Péchlet number Pe, already smaller values of x_A allow observation of segregation. Another study with active particles only could show that suspensions of self-propelled particles are able to transmit forces between two walls in two dimensions [179]. Remarkably, there is a phase transition between attractive and repulsive forces depending on the density of active particles.

After all, the work mentioned above proves that active and passive particles together can show segregation, where domain walls appear, separating

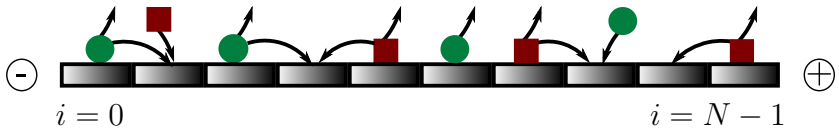

Figure 3.3: **Sketch of the theoretical description**. Motor particles (green) and passive particles (red) can attach to any empty lattice site (gray). Plus- and minus-end are indicated at sites $i = N-1$ and $i = 0$, respectively. Possible hopping processes are indicated as black arrows.

regions of high densities of either of the particle types. They emerge by self-organization of the incorporated particles. So far, these studies have only been performed in two dimensions, motivated by colloidal suspensions. In the next section, our own work is presented, proving that a segregation phenomenon can also be observed for active and passive particles in a one-dimensional system given that the particles incorporated are able to attach and detach anywhere along the lattice and interact sterically.

3.3 Segregation of diffusive and directionally moving particles on a polar filament

As presented in the first chapters, different types of cross-linkers play a role in the formation of many cellular structures, especially in the mitotic spindle. Nonetheless, the interactions between different species that hop along filamentous tracks are still poorly understood. Here, we investigate the impact of steric interactions between particles of different species hopping along filaments. Theoretical analysis is provided using a meanfield approach that allows for the identification of the effects necessary for particle segregation. The work presented in this section has been published in [1].

Our description incorporates molecular motors such as Eg5 or Ncd as motor particles and passive cross-linkers, like for example Ase1, as passive particles, see Fig. 3.3. Properties of these particles are described in section 1.3. A filament of length L is represented by a linear lattice of $N = L/\Delta$ sites, where $\Delta = 8\,\mathrm{nm}$ corresponds to the size of a tubulin dimer. We enumerate lattice sites starting from the minus-end at $i = 0$ with the filament's plus-end at site $i = N-1$. Motors and passive particles can attach to an empty lattice site at rates $\omega_{\mathrm{m}}^{\mathrm{a}}$ and $\omega_{\mathrm{p}}^{\mathrm{a}}$, respectively. An empty site in this context means that it is not occupied by a particle of any type, corresponding to interspecies steric interactions. Once bound to the filament, particles can detach again

Parameter	Value	Dimensionless value	Reference
Δ	8 nm	1	[67]
γ	$12\,{}^{1}/_{\mathrm{s}}$	1	[180]
D	$860\,{}^{1}/_{\mathrm{s}}$	70	[153]
$\omega_{\mathrm{m}}^{\mathrm{d}}$	$1.56\,{}^{1}/_{\mathrm{s}}$	0.13	[180]
$\omega_{\mathrm{p}}^{\mathrm{d}}$	$0.0017\,{}^{1}/_{\mathrm{s}}$	$1.4{\cdot}10^{-4}$	[123]

Table 3.1: ***In-vitro* parameter values** chosen for the simulations together with reference and rescaled value.

at corresponding rates $\omega_{\mathrm{m}}^{\mathrm{d}}$ and $\omega_{\mathrm{p}}^{\mathrm{d}}$.
Apart from that, a motor at site i can hop at rate γ to site $i+1$, if the latter is empty. Accounting for the diffusive nature of the passive cross-linkers, a passive particle can hop at rate D to any of its neighboring sites, provided that it is not yet occupied by another particle. Motors at site $i = N-1$ can hop off the filament with rate γ as well, whereas passive particles cannot leave the filament via hopping neither at site $i = 0$ nor site $i = N-1$. The equations describing the time evolution of the occupation probabilities M_i and P_i of active and passive particles, respectively, at site i thus read

$$\partial_t M_i = \omega_{\mathrm{m}}^{\mathrm{a}}\,(1 - M_i - P_i) - \omega_{\mathrm{m}}^{\mathrm{d}} M_i + \gamma\left(M_{i-1,\bar{i}} - M_{i,\overline{i+1}}\right) \tag{3.8}$$

and

$$\begin{aligned}\partial_t P_i = {} & \omega_{\mathrm{p}}^{\mathrm{a}}\,(1 - M_i - P_i) - \omega_{\mathrm{p}}^{\mathrm{d}} P_i \\ & + D\left(P_{i-1,\bar{i}} + P_{i+1,\bar{i}} - P_{i,\overline{i+1}} - P_{i,\overline{i-1}}\right)\end{aligned} \tag{3.9}$$

for all sites i. The boundary conditions for motors and passive particles are introduced by defining $M_{N-1,\overline{N}} = M_{N-1}$, $M_{-1,\bar{0}} = 0$ and $P_{0,\overline{-1}} = P_{-1,\bar{0}} = P_{N-1,\overline{N}} = P_{N,\overline{N-1}} = 0$. In Eqs. (3.8) and (3.9), $P_{i,\bar{j}}$ and $M_{i,\bar{j}}$ are the respective probabilities of site i to be occupied by either a passive or motor particle, while site j is empty.

Equations (3.8) and (3.9) are solved stochastically using Gillespie's algorithm[2]. For the rates, known *in vivo* parameters for Ase1 and Eg5 motors are chosen. The hopping rates are $\gamma = 12\,\mathrm{s}^{-1}$ [180] for motor particles and $D = 860\,\mathrm{s}^{-1}$ [153] for passive particles. The detachment rates are $\omega_{\mathrm{m}}^{\mathrm{d}} = 1.56\,\mathrm{s}^{-1}$ for motor particles [180] and $\omega_{\mathrm{p}}^{\mathrm{d}} = 0.0017\,\mathrm{s}^{-1}$ for passive particles [123]. The occupancy rates $\omega_{\mathrm{m}}^{\mathrm{a}}$ and $\omega_{\mathrm{p}}^{\mathrm{a}}$ depend on the concentrations

[2]Details of the algorithm are given in appendix A.

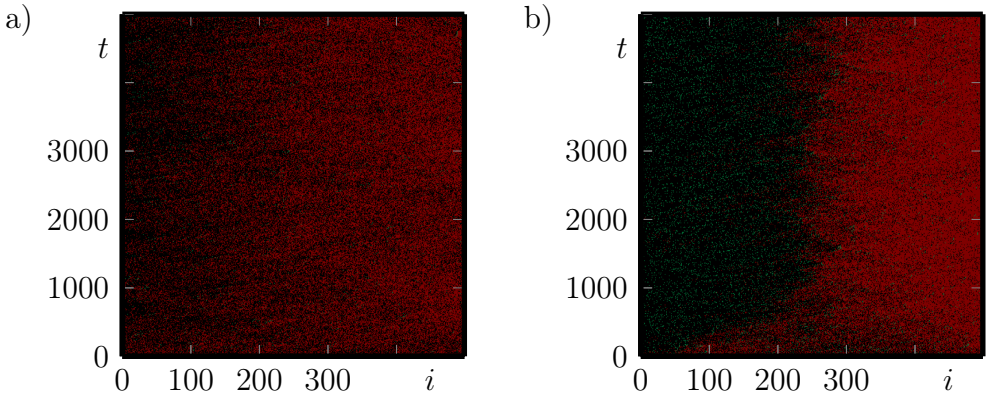

Figure 3.4: **Kymographs** for filaments of length $L = 500$ from stochastic simulations. The states of the filament sites for different times are color coded: empty sites are black, sites occupied by motors green, those occupied by passive particles red. Other parameters are $\omega_{\mathrm{m}}^{\mathrm{a}} = 0.002$ (a), 0.01 (b), $\omega_{\mathrm{p}}^{\mathrm{a}} = 10^{-4}$. From [1], Copyright 2014 by the American Physical Society

of unbound passive and motor particles in the surrounding medium and are used as control parameters. Additionally, length is rescaled with the lattice constant Δ and rates by the hopping rate of motor particles γ. An overview of all rates together with their respective rescaled values can be found in table 3.1. In the rest of this chapter, we only refer to these rescaled quantities. As initial condition, the lattice is occupied uniformly by motor and passive particles with densities $\overline{M}$ and $\overline{P}$, respectively. We choose the values of $\overline{M}$ and $\overline{P}$ to be given by the stationary state of Eqs. (3.8) and (3.9) in the case $\gamma = D = 0$,

$$\overline{P} = \frac{\omega_{\mathrm{m}}^{\mathrm{d}}\omega_{\mathrm{p}}^{\mathrm{a}}}{\omega_{\mathrm{m}}^{\mathrm{d}}\omega_{\mathrm{p}}^{\mathrm{a}} + \omega_{\mathrm{p}}^{\mathrm{d}}\omega_{\mathrm{m}}^{\mathrm{a}}\omega_{\mathrm{m}}^{\mathrm{d}}\omega_{\mathrm{p}}^{\mathrm{d}}} \tag{3.10}$$

for passive particles and

$$\overline{M} = \frac{\omega_{\mathrm{m}}^{\mathrm{a}}\omega_{\mathrm{p}}^{\mathrm{d}}}{\omega_{\mathrm{m}}^{\mathrm{d}}\omega_{\mathrm{p}}^{\mathrm{a}} + \omega_{\mathrm{p}}^{\mathrm{d}}\omega_{\mathrm{m}}^{\mathrm{a}}\omega_{\mathrm{m}}^{\mathrm{d}}\omega_{\mathrm{p}}^{\mathrm{d}}} \tag{3.11}$$

for motor particles.

Kymographs presenting the results of stochastic simulations show that passive particles start to aggregate close to the plus-end whereas motor particles are kept away from the plus-end by large accumulation of passive particles

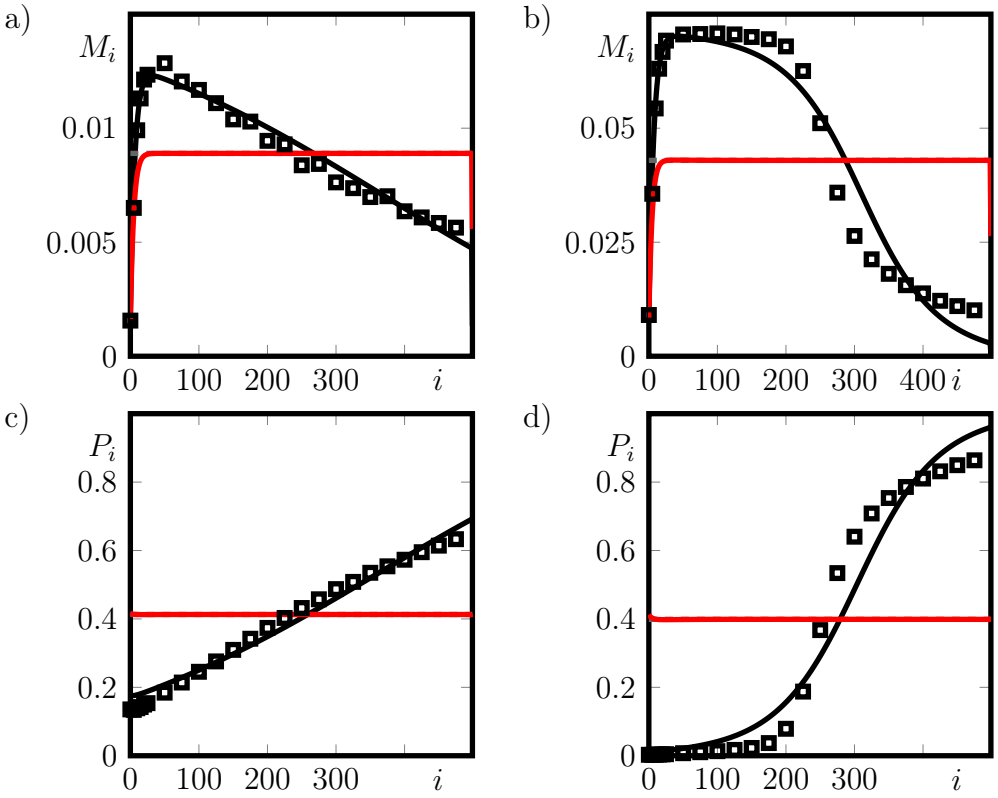

Figure 3.5: **Steady state particle densities** for motors (a,c) and passive particles (b,d). Parameters used are as in Fig. 3.4(a) (a,c) and Fig. 3.4(b) (b,d). Profiles where obtained using 10^7 samples of one simulation at a time distance of $10\gamma^{-1}$. Langmuir densities according to Eqs. (3.11) and (3.11) are plotted as horizontal gray dashed lines. Black lines show analytic meanfield solutions using $\alpha = 0.17 \pm 0.05$ (a,c) and 0.11 ± 0.05 (b,d) and red lines the meanfield solutions for $\alpha = 0$. After [1].

and therefore have a higher density near the minus-end, see Fig. 3.4. This phase separation between regimes of high densities of passive and motor particles is even more pronounced upon an increase of the motor particle concentration $\omega_{\mathrm{m}}^{\mathrm{a}}$, as can be seen by comparing kymographs, see Fig. 3.4(a) and Fig. 3.4(b) as well as particle densities, see Fig. 3.5. For a small motor occupancy rate of $\omega_{\mathrm{m}}^{\mathrm{a}} = 0.002$, the motor density reaches a maximum value larger than $\overline{M}$ close to the minus-end at $i = 0$, after which it decreases monotonically towards the plus-end, see Fig. 3.5(a). The density of passive particles shows a reversed profile. It monotonically increases, with a maximum value larger than $\overline{P}$ attained near the plus-end.

The shapes of the profiles change qualitatively in the case of larger motor

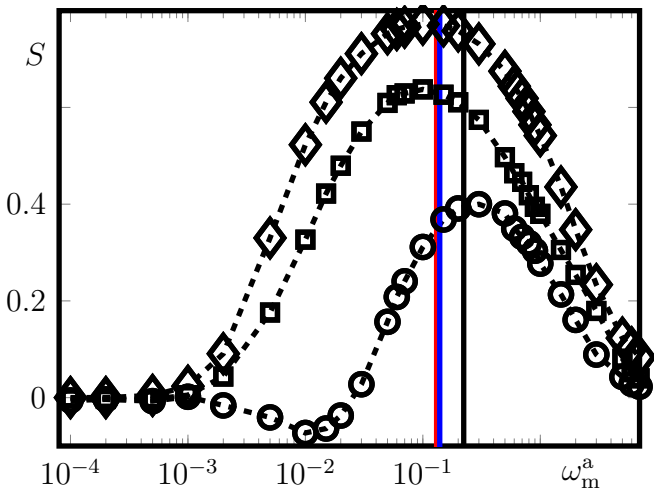

Figure 3.6: **Segregation** S of motors and passive particles for $\omega_{\mathrm{p}}^{\mathrm{a}} = 10^{-6}$ (○), 10^{-5} (□), 10^{-4} (◇) and varying motor attachment rates $\omega_{\mathrm{m}}^{\mathrm{a}}$. Dashed lines between data points serve as guide to the eye. Vertical lines indicate the estimate given by Eq. (3.19) for $\omega_{\mathrm{p}}^{\mathrm{a}} = 10^{-6}$ (red), 10^{-5} (blue), 10^{-4} (black). From [1], Copyright 2014 by the American Physical Society.

concentrations. For $\omega_{\mathrm{m}}^{\mathrm{a}} = 0.01$, the motor density M_i again has its maximum close to the minus-end. Remarkably, a shock-like behavior emerges, similar to the effects described in [92, 94], see also section 2.1. Again, the passive particle density evolves in a reversed way. From the appearance of the domain wall between high and low density regimes of different particle species, we conclude that phase separation can also be seen in this one-dimensional system with passive and motor particles.

In order to quantify the segregation S of the two species, we define

$$S = 1 - \frac{N \sum_{i=0}^{N-1} M_i P_i}{\left(\sum_{i=0}^{N-1} M_i\right)\left(\sum_{i=0}^{N-1} P_i\right)} \tag{3.12}$$

such that $S = 1$ in the case of perfect segregation and $S = 0$ in the case of a homogeneous distribution. Note that $S < 0$ is possible. For varying occupancy rates of passive and active particles, a maximum of the segregation can be found from stochastic simulations, see Fig. 3.6.

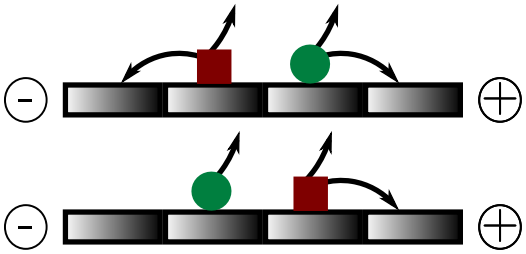

Figure 3.7: **Sketch to explain segregation**. The sketch illustrates the two possible configurations of passive and motor particles neighboring each other. In the upper figure, the motor particle is closer to the plus-end, whereas in the lower figure, it is closer to the minus-end. Arrows indicate possible processes.

The segregation can be understood by looking at neighboring passive and motor particles, see Fig. 3.7. If the motor particle is closer to the plus-end, it can either hop or detach. Similarly, the passive particle can hop and detach. If now the configuration is inverted, the motor particle's hopping is hindered by its steric interaction with the passive particle. Thus, the latter configuration has a longer lifetime.

A passive particle can resolve the first configuration by hopping towards the minus-end, whereas the second configuration can be resolved by hopping of the passive particle in the direction of the plus-end. Due to its larger lifetime, the latter configuration is more likely to occur. Therefore, it is more probable to find passive particles hopping towards the plus-end and motor particles induce a drift of the passive particles towards the plus-end. Since passive particle have a small detachment rate compared to that of motors, they on average travel a long distance along the filament. This large processivity in cooperation with the diffusive barrier leads to accumulation of passive particles at the plus-end. By this aggregation of passive particles, motors are kept away from the plus-end, consequently presenting a higher density near the minus-end.

According to the understanding of segregation given above, it should depend on the processivity of passive and motor particles as well as the diffusive barrier. In fact, the larger the processivity of both particle types, the larger the segregation, see Fig. 3.8. If motors hop as fast as the diffusive particles, the processivity of motors is increased and consequently also the effective processivity of passive particles. Consistent with our explanation of segregation, the separation of regimes of high density of either particle type becomes more pronounced, compare Fig. 3.8(a) and the domain wall between motor

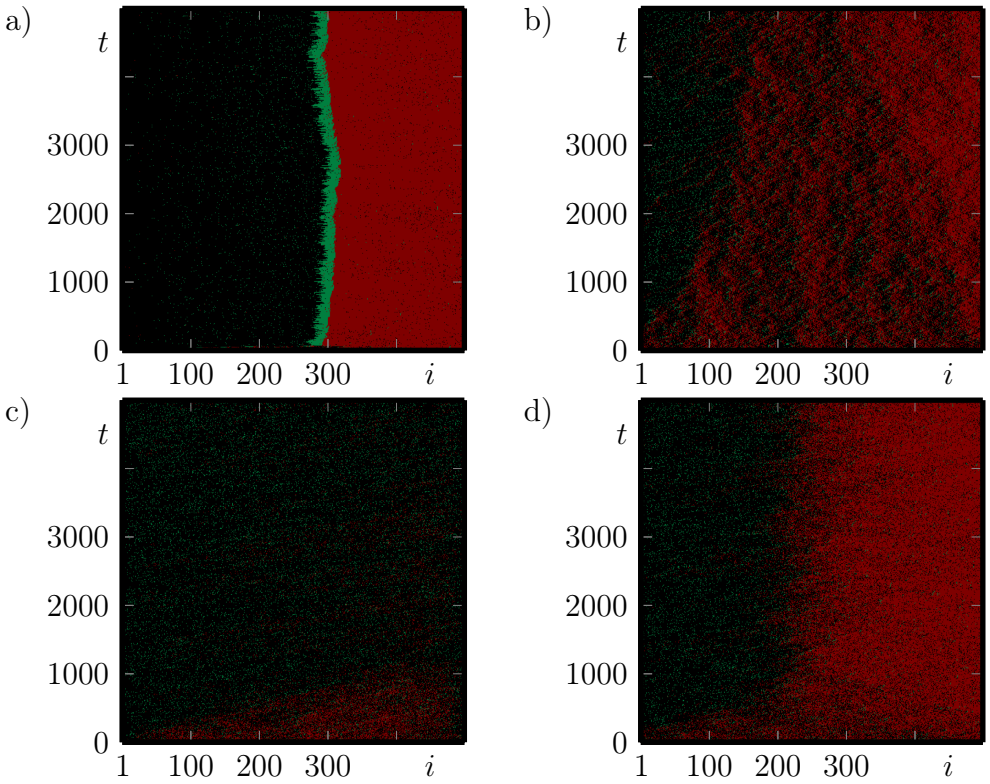

Figure 3.8: **Changing boundary conditions or the hopping rates of particles affects segregation** (a) γ is taken to be the same as the hopping rate of diffusive particles. Other parameters are $\omega_{\mathrm{m}}^{\mathrm{d}} = 1.86 \cdot 10^{-3}$, $\omega_{\mathrm{p}}^{\mathrm{d}} = 2 \cdot 10^{-6}$, $\omega_{\mathrm{m}}^{\mathrm{a}} = 1.43 \cdot 10^{-4}$, $\omega_{\mathrm{p}}^{\mathrm{a}} = 1.43 \cdot 10^{-6}$ (b) D is reduced to the hopping rate of motors. (c) Kymograph without diffusive barrier for passive particles. (d) Kymograph with end barrier for active particles. Parameters for (b-d) as in Fig. 3.4. From [1], Copyright 2014 by the American Physical Society.

and passive particles is steeper than in the case with the original *in-vitro* rates. For the kymograph in Fig. 3.8(b), diffusive particles hop at the speed of active particles. The segregation effect is still present, but less pronounced than in the cases studied before. This is caused by the reduced distance that passive particles travel on average at the reduced hopping rate.
Removal of the diffusive barriers leads to a loss of segregation, see Fig. 3.8(c), since passive particles are driven out of the system and cannot accumulate at the plus-end. Yet, in this situation, diffusive particles cannot be considered passive anymore. Hopping off the filament's ends changes the free energy of the particles, as they are in an unbound state afterwards, which is energetically less favorable than the bound state. For this reason, hopping off the filament ends requires additional energy, which is in contradiction to the

assumption that the diffusive particles are passive.
Introducing a barrier for the motor particles does not qualitatively change the system's behavior, compare Fig. 3.8(d). The density of motor particles is very small close to the plus-end, as this end is already packed with passive particles. Hence changing the boundary condition at the plus-end for motor particles does not lead to differences in the observable behavior of passive and motor particles.

Without interspecies steric interactions, the effect of segregation is lost as the particles evolve independently of each other. The case for motor particles only is already discussed in 2.1. Since passive particles simply diffuse with a reflective boundary at the lattice ends, a constant density profile with $P_i = \overline{P}$ and consequently $S = 0$ is observed, resulting from diffusion of a particle gas in a one-dimensional closed system.
Hence, we are able to identify steric interactions between different species and a diffusive barrier for passive particles as necessary conditions to find segregation.

In addition to the qualitative understanding we have so far, we can get a quantitative understanding of the segregation effect. For this, we apply a meanfield analysis to Eqs. (3.8)–(3.9). To clearly distinguish between the stochastic solution and the meanfield approach, we denote the meanfield densities of motor and passive particles at site i as m_i and p_i, respectively. Following the meanfield *ansatz* also used to solve the TASEP, see section 1.3, we would neglect two-point correlations, $P_{i,\bar{j}} = p_i(1 - p_j - m_j)$ and $M_{i,\bar{j}} = m_i(1 - p_j - m_j)$. Using this *ansatz*, the density profiles given in Fig. 3.5 cannot be approximated, especially no profile with a shock-like shape, see red lines in Fig. 3.5. Instead, two-point correlations between passive and active particles are taken into account by introducing a phenomenological parameter α and rewriting

$$p_{i-1,\bar{i}} = p_{i-1}(1 - p_i - (1 - \alpha)m_i) \ , \tag{3.13}$$

$$p_{i+1,\bar{i}} = p_{i-1}(1 - p_i - (1 + \alpha)m_i) \ , \tag{3.14}$$

and

$$m_{i-1,\bar{i}} = m_{i-1}(1 - (1 + \alpha)p_i - m_i) \ . \tag{3.15}$$

This is equivalent to write interspecies two-point correlations as

$$\langle P_i M_{i+1} \rangle = (1 - \alpha)p_i m_{i+1} \tag{3.16}$$

and

$$\langle M_i P_{i+1} \rangle = (1+\alpha) m_i p_{i+1} \ , \tag{3.17}$$

where $\langle M_i P_{i+1} \rangle$ is the average probability of site i being occupied by a motor particle while site j is occupied by a passive particle. Hence, we quantitatively approximate the asymmetry between the two configurations of passive and motor particles discussed above, see Fig. 3.7.
The value of α can be obtained by fitting the density profiles obtained from the numerical solution of the meanfield theory to the ones obtained from stochastic simulations. The range of accepted values of α is given by those α-values, for which the deviation between the meanfield approximation and the stochastic simulation is less than twice the minimal deviation. An analytic approach to get an estimate of α did not succeed. If we try to explicitly write down the time development of the two-point correlated states, describing the time development of configurations as shown in Fig. 3.7, three-point correlations need to be taken into account. Approximating those via two-point correlations and particle densities on single sites, did not succeed. This is caused by the fact that in motor driven systems, correlations between specific sites close to moving boundaries play a very large role [62]. In this system, each passive particle presents a dynamic boundary to the motor particles.
The results of the meanfield theory are shown in Fig. 3.5 and Fig. 3.9 for varying values of $\omega_{\mathrm{m}}^{\mathrm{a}}$ and $\omega_{\mathrm{p}}^{\mathrm{a}}$ together with the fitted values of α.

Since segregation relies on the effective current of passive particles, which is induced by the current of motor particles, we can estimate to position of the maximum of the segregation value S.
To do so, we approximate the average current of active particles by the steady state Langmuir densities $\overline{M}$ and $\overline{P}$. Similar to the TASEP, the current of particles is then given by

$$\overline{J} = \gamma \overline{M}(1 - \overline{M} - \overline{P}) \ . \tag{3.18}$$

With this equation, we can find the occupancy rate

$$(\omega_{\mathrm{m}}^{\mathrm{a}})^* = \omega_{\mathrm{m}}^{\mathrm{d}} \frac{\omega_{\mathrm{p}}^{\mathrm{d}} + \omega_{\mathrm{p}}^{\mathrm{a}}}{\omega_{\mathrm{p}}^{\mathrm{d}}} \tag{3.19}$$

of motor particles, for which the current $\overline{J}$ is maximized under a given passive particle attachment rate $\omega_{\mathrm{p}}^{\mathrm{a}}$. We get the right order of magnitude for the optimal conditions of the segregation, see vertical lines in Fig. 3.6. This value is

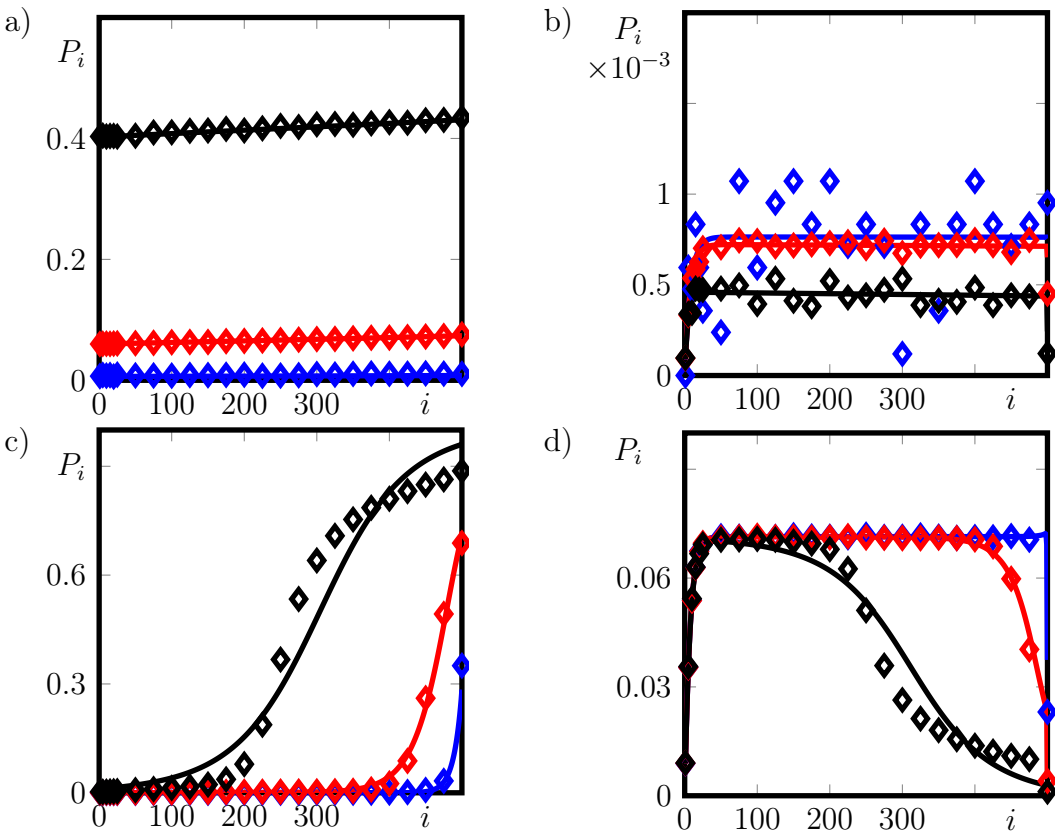

Figure 3.9: **Comparison of the stochastic simulations with the meanfield results.** Density profiles for passive (a,c) and active (b,d) particles using a low density of active particles $\omega_{\mathrm{m}}^{\mathrm{a}} = 10^{-4}$ (a, b) or high density of active particles $\omega_{\mathrm{m}}^{\mathrm{a}} = 10^{-2}$ (c, d). In all cases, $\omega_{\mathrm{p}}^{\mathrm{a}} = 10^{-6}$ (blue), 10^{-5} (red), 10^{-4} (black). Markers present the result of stochastic simulations, solid lines the solution of the meanfield theory using the fit parameter $\alpha = 0.3 \pm 0.2$ (blue), 0.3 ± 0.03 (red) and 0.17 ± 0.08 (black) (a, b) and $\alpha = 0.58 \pm 0.36$ (blue), 0.24 ± 0.06 (red) and 0.11 ± 0.05 (black) (c, d). After [1].

not exact, which is first of all due to the simplicity of the approach, assuming constant density profiles and neglecting two-point correlations. This assumption, as can be inferred from the meanfield theory, is not valid in general. Furthermore, the definition of the segregation value S is not unique, but is introduced to provide a means of quantitatively comparing density profiles for different parameter values.

So far, we have only considered filaments of the same length. Upon variation of the lattice length N, the relative position of the domain wall remains constant. However, the absolute width of the transition region is unaffected by the filament length and thus its relative width decreases for increasing values of N, see Fig. 3.10.
In steady state, on the one hand the pairs of motor and passive particles, leading to an effective drift of passive ones, are mostly found near the domain wall between high and low density of either particle type. The behavior of these pairs determines the fluctuations of the domain wall's position and hence the width of the boundary region. Therefore, its width is not affected by changing N, as long as the lattice is much larger than the width of this region. On the other hand, the position of the domain wall is given by the global influx and outflux of particles together with the densities in the high and low density regime. We can approximate the densities of particles in the low and high density regime to be piecewise constant. The respective values of high and low density of either particle species are given by p_{LD} and p_{HD} for passive particles and m_{LD} and m_{HD} for motor particles, respectively. With this assumption, the total influx Ω of passive particles is given by

$$\Omega = \omega_{\mathrm{p}}^{\mathrm{a}}(1 - a_{\mathrm{LD}} - p_{\mathrm{HD}})(N - x) + \omega_{\mathrm{p}}^{\mathrm{a}}(1 - a_{\mathrm{HD}} - p_{\mathrm{LD}})x \ , \tag{3.20}$$

where x is the position of the domain wall. The outflux $\overline{\Omega}$ is calculated by

$$\overline{\Omega} = \omega_{\mathrm{p}}^{\mathrm{d}} p_{\mathrm{HD}}(N - x) + \omega_{\mathrm{p}}^{\mathrm{d}} p_{\mathrm{LD}} x \ . \tag{3.21}$$

Since in steady state, the flux Ω of particles entering the filament must equal the flux $\overline{\Omega}$ of particles leaving the filament, we find

$$\begin{aligned} &\omega_{\mathrm{p}}^{\mathrm{a}}(1 - a_{\mathrm{LD}} - p_{\mathrm{HD}})(1 - \frac{x}{N}) + \omega_{\mathrm{p}}^{\mathrm{a}}(1 - a_{\mathrm{HD}} - p_{\mathrm{LD}})\frac{x}{N} \\ &\quad = \omega_{\mathrm{p}}^{\mathrm{d}} p_{\mathrm{HD}}(1 - \frac{x}{N}) + \omega_{\mathrm{p}}^{\mathrm{d}} p_{\mathrm{LD}} \frac{x}{N} \ . \end{aligned} \tag{3.22}$$

We do not expect the densities to depend on the lattice size, since it is determined by local effects, namely the interactions of particles. For Eq. (3.22)

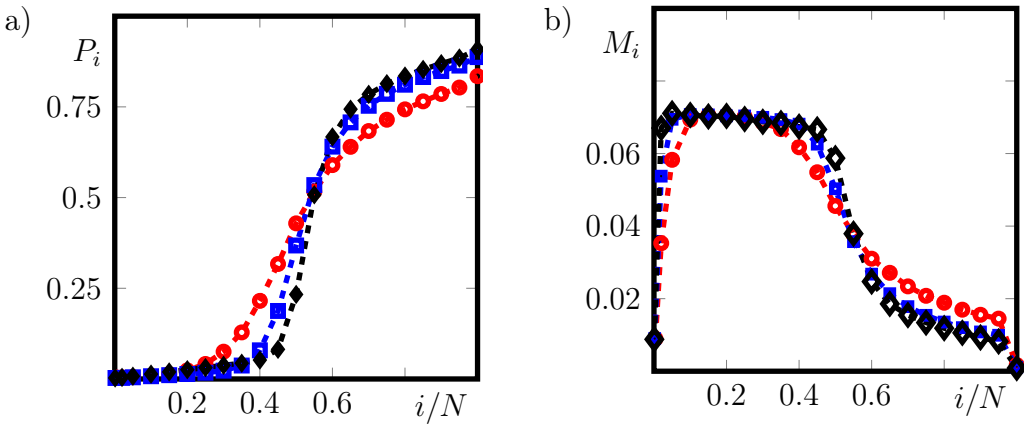

Figure 3.10: **Comparison of the density profiles for varying N.** Density profiles of passive (a) and active (b) particles, $N = 250$ (red), 500 (blue) and 1000 (black). Other parameters as in Fig. 3.4. After [1].

to be valid for all lengths, the relative domain position x/N must not be affected by changing the lattice length N.

Experimental verification of interspecies steric interactions is achieved by measuring the dynamics of individual molecular motors and passive cross-linkers on single microtubules. The experiments described below were performed by Christopher Zapp in the lab of Marcel Janson at the Wageningen university and research center, supervised by Aniek Jongerius and analyzed by Christopher Zapp and me.
First, microtubules are attached to a surface, as described in section 2.3. After that, the chamber is rinsed with a buffer containing various concentrations of ATP, Ase1 and Dk4mer, a molecular motor [181]. The fluorescently labeled proteins Ase1 and Dk4mer are imaged at 1 Hz frame rate for approximately two minutes per measurement.
Protein densities are extracted from time-averaged images by scanning fluorescence intensity along filaments. Then we rescale all profiles to the same length and make an ensemble average over all filaments. The average fluorescence intensity profile does not allow us to show if particles are driven towards one specific end, since we do not know the microtubules' polarization. Yet, if segregation is present, we expect maxima of the filament density near both ends and minima in the middle of the filaments, whereas we should find approximately homogeneous particle distributions otherwise.
Protein tracks are determined from image time series using FIESTA, a particle tracking algorithm [182]. With these tracks we can analyze the mean

square displacement $\sigma(t)$, see Eq. (3.1), of individual particles in the course of time. We expect

$$\sigma_{\text{ballistic}}(t) = v^2 t^2 \tag{3.23}$$

for a directionally moving particle of velocity v and

$$\sigma_{\text{diffusive}}(t) = 2Dt \ . \tag{3.24}$$

for a diffusive particle of diffusion constant D. This is true as long as the measurement times are sufficiently short, such that intraspecies particle interactions do not affect the mean square displacement, see section 3.1. The proteins observed in our measurements usually do not present a purely passive or ballistic behavior. Therefore, we use a superposition

$$\tilde{\sigma} = \sigma_0 + 2Dt + v^2 t^2 \tag{3.25}$$

of ballistic and diffusive behavior. The offset σ_0 accounts for inaccuracy in the determination of the initial position of a particle as well as neither ballistic nor diffusive behavior on time scales shorter than the temporal resolution of our measurements. The spatial resolution of the microscope used in the experimental setup is $160\,{}^{\text{nm}}/_{\text{pixel}}$. Since the signal of individual proteins typically extends over several pixels, we expect values of σ_0 in the order of $10^5\,\text{nm}^2$. For measurements with Ase1 only, we expect $v \approx 0$ and $D \approx 5.5 \cdot 10^4\,{}^{\text{nm}^2}/_{\text{s}}$ [123]. For Dk4mer, we expect a velocity in the order of several hundred nanometers per second [181], depending on the concentration of ATP in the buffer, which is 5 mM for all experiments presented here. We rescale concentrations of Ase1 and Dk4mer by the respective protein concentrations $[\text{Ase1}]_0$ and $[\text{Dk4mer}]_0$ of the stock solutions.

Initial measurements with pure Dk4mer in buffer result in an average particle velocity[3] $v = 329(17)\,{}^{\text{nm}}/_{\text{s}}$, see Fig. 3.11(a), which is comparable to literature values. For Ase1 only, we find $D = 5.7(7) \cdot 10^4\,{}^{\text{nm}^2}/_{\text{s}}$ with a negligible velocity of $v = 36(17)\,{}^{\text{nm}}/_{\text{s}}$, see Fig. 3.11(b). This is in perfect agreement with previous measurements. If Ase1 and Dk4mer are in buffer together, the average motor velocity is reduced upon an increase of the concentration of Ase1, see Fig. 3.11(c). For Ase1, the average densities show pronounced maxima close to the filament ends in presence of Dk4mer, that are not visible without molecular motors, see Fig. 3.12(a). The height of this peaks increases for increasing concentration of Dk4mer. The decay of the intensity towards the

[3]Error range for 95 % confidence interval. Fits are always obtained by fitting $\ln(\tilde{\sigma})$.

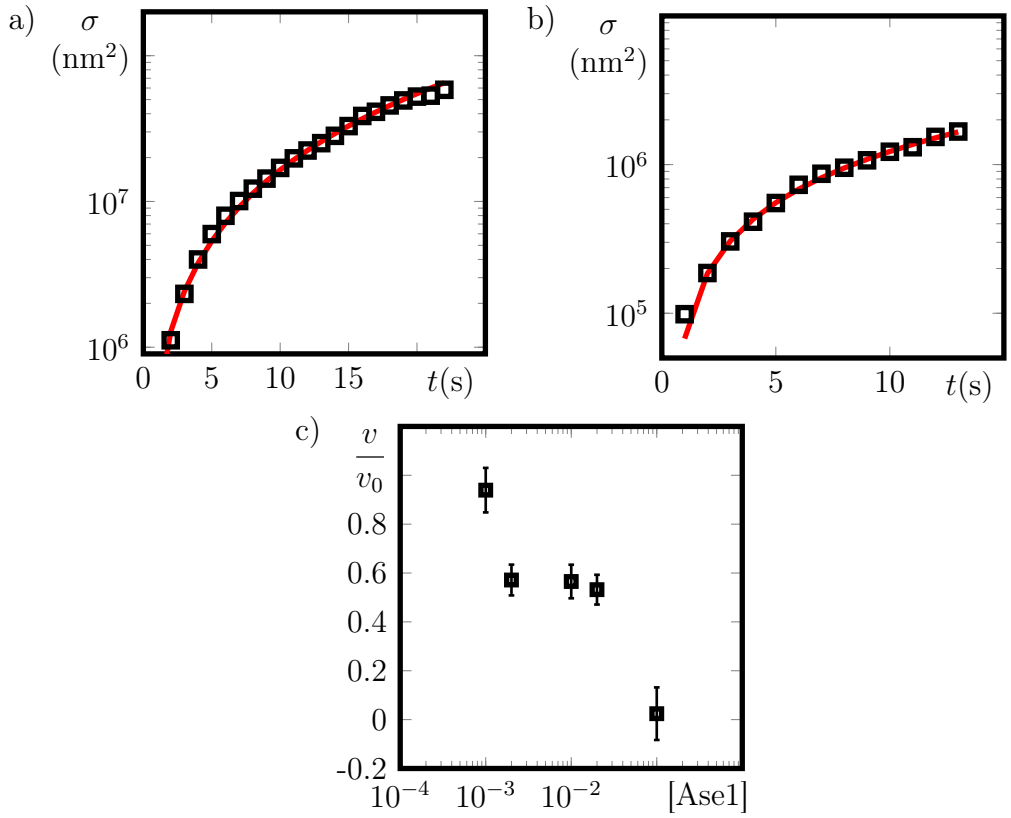

Figure 3.11: **Experimental results** from mean square displacement. (a,b) Mean square displacement $\sigma(t)$ of Dk4mer (a) and Ase1 (b) together with fit of $\tilde{\sigma}$ (red lines). (a) [Dk4mer] = 10^{-4}, [Ase1] = 0, data from 257 particles. Fit parameters: $v = 329(17)\,\mathrm{nm/s}$, $D = 3.0(7) \cdot 10^5\,\mathrm{nm^2/s}$ and $s0 = -3.5(15) \cdot 10^5\,\mathrm{nm^2}$. (b) [Ase1] = 10^{-4}, [Dk4mer]=0, data from 98 particles. Fit parameters: $v = 36(17)\,\mathrm{nm/s}$, $D = 5.7(7) \cdot 10^4\,\mathrm{nm^2/s}$ and $s0 = -4.7(15) \cdot 10^4\,\mathrm{nm^2}$. (c) Relative velocity v/v_0 of Dk4mer for $v_0 = 329(17)\,\mathrm{nm/s}$ and [Dk4mer]=10^{-4}.

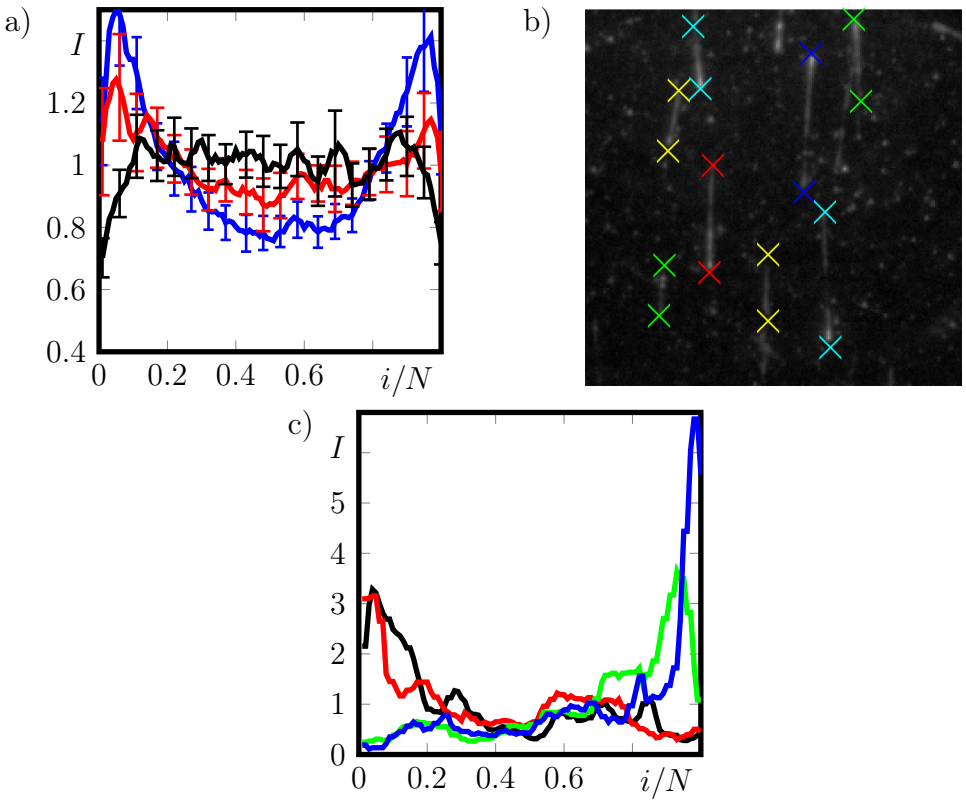

Figure 3.12: **Experimental results for Ase1**. (a) Average fluorescence intensity I of Ase1 along microtubules for [Ase1]=$2 \cdot 10^{-4}$ and [Dk4mer]=0 (black), 0.04 (red) and 0.1 (blue). Intensities are rescaled with the total intensity. Averaged values from 66 (black), 40 (red) and 79 (blue) filaments. (b) Fluorescence intensity of Ase1. Microtubule ends indicated by crosses of different colors. Total image size is $33.6\,\mu$m $\times$ $33.6\,\mu$m. [Ase1]=$2 \cdot 10^{-4}$, [Dk4mer]=0.1. Fluorescence intensity averaged over 121 images. (c) Time averaged fluorescence intensity I of Ase1 along four selected microtubules (different colors). Intensity is rescaled with the respective total intensity along individual filaments. Protein concentrations as in (b).

filament ends results from the inaccuracy in determining the filament-end positions from images of Rhodamine-labeled tubulin. The fluorescence images show that Ase1 preferentially accumulates in proximity of one end of individual microtubules in presence of Dk4mer, see Fig. 3.12(b,c). Analyzing the induced drift of passive particles is not possible in this setup, since fluctuations of the passive particles in general cover any directed drift.
Nonetheless, our experiments support the assumption that steric interactions between passive particles and molecular motors exist. We can clearly observe an influence of each of the particle types on the dynamics of the other one, either a reduced gliding velocity of motors or accumulation of passive particles at one filament end. Both phenomena qualitatively agree with what we expect to observe in presence of steric interactions, based on the theoretical description discussed above.

3.4 Discussion

In section 3.3, we introduce a system describing the interaction of directionally moving motor particles with diffusive passive particles. This description allows us to identify steric interactions between passive and motor particles and additionally a diffusive barrier for the passive particles, as necessary prerequisites for segregation of species along the filament. We find that steric interactions lead to an effective drift of passive particles in the direction of movement of motor particles.
We quantify segregation and find a non-monotonic dependence on attachment rates of particles. The optimal parameter values for segregation can be estimated by considering Langmuir densities of motors and passive particles and maximizing the current of active particles.
In order to quantitatively understand the origin of segregation, we apply a meanfield analysis using a phenomenological parameter to account for two-point correlations between neighboring motors and passive particles. The meanfield approach approximates the results from stochastic simulations, if the phenomenological parameter is fitted.

Segregation of species has been studied in colloid systems [177, 178, 183] and for different kinds of directionally moving particles [86, 95]. Yet, this study is the first to explicitly consider interactions between diffusive and directionally moving particles in one dimension and investigate the impact of boundary conditions.
The diffusive barrier for Ase1 has been observed *in vitro* [153]. Experiments

on molecular motors only suggest that at least intraspecies steric interactions are plausible [60, 184]. A lack of interspecies steric interactions would lead to an immediate loss of both the segregation effect and the effective drift of passive particles. Therefore, our theoretical description introduced and analyzed in this chapter allows to falsify or support the assumption of steric interactions by *in-vitro* experiments. Results from our measurements on Ase1 and the molecular motor Dk4mer support the assumption of steric interactions between different particle species. Motors are slowed down upon addition of Ase1, while Ase1 proteins accumulate towards one end of their respective filament in presence of Dk4mer.

The current experimental setup does not allow to clearly observe segregation. First of all, we have not been able to label the tubules in a way to identify the filaments' polarization. Fluorescently labeling filament nucleators would in principle allow to measure the filaments' orientation directly. On top of that, the resolution of the experimental setup is limited by time duration of the measurement due to photobleaching and the resulting limited number of images that can be made, as well as the spatial resolution of the microscope. These limits only allow us to clearly identify domain walls and phase separation at high densities of Ase1 and Dk4mer. However, we find that Ase1 at high densities generates immobile clusters that do not allow to observe any drift or segregation. At the same time, large Dk4mer concentrations induce buckling of the microtubules, because Dk4mer generates cross-links between filaments and the substrate and induces stresses. The next step in the experiments could be to identify other pairs of diffusive and directionally moving particles that show drift phenomena, possibly enabling us to quantitatively compare segregation in theory and experiment.
Additionally, further experiments should investigate, if steric interactions between different particle species are a general phenomenon for a class of particles or if they only exist for specific particle types.
Future theoretical studies of this system could extend the meanfield theory or provide a different analytical description, explicitly accounting for correlations between neighboring passive and motor particles without a phenomenological parameter. Furthermore recent experiments suggest that particles are able to circumvent obstacles by changing the protofilaments they move along [184]. Nonetheless, steric interactions on individual protofilaments would still lead to segregation or passive drift of particles. For several protofilaments, we would only expect quantitative differences between the drift velocities of passive and motor particles.
Apart from that, experiments by Bieling et al. [129] indicate that passive

particles in overlaps may recruit motors or members of one species transport particles of the other one. These additional interactions could also be incorporated besides intraspecies interactions such as oligomerization, where several proteins of the same species form less mobile clusters on the filament, as has been proposed by Braun et al. [153] and observed in our experiments as well.

In the next chapter, we shift our attention again to the original problem underlying this study, namely pairs of filaments, which are cross-linked by proteins.

Chapter 4

Overlaps between antiparallel filaments induced by the interplay of molecular motors and diffusive cross-linkers

In this chapter, we introduce a theoretical description of two antiparallel filaments cross-linked via molecular motors and passive cross-linkers. We show, that stable finite overlaps of different size can be generated. The dependence of the overlap length on particle concentrations, both without and with steric interactions between the different particle types, is investigated. Afterwards, the forces generated are studied in detail, allowing for a comparison to recent experiments [154]. The results on filament pairs are extended to a coarse-grained theory for bundles of filaments.
The results presented in sections 4.1 and 4.2 have been partially published in [2].

4.1 Generation of stable overlaps

Based on the experiments discussed in section 2.3 and similar in spirit to the theories presented in chapters 2 and 3, we first introduce a particle-based stochastic model for cross-linking molecular motors and passive cross-linkers, see Fig. 4.1.
A filament of length L is described as a linear lattice of $N = L/\Delta$ sites with lattice constant Δ corresponding to the size of a tubulin dimer. The plus-

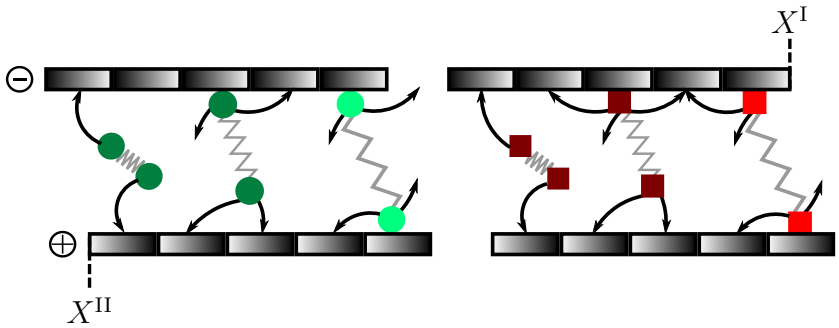

Figure 4.1: **Sketch of the theoretical description.** Possible processes are displayed for motors (green) and passive cross-linkers (red) on separate filament pairs for clarity. Bright colors indicate cross-linked proteins, dark colors are used for particles with an unbound partner particle. The filaments' plus-end positions are X^{I} and X^{II}, respectively. After [2].

end of the filament is at site $i = 0$ and the minus-end corresponds to site $i = N - 1$. The positions of the plus-ends of the two antiparallel lattices **I** and **II** are given by X^{I} and X^{II}, respectively and the quantity

$$\ell = X^{\mathrm{I}} - X^{\mathrm{II}} \ . \tag{4.1}$$

corresponds to the overlap length λ, if $\ell \leq L$. In general, the overlap length is given by

$$\lambda = L - |L - \ell| \ . \tag{4.2}$$

Motor proteins and passive cross-linkers are each described as two identical particles connected via a linear spring of stiffness k_{m} or k_{p}, respectively. The head of an unbound protein can bind to any site i of one of the lattices provided that it is not yet occupied by another particle of the same species. The associated rate is $\omega_{\mathrm{m}}^{\mathrm{a}}$ for motor particles and $\omega_{\mathrm{p}}^{\mathrm{a}}$ for passive particles. Once attached to the filament, the partner particle of the bound particle can bind to an empty site j of the opposite lattice. The spring extension

$$\xi = (i + j)\Delta - \ell \tag{4.3}$$

at binding is distributed normally. This represents that the free head diffuses in the harmonic potential given by the cross-linker spring. The associated cross-linking rate is

$$\omega_{\mathrm{m}}^{\mathrm{c}}(\xi) = \overline{\omega_{\mathrm{m}}^{\mathrm{c}}} \exp\left(\frac{\xi^2}{2\sigma^2}\right) / \sqrt{2\pi\sigma^2} \tag{4.4}$$

for motors and

$$\omega_{\mathrm{p}}^{\mathrm{c}}(\xi) = \overline{\omega_{\mathrm{p}}^{\mathrm{c}}} \exp\left(\frac{\xi^2}{2\sigma^2}\right) / \sqrt{2\pi\sigma^2} \tag{4.5}$$

for passive cross-linkers. Proteins with both particles attached to a lattice are referred to as cross-linked proteins. A bound partner can detach from the lattice at rates

$$\omega_{\mathrm{m}}^{\mathrm{d}}(\xi) = \overline{\omega}_{\mathrm{m}}^{\mathrm{d}} \exp\left|\frac{k_{\mathrm{m}}\xi}{\overline{f}_{\mathrm{m}}}\right| \tag{4.6}$$

and

$$\omega_{\mathrm{p}}^{\mathrm{d}}(\xi) = \overline{\omega}_{\mathrm{p}}^{\mathrm{d}} \exp\left|\frac{k_{\mathrm{p}}\xi}{\overline{f}_{\mathrm{p}}}\right| \ , \tag{4.7}$$

with characteristic forces $\overline{f}_{\mathrm{p}}$ and $\overline{f}_{\mathrm{p}}$. Particles with an unbound partner leave the lattice at rates $\overline{\omega}_{\mathrm{m}}^{\mathrm{d}}$ and $\overline{\omega}_{\mathrm{p}}^{\mathrm{d}}$, corresponding to the situation of no additional force acting on the proteins.

A motor particle can hop at rate $\overline{\gamma}$ towards its neighboring site in direction of the plus-end if it is not yet occupied by another motor particle. If the partner particle is also bound, the hopping rate γ is influenced, as presented in section 1.3. Motivated by the essentially exponential force-velocity dependence, as shown in Fig. 1.6 for high concentrations of ATP, we assume

$$\gamma(\xi) = \overline{\gamma} \exp\left(\frac{k_{\mathrm{m}}\xi}{\overline{f}_{\mathrm{m}}}\right) \ , \tag{4.8}$$

Equation (4.8) allows for arbitrarily large hopping rates, but the simulations we performed have never shown large spring extensions. Either filament sliding or the increased detachment rate of particle heads, see Eq. (4.6), prevent unphysiologically large hopping rates. A particle at site $i = 0$ can always hop at the same rate as a bulk particle, simultaneously detaching from the lattice.

Passive particles can hop as well. As long as the partner particle is not yet bound, the hopping rate to any neighboring site that is not yet occupied by another passive article is $\overline{D}$. If the partner particle is bound, the hopping rates $D^{\pm}$ towards the plus- or minus-end of the respective filament are given as

$$D^{\pm}(\xi) = \overline{D} \exp\left(\pm\frac{k_{\mathrm{p}}\xi}{\overline{f}_{\mathrm{p}}}\right) \ . \tag{4.9}$$

Passive particles cannot leave the lattice via hopping.

To write down the master equation for the system, we introduce the quantities M_i and P_i describing the probability of site i on lattice **I** to be occupied by either a motor or a passive particle with an unbound partner. Similarly, M_i^j and P_i^j describe the probability of a particle bound to site i of lattice **I** with the partner particle bound to site j on lattice **II**. In this context, $M_{i,\overline{k}}$, $M^j_{i,\overline{k}}$, $P_{i,\overline{k}}$ and $P^j_{i,\overline{k}}$ describe probabilities of respective particles bound to site i of lattice **I** while site k of lattice **I** is not occupied by a particle of the same species. Finally, we define $M_i^{\overline{j}}$ and $P_i^{\overline{j}}$ as the probability of site i to be occupied by a motor or passive particle with an unbound partner while site j on lattice **II** is not occupied by a particle of the same species. Similar quantities for lattice **II** are denoted via a hat, implying $P_i^j = \hat{P}_j^i$ and $M_i^j = \hat{M}_j^i$. With these notations, the equations[1] describing the stochastic system introduced above are given by

$$\begin{aligned}\frac{d}{dt}M_i = {}& \overline{\gamma}M_{i+1,\overline{i}} - \overline{\gamma}M_{i,\overline{i-1}} + \gamma(\xi)M_i^0 \\ & - \overline{\omega}_{\mathrm{m}}^{\mathrm{d}}M_i + \omega_{\mathrm{m}}^{\mathrm{a}}(1 - M_i - \sum_j M_i^j) - \sum_j I_i^j \end{aligned} \tag{4.10}$$

and

$$\begin{aligned}\frac{d}{dt}M_i^j = {}& \gamma(\xi+\Delta)M^j_{i+1,\overline{i}} - \gamma(\xi)M^j_{i,\overline{i-1}} \\ & + \gamma(\xi+\Delta)\hat{M}^i_{j+1,\overline{j}} - \gamma(\xi)\hat{M}^i_{j,\overline{j-1}} \\ & + I_i^j + \hat{I}_j^i \end{aligned} \tag{4.11}$$

for motor particles with

$$I_i^j = \omega_{\mathrm{m}}^{\mathrm{c}}(\xi)M_i^{\overline{j}} - \omega_{\mathrm{m}}^{\mathrm{d}}(\xi)M_i^j \tag{4.12}$$

describing the formation and disbanding of cross-links between the lattices. The third term in Eq. (4.10) describes hopping off of a motor particle at site $i = 0$ of lattice **II** while its partner particle remains attached to lattice **I**. For passive particles, the corresponding equation is

[1] Only the time evolution for the quantities M_i, P_i, M_i^j and P_i^j are given here explicitly. The equations for higher order terms and quantities on lattice **II** follow straightforward.

Parameter	Value	Dimensionless value	Reference
Δ	8 nm	1	[67]
$\overline{\gamma}$	$12\,\mathrm{s}^{-1}$	1	[180]
$\overline{D}$	$12\,\mathrm{s}^{-1}$	1	[153]
$\overline{\omega}_{\mathrm{m}}^{\mathrm{d}}$	$1.56\,\mathrm{s}^{-1}$	0.13	[180]
$\overline{\omega}_{\mathrm{p}}^{\mathrm{d}}$	$0.0017\,{}^{1}/_{\mathrm{s}}$	$1.4{\cdot}10^{-4}$	[123]
$\overline{\omega}_{\mathrm{m}}^{\mathrm{c}}$	$8.4\,\mathrm{s}^{-1}$	0.7	-
$\overline{\omega}_{\mathrm{p}}^{\mathrm{c}}$	$1.2\,\mathrm{s}^{-1}$	0.1	-
$k_{\mathrm{m,p}}$	$0.11\,{}^{\mathrm{pN}}/_{\mathrm{nm}}$	0.1	-
σ	8 nm	1	-
μ	$0.1\,{}^{\mathrm{pNs}}/_{\mathrm{nm}}$	1	-
$\overline{f}_{\mathrm{m,p}}$	9 pN	1	[180]
L	800 nm	100	-

Table 4.1: ***In-vitro* parameter values** chosen for the simulations together with the used rescaled values and source, if available.

$$\begin{aligned}\frac{d}{dt}P_i &= \overline{D}(P_{i+1,\bar{i}} + P_{i-1,\bar{i}} - P_{i,\overline{i-1}} - P_{i,\overline{i+1}}) \\ &\quad - \overline{\omega}_{\mathrm{p}}^{\mathrm{d}} P_i + \omega_{\mathrm{p}}^{\mathrm{a}}(1 - P_i - \sum_j P_i^j) - \sum_j J_i^j \ , \qquad (4.13)\\ \frac{d}{dt}P_i^j &= D^+(\xi+\Delta)P^j_{i+1,\bar{i}} - D^+(\xi)P^j_{i,\overline{i-1}} \\ &\quad + D^+(\xi+\Delta)\hat{P}^i_{j+1,\bar{j}} - D^+(\xi)\hat{P}^i_{j,\overline{j-1}} \\ &\quad + D^-(\xi-\Delta)P^j_{i-1,\bar{i}} - D^-(\xi)P^j_{i,\overline{i+1}} \\ &\quad + D^-(\xi-\Delta)\hat{P}^i_{j-1,\bar{j}} - D^-(\xi)\hat{P}^i_{j,\overline{j+1}} + J_i^j + \hat{J}_j^i \qquad (4.14)\end{aligned}$$

with

$$J_i^j = \omega_{\mathrm{p}}^{\mathrm{c}}(\xi)P_i^{\bar{j}} - \omega_{\mathrm{p}}^{\mathrm{d}}(\xi)P_i^j \ . \qquad (4.15)$$

Equations (4.10)-(4.15) are valid for any given values of i and j, if the boundary conditions for motors and passive cross-linkers are incorporated as $M_{0,\overline{-1}} = M_0$, $M_{N,\overline{N-1}} = 0$, $M^j_{0,\overline{-1}} = M_0^j$ and $M^j_{N,\overline{N-1}} = 0$ to account for the motors' ability to leave the lattice via hopping as well as $P_{-1,\bar{0}} = P_{0,\overline{-1}} = P_{N,\overline{N-1}} = P_{N-1,\bar{N}} = 0$ and $P^j_{-1,\bar{0}} = P^j_{0,\overline{-1}} = P^j_{N,\overline{N-1}} = P^j_{N-1,\bar{N}} = 0$, representing the diffusive barrier for passive particles.
The positions of the filaments are changed by the force dipoles generated by

the individual motors, hence

$$\dot{X}^{\mathrm{I}} = \mu \sum_i (f_{\mathrm{m},i} + f_{\mathrm{p},i}) = -\dot{X}^{\mathrm{II}} \ . \tag{4.16}$$

Therefore, the overlap length ℓ changes according to

$$\dot{\ell} = 2\mu \sum_i (f_{\mathrm{m},i} + f_{\mathrm{p},i}) \ . \tag{4.17}$$

Since $f_{\mathrm{m},i}$ and $f_{\mathrm{p},i}$ in Eqs. (4.16) and (4.17) reflect the force dipoles generated by the particles bound to site i on lattice $\mathbf{I}$, they are calculated by summing up all force dipoles generated by individual cross-linkers. Cross-links are implemented as linear springs, so the force dipoles are given by

$$f_{\mathrm{m},i} = k_{\mathrm{m}} \sum_j \xi M_i^j \tag{4.18}$$

and

$$f_{\mathrm{p},i} = k_{\mathrm{p}} \sum_j \xi P_i^j \ , \tag{4.19}$$

respectively.
This completes the description of the system. Equations (4.11)- (4.15) are solved stochastically using Gillespie's algorithm[2]. As parameters, known *in-vitro* values of Eg5 and Ase1 are chosen if available. The bare hopping rate of motor particles is $\overline{\gamma} = 12\,\mathrm{s}^{-1}$ [180], the hopping rate of passive cross-linker heads is set to the same rate[3]. The detachment rate is $\overline{\omega}_{\mathrm{m}}^{\mathrm{d}} = 1.56\,\mathrm{s}^{-1}$ [180] for motors and $\overline{\omega}_{\mathrm{p}}^{\mathrm{d}} = 0.0017\,\mathrm{s}^{-1}$ [123] for passive cross-linkers. The cross-linking rates are set to $\overline{\omega}_{\mathrm{m}}^{\mathrm{c}} = 8.4\,\mathrm{s}^{-1}$ for motors and $\overline{\omega}_{\mathrm{p}}^{\mathrm{c}} = 1.2\,\mathrm{s}^{-1}$ for passive cross-linkers. We choose the spring stiffness $k_{\mathrm{m}} = k_{\mathrm{p}} = 0.11\,{}^{\mathrm{pN}}\!/_{\mathrm{nm}}$ and as characteristic forces $\overline{f}_{\mathrm{m}} = \overline{f}_{\mathrm{p}} = 9\,\mathrm{pN}$ [180]. If not mentioned explicitly, the filament has a length of 800 nm with friction coefficient $\mu = 0.1\,{}^{\mathrm{pNs}}\!/_{\mathrm{nm}}{}^{4}$. The width $\sigma = 8\,\mathrm{nm}$ of the distribution of cross-linker extensions at cross-linking is the same as the lattice constant.

[2]Details of the algorithm are given in appendix A.

[3]The *in-vitro* value of $\overline{D}$ is $860\,\mathrm{s}^{-1}$ [153]. Reducing the value of $\overline{D}$ reduces simulation time significantly, whereas the results are not changed qualitatively. We still observe well regulated finite overlaps for varying occupancy rates of motors and passive cross-linkers.

[4]Varying the friction coefficient by four orders of magnitude, both higher or lower values, did not show any change in the average length of the overlap or the fluctuations around the average value

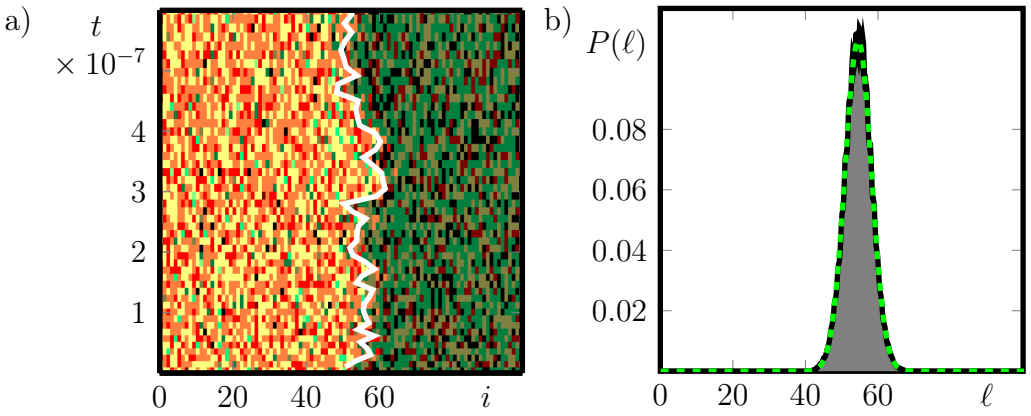

Figure 4.2: **Kymograph and overlap distribution** in absence of steric interactions. (a) Kymograph. Only the configuration of lattice **II** is shown. Empty sites are black, sites occupied by motor particles are green, those occupied by passive particles are labeled in red. Bright colors indicate cross-linking particles. The white line indicates ℓ, corresponding to the position of the plus-end of lattice **I**. (b) Distribution $P(\ell)$ of overlap lengths for $N = 100$ and 10^7 samples. The green line is a Gaussian of same mean and width. Parameters: $\omega_{\mathrm{m}}^{\mathrm{a}} = 0.316$, $\omega_{\mathrm{p}}^{\mathrm{a}} = 10^{-4}$. (b) from [2], Copyright 2015 by the American Physical Society.

We rescale all rates by the hopping rate of motors $\overline{\gamma}$, forces by the characteristic force $\overline{f}_{\mathrm{m}}$ and length by the lattice constant Δ. All rates together with their rescaled value can also be found in table 4.1.
In the rest of the text, we only refer to the rescaled values unless dimensions are mentioned explicitly. The attachment rates $\omega_{\mathrm{m}}^{\mathrm{a}}$ and $\omega_{\mathrm{p}}^{\mathrm{a}}$ in general depend on the concentration of free proteins in the surrounding medium and are therefore used as control parameters.

Kymographs obtained from stochastic simulations for $\omega_{\mathrm{m}}^{\mathrm{a}} = 0.316$ and $\omega_{\mathrm{p}}^{\mathrm{a}} = 10^{-4}$ show that a stable partial overlap can be generated, see Fig. 4.2(a). Independent of the initial system configuration, the same overlap is obtained after a transient phase until the steady state overlap is achieved. The only requirement is an initial overlap of finite length. In steady state, the fluctuations of the overlap length are symmetric to the mean value, and the distribution of overlap lengths is in this case Gaussian, see Fig. 4.2(b).
Longer filaments do not lead to a larger overlap, see Fig. 4.3(a), whereas for filaments shorter than the original steady state overlap, a full overlap is generated in steady state, see Fig. 4.3(b).

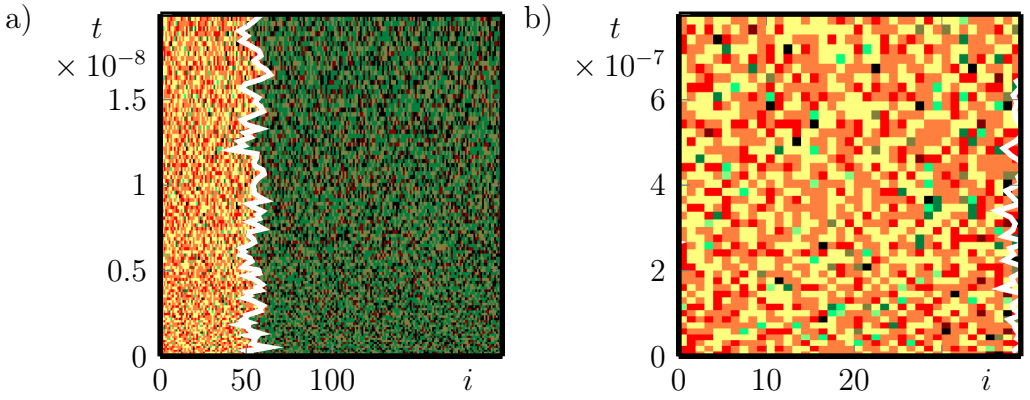

Figure 4.3: **Kymographs for varying filament length** $N = 200$ (a) and 40 (b). Other parameters and presentation as in Fig. 4.2(a).

To understand the origin of the stable partial overlap, consider two antagonistic forces. Passive cross-linkers generate a force which is independent of the overlap length and tries to increase the overlap. Molecular motors generate a length dependent force that diminishes the overlap. The reason for the forces lies within the dynamics of particle hopping and cross-linking.
Both binding and movement of passive cross-linkers inside the overlap are symmetric, hence the average spring extension $\langle \xi \rangle$ vanishes and similarly the force $f_{\mathrm{p},i}$. Nevertheless, this symmetry is broken at the filament ends, see Fig. 4.4. In this situation, there are more cross-linker configurations possible that increase the overlap, leading to an effective force by passive cross-linkers maximizing the overlap.
The same binding asymmetry exists for motors as well. However, the hopping of motors is not symmetric. Since motor particles hop directionally, they generate force dipoles that diminish the overlap. The result is an effective force by motors in the bulk, reducing the overlap length. The amplitude

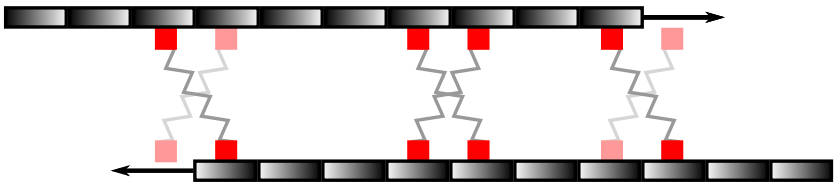

Figure 4.4: **Illustration of the origin of the force exerted by passive cross-linkers**. In the bulk, both configurations that increase and decrease the overlap are equally possible. At the ends, the configuration that would decrease the overlap is not possible (faded colors), hence only the opposing configuration remains, generating a force dipole that increases the overlap (arrows).

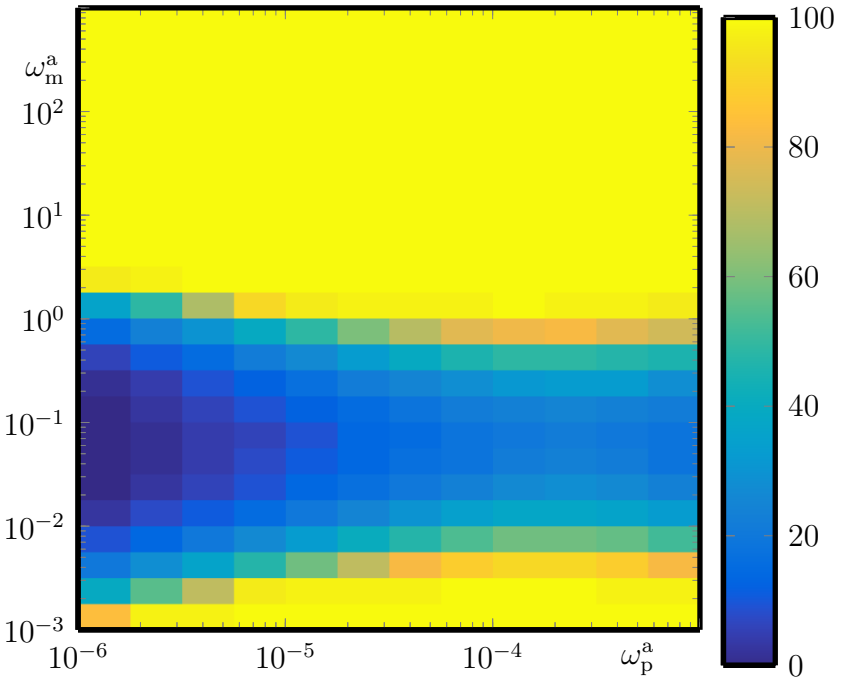

Figure 4.5: **Phase diagram** for varying concentration of motors and passive cross-linkers. Colors indicate the typical overlap length obtained from stochastic simulations averaged over 10^7 samples taken at intervals of $10\gamma^{-1}$. Blue presents vanishing overlaps, yellow full overlap, see color bar. From [2], Copyright 2015 by the American Physical Society.

of the total force generated by the motors in general scales with ℓ. Only if the density of motor particles is so high that hopping is essentially blocked, the end asymmetry due to cross-linking overcomes the bulk effect. This explains the large overlaps observed for high motor concentration in the phase diagram, see Fig. 4.5.

The interplay of the forces generated by motors and passive cross-linkers leads to the generation of stable finite overlaps of various length, see Fig. 4.5. With increasing values of $\omega_{\mathrm{p}}^{\mathrm{a}}$, the region of finite overlaps shrinks. The force pulling the filaments together increases due to the larger concentration of passive cross-linkers. Therefore, larger currents of active particles are necessary to generate forces sufficiently large to compensate for the force by passive cross-linkers.

In order to get a quantitative understanding of overlap length regulation, we apply a meanfield *ansatz*. First of all, the lattices are identical, hence

in steady state, the densities on both lattices are symmetric. Using the symmetry between the two lattices, we can write $M_i = \hat{M}_i$, $M_i^j = \hat{M}_i^j$, $P_i = \hat{P}i$, and $P_i^j = \hat{P}_i^j$. If we furthermore neglect correlations between neighboring sites and denote meanfield quantities by minuscules, Eqs. (4.10)–(4.15) can be rewritten as

$$\begin{aligned}\frac{d}{dt}m_i &= \overline{\gamma}m_{i+1}(1 - m_i - \sum_j m_i^j) \\ &\quad - \overline{\gamma}m_i(1 - m_{i-1} - \sum_j m_{i-1}^j) \\ &\quad + \gamma(\xi)m_i^0 - \overline{\omega}_{\mathrm{m}}^{\mathrm{d}}m_i \\ &\quad + \omega_{\mathrm{m}}^{\mathrm{a}}(1 - m_i - \sum_j m_i^j) - \sum_j I_i^j, \end{aligned} \tag{4.20}$$

and

$$\begin{aligned}\frac{d}{dt}m_i^j &= \gamma(\xi + \Delta)m_{i+1}^j(1 - m_i - \sum_j m_i^j) \\ &\quad - \gamma(\xi)m_i^j(1 - m_{i-1} - \sum_j m_{i-1}^j) \\ &\quad + \gamma(\xi + \Delta)m_i^{j+1}(1 - m_j - \sum_k m_j^k) \\ &\quad - \gamma(\xi)m_i^j(1 - m_{j-1} - \sum_k m_{j-1}^k) + I_j^i + I_i^j \end{aligned} \tag{4.21}$$

$$\tag{4.22}$$

with

$$I_i^j = \omega_{\mathrm{m}}^{\mathrm{c}}(\xi)m_i(1 - m_j - \sum_k m_j^k) - \omega_{\mathrm{m}}^{\mathrm{d}}(\xi)m_i^j \tag{4.23}$$

for motor particles. Similarly, for passive particles follows

$$\begin{aligned}\frac{d}{dt}p_i &= \overline{D}(p_{i+1} + p_{i-1})(1 - p_i - \sum_j p_i^j) \\ &\quad - p_i(2 - p_{i-1} - \sum_j p_{i-1}^j - p_{i+1} - \sum_j p_{i+1}^j) \\ &\quad - \overline{\omega}_{\mathrm{p}}^{\mathrm{d}}p_i + \omega_{\mathrm{p}}^{\mathrm{a}}(1 - p_i - \sum_j p_i^j) - \sum_j J_i^j, \end{aligned} \tag{4.24}$$

$$\tag{4.25}$$

$$\begin{aligned}\frac{d}{dt}p_i^j &= (D^+(\xi+\Delta)p_{i+1}^j + D^-(\xi-\Delta)p_{i-1}^j)(1-p_i-\sum_j p_i^j)\\ &+ (D^+(\xi+\Delta)p_i^{j+1} + D^-(\xi-\Delta)p_i^{j-1})(1-p_j-\sum_k p_j^k)\\ &- D^+(\xi)p_i^j(1-p_{i-1}-\sum_j p_{i-1}^j)\\ &- D^+(\xi)p_i^j(1-p_{j-1}-\sum_k p_{j-1}^k)\\ &- D^-(\xi)p_i^j(1-p_{i+1}-\sum_j p_{i+1}^j)\\ &- D^-(\xi)p_i^j(1-p_{j+1}-\sum_k p_{j+1}^k) + J_i^j + J_j^i \end{aligned} \tag{4.26}$$

with

$$J_i^j = \omega_{\mathrm{p}}^{\mathrm{c}}(\xi)p_i(1-p_j-\sum_k p_j^k) - \omega_{\mathrm{p}}^{\mathrm{d}}(\xi)p_i^j \ . \tag{4.27}$$

The forces are calculated using Eqs. (4.18) and (4.19). The meanfield equations can be solved numerically using a standard forward Euler scheme together with an adaptive step size control. The solution shows that the densities both of motors and passive cross-linkers are approximately piecewise constant with plateaus in the bulk of the overlap as well as in the non-overlapping region of the filament, see Fig. 4.6(a-d). The force by passive cross-linkers, see Fig. 4.6(e), essentially vanishes in the overlap region, with pronounced peaks at the ends of either of the lattices. Motors generate an approximately constant force inside the overlap region, compare Fig. 4.6(f). The force shows a small peak at the lattice ends originating from the effectively asymmetric cross-linking events, similar to passive cross-linkers. The peak in the case of motors is less pronounced than for passive particles, because motors lack a diffusive barrier and are not moving symmetrically, but directionally.

If we fix the overlap length and measure the forces produced by motors and passive cross-linkers, we find that the force generated by passive cross-linkers vanishes if $\ell = 0$, see Fig. 4.7(a). Towards increasing overlap length, the force increases towards its maximum value, with essentially constant force for a large range of overlaps. For full overlap, the force vanishes again, with a sharp decrease in the force profile close to $\ell = N$.

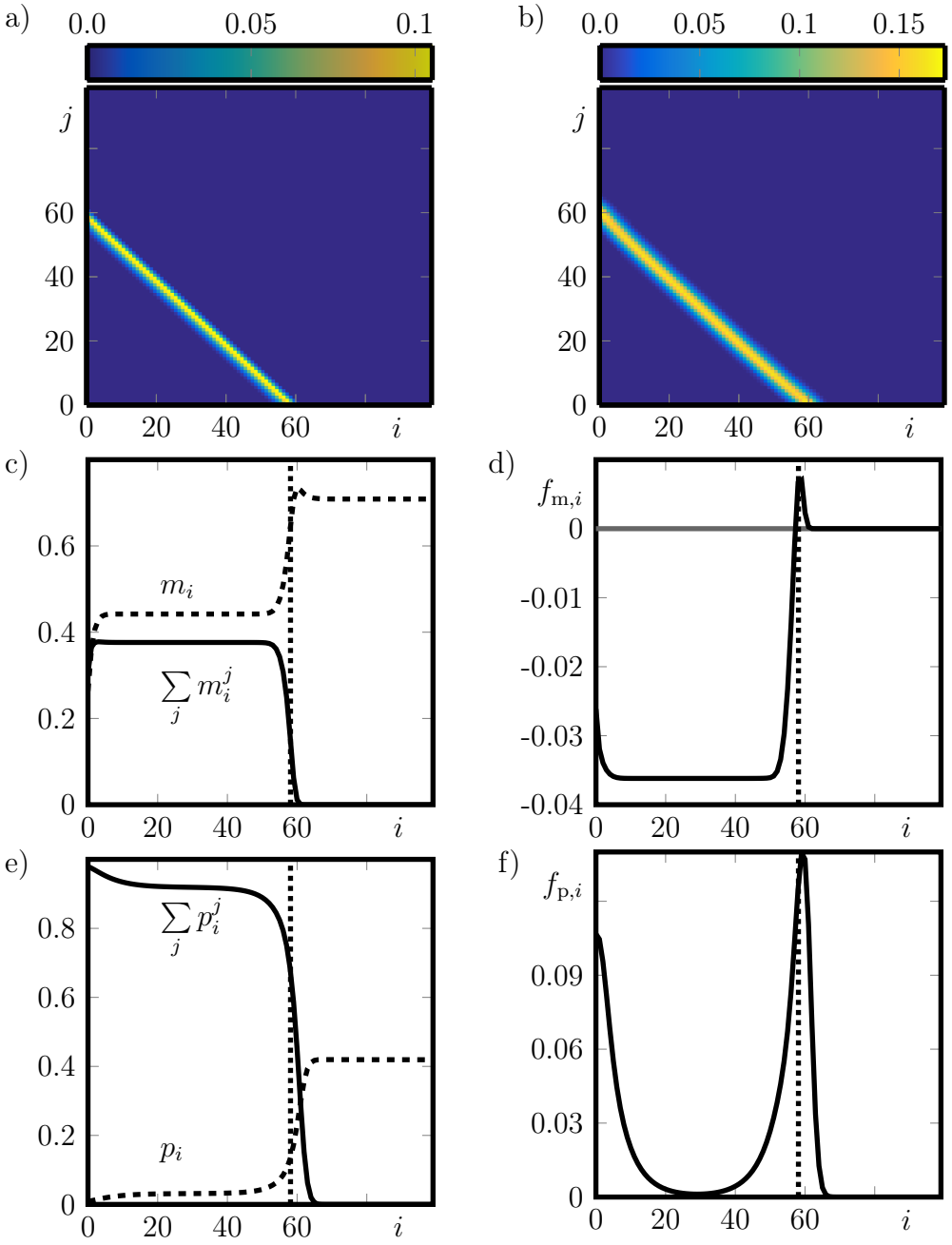

Figure 4.6: **Solution of the meanfield theory**. (a, b) Densities m_i^j (a) and p_i^j (b) indicated by colors, see respective color bars. (c, d) Density of motors (c) and passive particles (d) particles with an unbound (dashed line) or bound (solid line) partner particle. (d, f) Force generated by motors (d) and passive cross-linkers (f). The gray line in (d) indicates vanishing force. The vertical dotted lines in (c-f) indicate the calculated value of $\ell = 58.1$. Parameters as in Fig. 4.2. After [2].

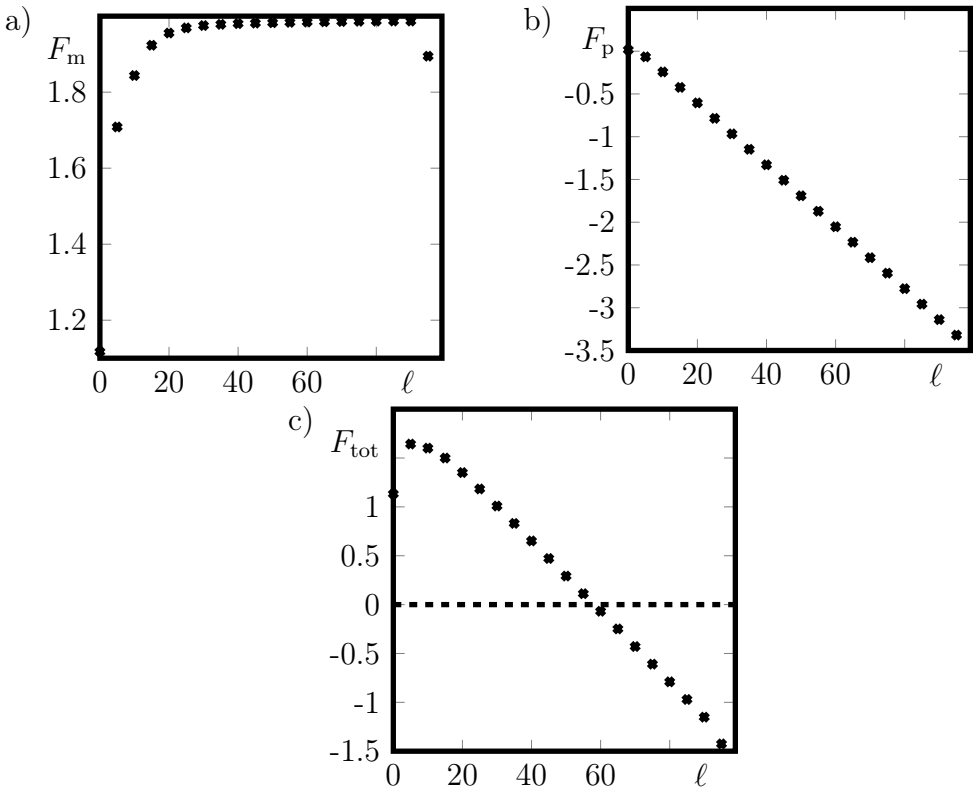

Figure 4.7: **Meanfield solution - Forces** for different fixed overlap ℓ. (a) Total force $F_\mathrm{p} = \sum_{i=1}^{N} f_{\mathrm{p},i}$ by passive cross-linkers. (b) Total force $F_\mathrm{m} = \sum_{i=1}^{N} f_{\mathrm{m},i}$ by motors. (c) Combined force $F_\mathrm{tot} = F_\mathrm{p} + F_\mathrm{m}$. The horizontal dashed line indicates vanishing force. Parameters as in Fig. 4.6.

The force generated by motors is almost proportional to the overlap length, see Fig. 4.7(b), with a negative slope reflecting that motors reduce the overlap between antiparallel filaments. Yet, for $\ell = 0$, a positive force is observed, resulting from the asymmetry in cross-linking, as described above.

The superposition of the forces by passive cross-linkers and motors shows that the total force acting on an overlap of length ℓ is essentially linear for sufficiently large overlaps, see Fig. 4.7(c) and can be described as $F_\mathrm{tot} = \alpha - \beta\ell$, with positive parameters α and β. The steady state overlap that is observed if ℓ is not fixed, can be retrieved by determining the overlap, for which the total force vanishes.

The phase diagram 4.8 obtained from the meanfield equations reproduces

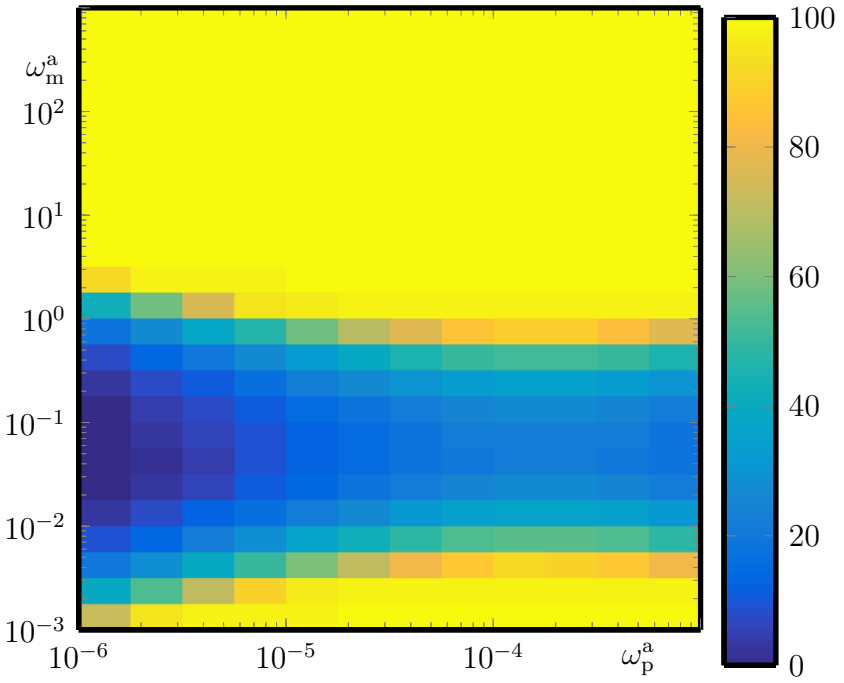

Figure 4.8: **Phase diagram for varying concentration of motors and passive cross-linkers**. Colors indicate the steady-state overlap length obtained from numerically solving the meanfield equations. Blue presents vanishing overlaps, yellow full overlap. From [2], Copyright 2015 by the American Physical Society.

all characteristic features of the original phase diagram 4.5 obtained from stochastic simulations. The quantitative agreement is less for very small particle concentrations, where stochastic fluctuations are more prominent.

So far, only the case without steric interactions has been presented. The next section addresses the impact of steric interactions on the generation of stable partial overlaps.

4.2 Steric interactions enable partial overlap generation without cross-linking motors

As shown in chapter 3, steric interactions have an impact on diffusive and directionally moving particles on a single filament. Thus, in this section we investigate the impact of interspecies steric interactions on passive and motor particles cross-linking a pair of antiparallel filaments. We prove that stable

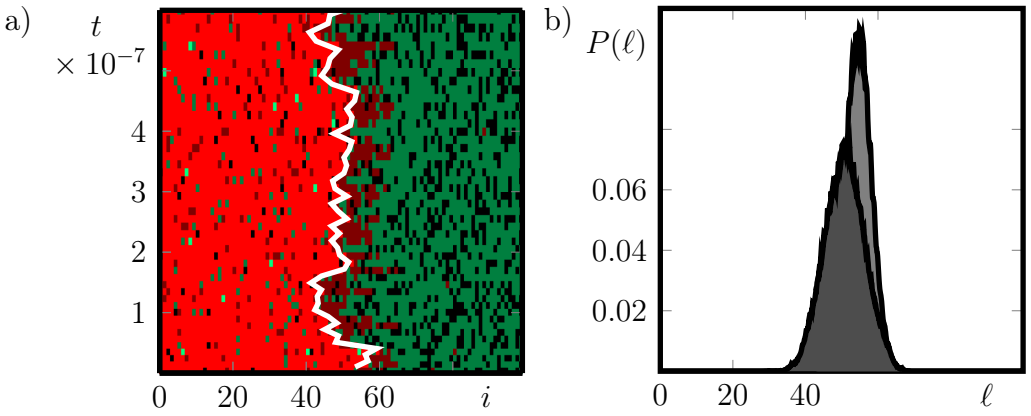

Figure 4.9: **Kymograph and overlap distribution** in presence of steric interactions. (a) Kymograph. Only the configuration of lattice **I** is shown. Empty sites are black, sites occupied by motor particles are green, those occupied by passive particles are labeled in red. Bright colors indicate cross-linking particles. The white line indicates ℓ, corresponding to the position of the plus-end of lattice **I**. (b) Distribution $P(\ell)$ of overlap lengths for 10^7 samples with (dark gray) and without (light gray) steric interactions. Parameters: $\omega_{\mathrm{m}}^{\mathrm{a}} = 0.316$, $\omega_{\mathrm{p}}^{\mathrm{a}} = 10^{-4}$. From [2], Copyright 2015 by the American Physical Society.

overlap generation is in this case even possible in presence of motors that do not cross-link.

The differential equations describing the system are similar to the ones presented in the previous section, although now a site is considered to be empty if no other particle of any of the species is bound.

Kymographs show a similar behavior as in the case without steric interactions for a large range of parameters, compare Figs. 4.2(a) and 4.9(a). Again, in steady state only fluctuations around a stable overlap can be observed. As can be seen from the distribution of overlap lengths, see Fig. 4.9(b), the width of the distribution increases in the case of steric interactions. This is a consequence of additional fluctuations originating from the larger correlations between motors and passive cross-linkers. Same as for the case without interspecies steric interactions, the filament length has no influence on the overlap length, as long as filaments are sufficiently large, see Fig. 4.10.

In the case of large motor occupancy rates, the system shows a qualitatively new behavior, see Fig. 4.11(a). In this parameter regime, the overlap length strongly fluctuates, so it is impossible to properly define a typical overlap length. To explain the origin of these fluctuations, note that on the one hand,

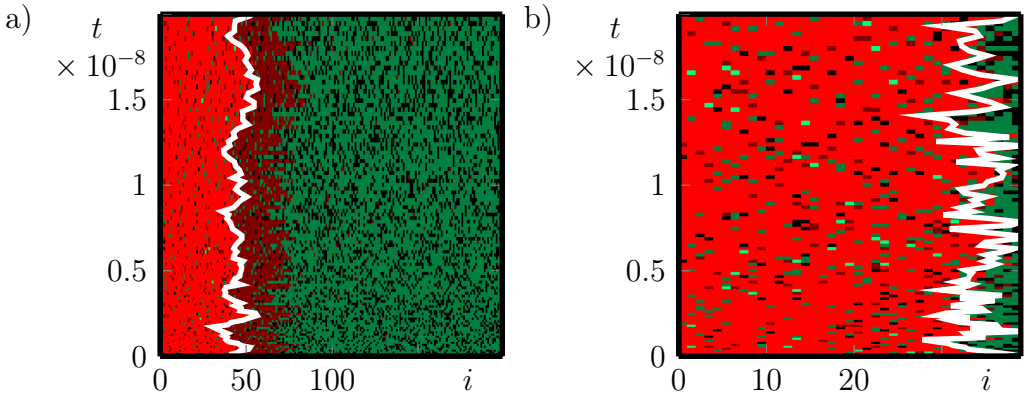

Figure 4.10: **Kymographs for varying filament length** $N = 200$ (a) and 40 (b). Other parameters and presentation as in Fig. 4.9(a).

the movement of motors is essentially blocked due to the large concentration of particles. Therefore, they have an effect comparable to that of passive cross-linkers, namely they generate a full overlap. This can also be seen from the phase diagram in the case without steric interactions, see Fig. 4.5, for large motor occupancy rates as well. On the other hand, due to the increased correlation between motors and passive particles, situations may occur in which a single passive particle or motor generates a cross-link. Since steric interactions lead to a directed drift of passive particles, as described in section 3.3, both types of cross-linkers move similar to a motor cross-linker and effectively reduce the overlap as long as they are cross-linked. These configurations lead to a reduction of the overlap, which increases again after the cross-link disbands.

This is also visible from the fact that the fluctuations in ℓ are asymmetric, such that more situations occur, in which the filaments' plus-ends overlap, as the minus-ends are rarely visible, see solid and dashed white lines in Fig. 4.11. This is because the action of cross-linking molecular motors that hop towards the plus-end favors this orientation of the overlap.

Since without steric interactions, passive particles always favor the generation of a full overlap, these fluctuations cannot be observed in the case without steric interactions as long as $\omega_{\mathrm{p}}^{\mathrm{a}} > 0$. If we consider the case $\omega_{\mathrm{p}}^{\mathrm{a}} = 0$ with motor particles only, the fluctuating phase for large motor concentrations can be observed as well, see Fig. 4.11(b).

The phase diagram in the case of steric interactions includes the phase of large fluctuations described above, see Fig. 4.12. In addition, again stable finite overlaps can be generated and furthermore, the value of the overlap is less sensitive to changes in the occupancy rates of passive cross-linkers and

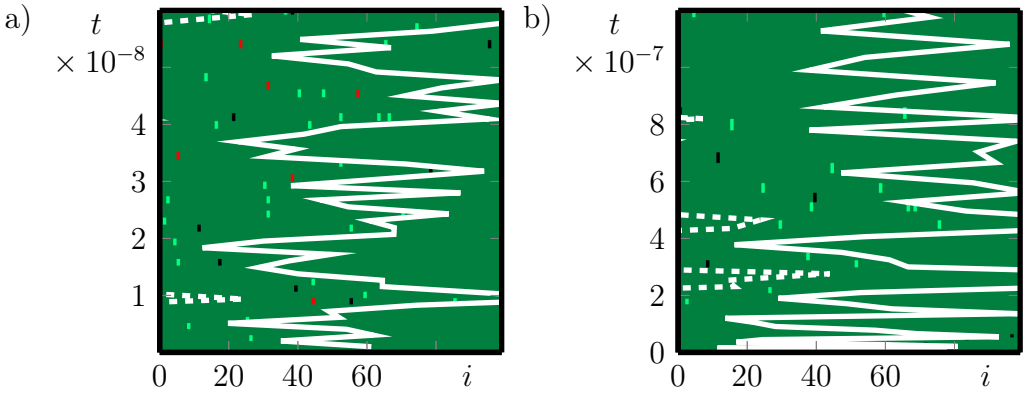

Figure 4.11: **Kymograph of an unstable overlap**. Only the configuration of lattice **I** is shown. Empty sites are black, sites occupied by motor particles are green, those occupied by passive particles are labeled in red. Bright colors indicate cross-linking particles. The white line indicates the position $X^{\mathrm{II}} - X^{\mathrm{I}}$ of the plus-end of lattice **II**. Parameters: $\omega_{\mathrm{m}}^{\mathrm{a}} = 100$, $\omega_{\mathrm{p}}^{\mathrm{a}} = 10^{-4}$ (a), 0 (b). (a) from [2], Copyright 2015 by the American Physical Society.

motors. This could give rise to stabilization against fluctuations in the densities of proteins in the buffer surrounding the filaments.

The drift phenomenon described in section 3.3 as well as the phase of large fluctuations in the overlap length, which can be observed in the case of steric interactions and high particle concentrations, shows that passive cross-linkers can behave comparable to molecular motors. Indeed, in the case $\omega_{\mathrm{m}}^{\mathrm{c}} = 0$, still a stable overlap can be observed and the phase diagram 4.13 resembles that of the case with cross-linking motors $\omega_{\mathrm{m}}^{\mathrm{c}} > 0$. Overlaps for $\omega_{\mathrm{m}}^{\mathrm{a}} \geq 10^2$ are not shown in Fig. 4.13, since the relaxation time of the system is too large to allow for numerical analysis with our stochastic simulations if motor concentrations are large: Only a small amount of cross-links is generated by passive cross-linkers that can serve as force dipole generators changing the overlap towards its possible steady state value.

Although the agreement between the meanfield theory and the stochastic simulations in the case without steric interactions is good, an equivalent approach fails to describe the situation with steric interactions. Similar to the situation on a single filament, see section 3.3, a meanfield approach which neglects two-point correlations is not able to account for the correlations between motors and passive cross-linkers.

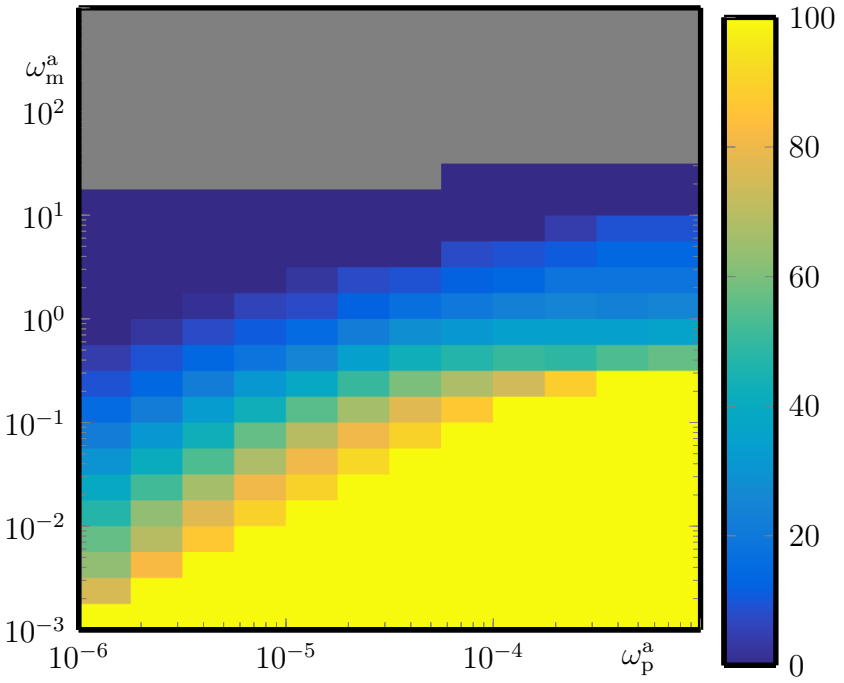

Figure 4.12: **Phase diagram** for varying concentration of motors and passive cross-linkers in presence of steric interactions. Colors indicate the typical overlap length obtained from stochastic simulations averaged over 10^7 samples, taken at intervals of $10\gamma^{-1}$. Blue presents vanishing overlaps, yellow full overlap and gray indicates regimes of large overlap fluctuations. Other parameters as in Fig. 4.5. From [2], Copyright 2015 by the American Physical Society.

For parallel filaments, we find that full overlaps are generated, while similar to the case of a single filament, passive cross-linkers and motors segregate, see Fig. 4.14.

Similar to the case without steric interactions, the generation of stable partial overlaps relies on the action of two antagonistic forces, namely a force component that favors full overlaps and another one, decreasing the overlap. Apart from the phase of large fluctuations, another difference between the situations with and without steric interactions is that passive cross-linkers as well contribute to the force decreasing the overlap, if they interact sterically with motors.

In sections 4.1 and this section, we provide arguments for the origin of the force by passive cross-linkers which ostensibly differ from the one given by Lansky et al. [154], see section 2.3. In the next section, we discuss our

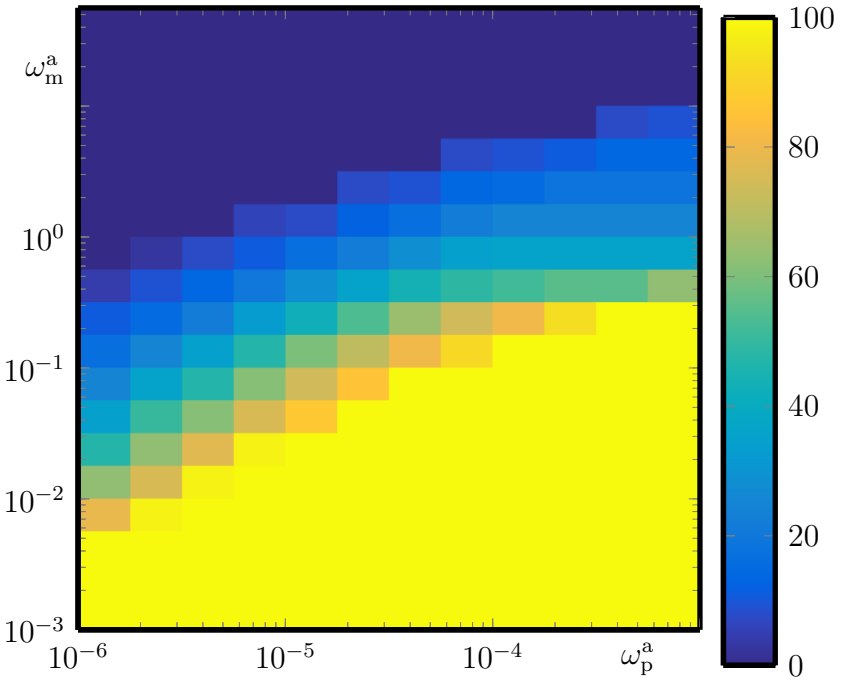

Figure 4.13: **Phase diagram** for varying concentration of not cross-linking motors and passive cross-linkers. Colors indicate the typical overlap length obtained from stochastic simulations averaged over 10^7 samples, taken at intervals of $10\gamma^{-1}$. Blue presents vanishing overlaps, yellow full overlap. Other parameters as in Fig. 4.5.

results in the light of their experimental observations as well as theoretical explanations.

4.3 Comparison of the theoretical description and experimental observations

Passive cross-linkers have been shown to play an important role in the formation of stable overlaps together with molecular motors [138, 153, 154]. A correct theoretical description of a system of passive cross-linkers and molecular motors on a pair of microtubules must be able to explain all observations made in experiments so far. In sections 4.1 and 4.2, we show that the mechanisms incorporated in our model allow for the generation of stable finite overlaps, similar to those observed in experiments. Additionally, in this section we compare our results to the force measurements by Lansky et al. [154] and relate our theoretical description to the argument of an entropic effect, as it is introduced by the authors. References to experiments in this section

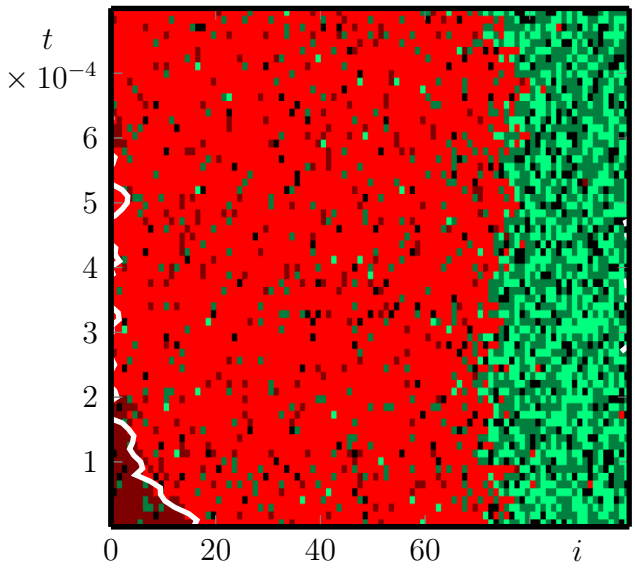

Figure 4.14: **Kymograph of parallel filaments**. Only the state of filament **II** is shown. Parameters as in Fig. 4.9.

always refer to the work on the passive cross-linker Ase1 [154].

In order to measure forces experimentally, one microtubule is attached to a substrate, which is moved via a motorized stage. The other filament has a silica microsphere attached, which is trapped with an optical tweezer to measure the applied forces. A more detailed description of the experimental procedure can be found in section 2.3. The measurement starts with full overlap between the tubules. For each data point, the stage is moved by 50 nm decreasing the overlap. After two seconds to allow for relaxation of the system, the force is measured for ten seconds at 50 kHz rate. Lansky et al. assume the buffer surrounding the filaments to be free of Ase1, since the observation chamber is rinsed with a solution not containing Ase1 prior to the measurement.

In our simulations, this setup is implemented by fixing the position of lattice **I** and applying a harmonic force with spring stiffness K_{ext} to the plus-end of lattice **II**. Displacement d of the stage is performed by changing the harmonic force's rest length X_0. The measurement of the external force f_{ext} starts after a time τ_0. During the measurement, $\mathcal{N}$ samples are taken at intervals τ_1.

Parameter values for particle dissociation and movement are, compared to the values chosen in sections 4.1 and 4.2, changed to those given in the supplemental material of Lansky et al. as far as possible, refer to table 4.2

Parameter	Value	Dimensionless value
$\overline{D}$	$0.1\,\mu\mathrm{m}^2/\mathrm{s}$	130
$\overline{\omega}_\mathrm{p}^\mathrm{d}$	$10^{-4}\,\mathrm{s}^{-1}$	$8.3{\cdot}10^{-6}$
$\overline{\omega}_\mathrm{p}^\mathrm{c}$	$0.5\,\mathrm{s}^{-1}$	0.042
k_p	$0.2\,\mathrm{pN/nm}$	0.18
σ	$2.4\,\mathrm{nm}$	0.3
μ	$23\,\mathrm{pNs/nm}$	230
L	$8\,\mu\mathrm{m}$	1000
K_ext	$0.15\,\mathrm{pN/nm}$	0.15
d	$50\,\mathrm{nm}$	6
$\mathcal{N}$	40000	40000
τ_0	$2\,\mathrm{s}$	24
τ_1	$2\times10^{-4}\,\mathrm{s}$	2.4×10^{-3}

Table 4.2: ***In-vitro* parameter values** chosen for the simulations together the used rescaled value. These parameters are used in section 4.3 if not mentioned explicitly.

for changed values. In [154], the spring stiffness was determined by fitting the diffusion constant of Ase1 in the overlaps to experimental observations. Since the authors do not provide an error range for the fitted value or data supporting their fit, we also use other values for the spring stiffness of passive cross-linkers k_p. To compare the case with and without dissociation of Ase1, we initially occupy the filaments by a given number n of passive cross-linkers. For the case without dissociation of Ase1, both detachment and attachment of particles are neglected, namely $\overline{\omega}_\mathrm{p}^\mathrm{d} = \omega_\mathrm{p}^\mathrm{a} = 0$.

If the number of passive cross-linkers is fixed, the results of the experiments can be reproduced, see Fig. 4.15(a-e). The maxima of the measured forces range from 2.7 pN in the case of one cross-linker to more than 20 pN for $n = 20$ cross-linkers, see Fig. 4.15(a-c,e). The values of the maxima are independent of the cross-linker spring stiffness and only determined by the strength of the harmonic potential K_ext together with the minimum value of the rest length, which is $X_0 = 0$, see gray line in Figs. 4.15(b,e). It is in the same order of magnitude as in experiments, see Fig. 4.15(d). Furthermore, the force decreases monotonically with increasing overlaps and increases with the number of cross-linkers for a given overlap. This is also in line with the experiments.

In order to perform the simulations with a fixed number of cross-linkers, we

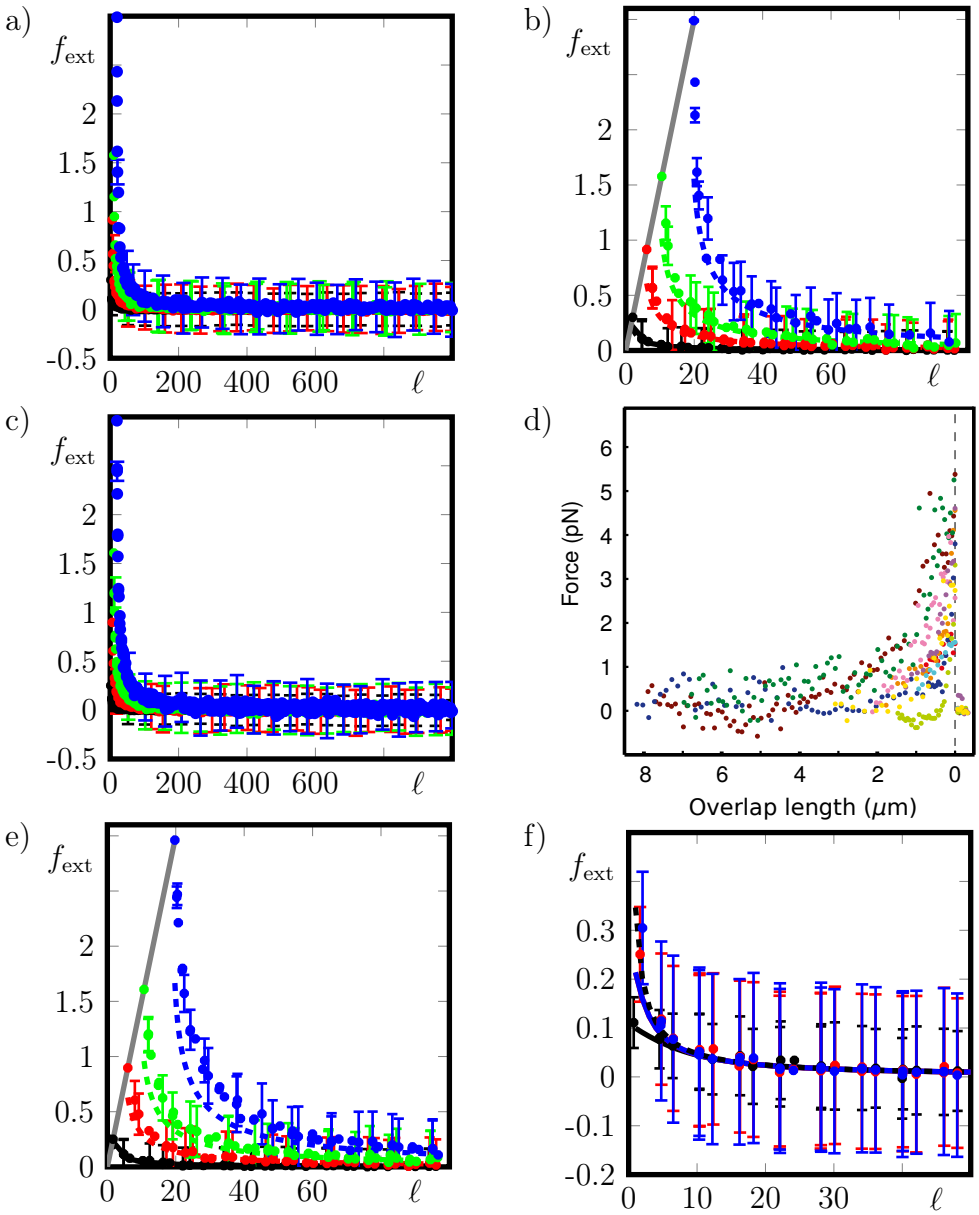

Figure 4.15: **Force for a fixed number of passive cross-linkers**. (a - c, e) Fixed number of $n = 1$ (black), 5 (red) and 10 (green) and 20 (blue) passive cross-linkers with spring stiffness $k_p = 1.6$ (a, b) and 0.18 (c, e) on a filament of length $N = 1000$. Results from measurements as dots with error bars for every 20th data point. Entropic force, see Eq. (2.22), in (b,e) as dashed lines, Maximal force $f_{ext}^{max} = K_{ext}\ell$ that can be measured for rest length $X_0 = 0$ as gray solid line. (d) Experimental results for a filament of the same length (8 μm) and different cross-linker numbers, taken from [154] (changed). Copyright 2015 by Elsevier. (f) Force for varying passive cross-linker spring stiffness $k_p = 0.018$ (black), 0.18 (red) and 1.8 (blue) and $n = 1$. Lines present solutions of Eq. (4.34) (solid lines) and Eq. (2.22) (dashed line).

define $\overline{\omega}_{\mathrm{p}}^{d} = \omega_{\mathrm{p}}^{\mathrm{a}} = 0$, as mentioned above. Hence, the effective temperature of the system is defined by the particle hopping rate, which has to fulfill the Einstein relation

$$k_{\mathrm{B}}T = \frac{D}{\mu} \ , \tag{4.28}$$

where μ is the effective friction coefficient of a passive particle. If we consider a passive cross-linker that is pulled by a force f, the particle's velocity

$$\begin{aligned} v &= \delta\overline{D}\left(\exp(f/\overline{f}_{\mathrm{p}}) - \exp(-f/\overline{f}_{\mathrm{p}})\right) \\ &= 2\delta\overline{D}\sinh(f/\overline{f}_{\mathrm{p}}) \\ &= 2\delta\overline{D}\frac{f}{\overline{f}_{\mathrm{p}}} + \mathcal{O}\left(\left(\frac{f}{f_{\mathrm{p}}}\right)^2\right) \end{aligned} \tag{4.29}$$

is given by the two possible hopping processes, in direction of the force and in the opposite direction. Inserting $D = \overline{D}\delta^2$ and $\mu = f/v$ up to linear order in $f/\overline{f}_{\mathrm{p}}$ into the Einstein relation (4.28) results in

$$k_{\mathrm{B}}T = \frac{f_{\mathrm{p}}\delta}{2} \ . \tag{4.30}$$

With this, we can calculate the entropic force Eq. (2.22) and the solution shows very small deviations for only one particle, see black dashed lines in Fig. 4.15(b,e). For larger particle numbers, the measured force is underestimated, see colored dashed lines in Fig. 4.15(b,e). The deviance between the entropic force and the measured force increases for softer cross-linker springs and larger forces, the relative difference increases up to approximately 40 % of the measured value for the maximum of the force at minimal overlap.
Lansky et al. do not consider the finite spring stiffness of the cross-linkers, therefore their approximation fails to describe situations, when the distribution of spring extensions plays a role. This is the case for densely packed overlap regions, $\ell \gtrapprox n$ or forces in the order of $\overline{f}_{\mathrm{p}}$, the characteristic force of the passive cross-linkers.
If we explicitly consider possible spring extensions of individual cross-linkers and assume that cross-linkers cannot cross each other, the partition function is given by

$$\begin{aligned} Q(n,\ell) = &\sum_{i_0=0}^{N-n}\sum_{j_0=n-1}^{N-1}\exp\left(-\frac{\beta k_{\mathrm{p}}}{2}\xi_1^2\right) \\ &\times\prod_{r=1}^{n-1}\left[\sum_{i_r=i_{r-1}}^{N-n+r}\sum_{j_r=n-r-1}^{j_{r-1}}\exp\left(-\frac{\beta k_{\mathrm{p}}}{2}\xi_r^2\right)\right] \ , \end{aligned} \tag{4.31}$$

where $\beta = 2(\delta\ \overline{f}_{\mathrm{p}})^{-1}$ and $\xi_r = \delta(i_r + j_r) - \ell$ for any index r. The resulting free energy $\mathcal{F}$ and the force f_{ext} follow straightforward:

$$\mathcal{F}(n,\ell) = -\beta^{-1}\ln(Q(n,\ell)) \tag{4.32}$$

$$\tag{4.33}$$

and

$$\begin{aligned} f_{\mathrm{ext}}(n,\ell) &= -\partial_l \mathcal{F}(n,\ell) \\ &= -\beta^{-1} Q(n,\ell)^{-1} \partial_l Q(n,\ell) \\ &= k_{\mathrm{p}} Q(n,\ell)^{-1} \sum_{i_0=0}^{N-n} \sum_{j_0=n-1}^{N-1} \xi_1 \exp\left(-\frac{\beta k_{\mathrm{p}}}{2}\xi_1^2\right) \\ &\times \prod_{r=1}^{n-1} \left[\sum_{i_r=i_{r-1}}^{N-n+r} \sum_{j_r=n-r-1}^{j_{r-1}} \xi_r \exp\left(-\frac{\beta k_{\mathrm{p}}}{2}\xi_r^2\right) \right] \end{aligned} \tag{4.34}$$

We can compare the result of Eq. (4.34) for varying spring stiffness and a single cross-linker, see Fig. 4.15(f). Simulations show a difference between the measured forces for small overlaps, see dots in Fig. 4.15(f). The entropic force is not able to reproduce this difference, because it does not account for finite cross-linker stiffness. Instead, the force dependence, Eq. (4.34), derived above allows us to capture the different force values measured in the simulations.

From this we conclude that Lansky et al. miss a property of cross-linkers, namely their finite spring stiffness, influencing the force generated by passive cross-linkers. Consequently, this force is not purely entropic, but the energetic contribution due to the cross-linkers' spring extensions must be considered, especially if the spring stiffness is below the value assumed by Lansky et al.

However, because the number of necessary computations to calculate f_{ext} numerically increases exponentially with the number of cross-linkers, it is technically impossible to evaluate f_{ext} for $n > 3$.

If unbound Ase1 is present in solution, passive cross-linkers can attach to and detach from the filaments. For the experimental protocol used in [154], the force dependence on the overlap is similar to the case with a fixed number of passive cross-linkers, see Fig. 4.16(a). The time scale of the measurement is well below the typical time scales for particle dissociation, and the assumption of approximately constant cross-linker numbers should be valid. The

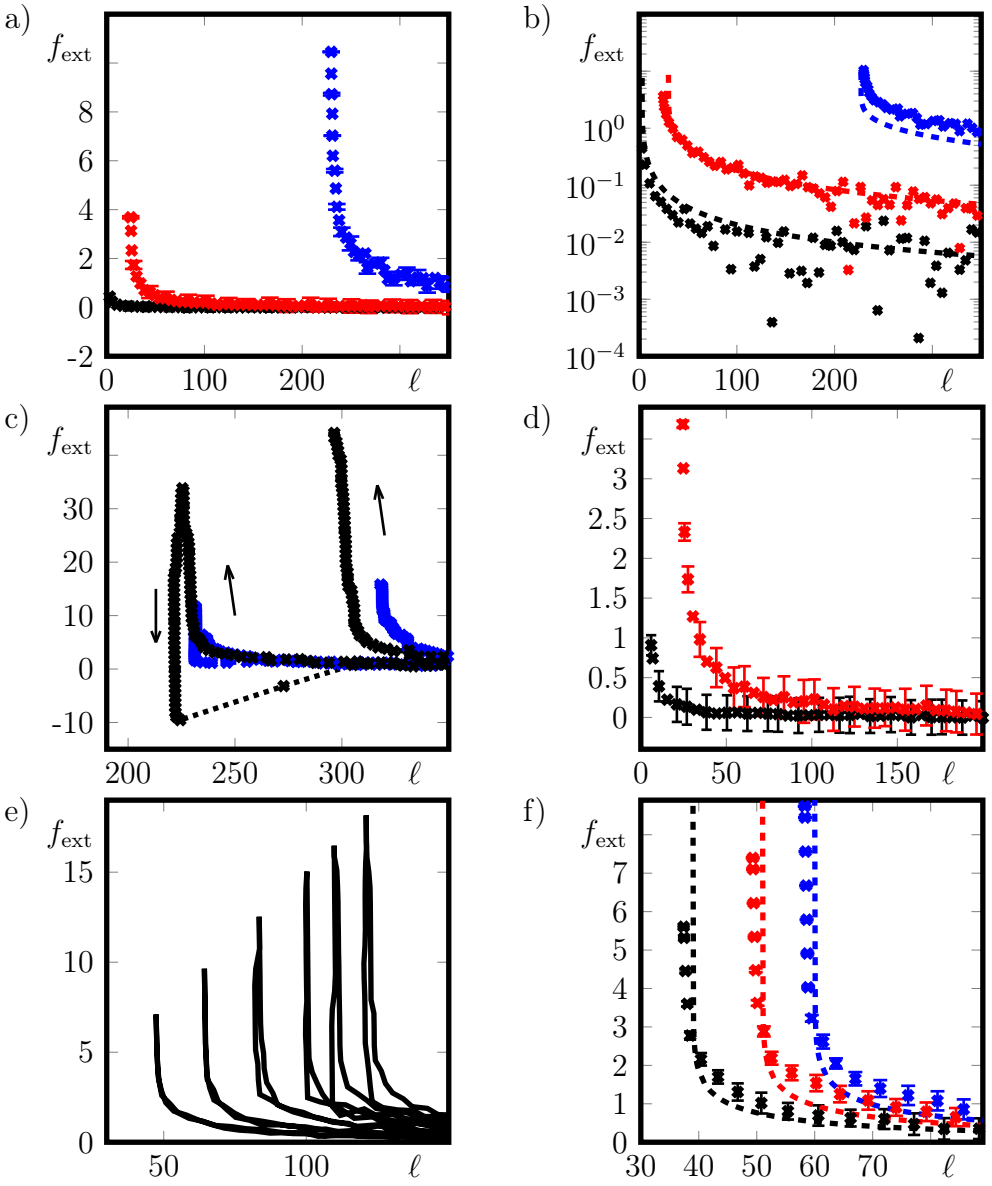

Figure 4.16: **External force for dissociating passive cross-linkers**. (a) Force for $\omega_{\text{p}}^{\text{a}} = 10^{-8}$ (black), 10^{-7} (red) and 10^{-6} (blue). (b) Force for parameters as in (a) together with the entropic force (dashed lines), see Eq. (2.22), for particle numbers $n = 4$ (black), 31 (red) and 228 (blue). (c) Force for $K_{\text{ext}} = 0.05$ (blue) and 0.15 (black). Dotted lines serve as guide to the eye. Arrows indicate directions of sliding. (d) Force for varying filament length $N = 200$ (solid line) and 1000 (dashed line), $\omega_{\text{p}}^{\text{a}} = 10^{-7}$. (e) Force for 25 cycles of reducing and increasing the overlap, every fifth cycle shown. Subsequent cycles correspond to larger maximal forces, $\omega_{\text{p}}^{\text{a}} = 10^{-8}$. (f) Force for varying relaxation time $\tau_0 = 24$ (black), 240 (red) and 2400 (blue), $\omega_{\text{p}}^{\text{a}} = 10^{-6}$. Entropic force (dashed line) for $n = 40$ (black), 52 (red) and 61 (blue). Other parameters are $k_{\text{p}} = 0.18$, $K_{\text{ext}} = 0.15$ (a,b,d-f) and $N = 1000$ (a-c) and 200 (e,f).

forces obtained in simulations are in reasonable agreement with the entropic force for small particle densities, if the number of cross-linkers is fitted, see Fig. 4.16(b). However, the entropic force predicts infinite forces, $f_{\text{ext}} \to \infty$, if the number of available sites in the overlap is less than the number of cross-linkers n, more accurately if $\ell \to n-1$. This is not observed in the simulations. Instead, we see that detachment of cross-linkers and finite stiffness of the cross-linkers prevents infinite forces. The effect is more pronounced for large particle densities, see blue line in Fig. 4.16(b).
Our simulations show an additional phenomenon, which was not observed by Lansky et al. We find that for further cycles of decreasing and increasing the overlap, the measured force changes and hysteresis is observable, see Fig. 4.16(c) The effect is more significant, the larger the occupancy rates of passive particles $\omega_{\text{p}}^{\text{a}}$ and the larger the stiffness of the external spring K_{ext}.
While the overlap is reduced by the external force, the force increases, similar to the situation of fixed number of cross-linkers discussed above. But upon increase of the overlap, the force first reduces while the overlap is not reduced in the same order of magnitude as the external force's rest length. The overlap region is densely packed with cross-linkers and the surrounding filament is also occupied by single-bound passive particles. This is not the case for a fixed number of cross-linkers. Now as the movement of cross-linkers in the overlap is essentially blocked and they cannot invade the non-overlapping region of the filaments at high particle densities, the measured force is reduced by an antagonistic component of blocked cross-linkers just changing their spring extensions while the filaments slide against each other. Since the number n of cross-linkers is large in the overlap region, already small changes $\delta\ell$ of the overlap lead to large changes in the force $k_{\text{p}} n \delta\ell$. This explains the sharp decrease in the force when the overlap is reduced, see Fig. 4.16(c). Above a critical average spring extension of the cross-linkers, cross-links start disbanding and the overlap region is not densely packed anymore. This allows for particle diffusion again and the overlap changes according to the movement of the external force's rest length.
For varying filament length, the force changes its amplitude, but the qualitative behavior remains the same, see Fig. 4.16(d). In order to reduce the computational effort, we can without loss of generality consider a shorter filament, when investigating experiments at longer time scales.
For repeated cycles of decreasing and increasing the overlap, the observed maximal force increases with every cycle, see Fig. 4.16(e). In the coarse of time, more cross-linkers attach to the filament, leading to more force dipole generators. The same holds for the significance of the hysteresis.
If the duration of the experiment is increased, the amplitude of the force as well as the deviation to the entropic force increase, see Fig 4.16(f).

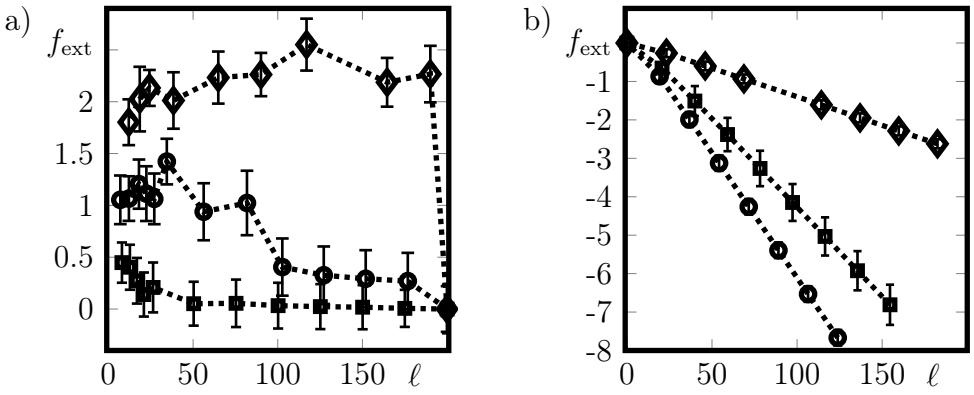

Figure 4.17: **Forces in steady state** for $\tau_0 = 10^6$, $\tau_1 = 10$ and $K_{\text{ext}} = 0.15$. (a) Passive cross-linkers only, $\omega_{\text{p}}^{\text{a}} = 10^{-8}$ (□), 10^{-7} (○) and 10^{-6} (◇). (b) Motors only, $\omega_{\text{m}}^{\text{a}} = 0.01$ (□), 0.1 (○) and 1 (◇). Dashed lines serve as guide to the eye. Other parameters are $k_{\text{p}} = 0.18$, $\mathcal{N} = 10000$, $\tau_1 = 10$ and $N = 200$.

From these measurements, we see that the entropic force suggested by Lansky et al. is able to approximate experiments on short time scales and as long as the density of particles in the overlap is not too high. If particles are densely packed in the overlap region, as it has been shown for a fixed number of cross-linkers as well as for dissociating particles, the entropic force does not reproduce the measured force. For fixed particle numbers, the entropic force is too small, since the assumption of an infinite spring stiffness neglects finite spring extensions and consequently the influence of distribution of extensions on steric interactions and the resulting force. For dissociating particles, the entropic force is not able to capture disbanding of cross-links, decreasing the measured force.
On top of that, if the force was purely entropic, the direction of relative sliding would not affect the measurement. For a reduce in the overlap, we can recover force dependence resembling that of an entropic force. Increase of the overlap however leads to a different force dependence. This hysteresis cannot be described by entropic arguments. Hysteresis effects can be relevant to understand fluctuations of the overlap between microtubules on short time scales and hence influence the characteristics of overlap regulation in a system with molecular motors.

If the waiting time is increased significantly by several orders of magnitude[5] to

[5]To allow for parallelization of these measurements, the rest length of the external force was set once for every data point separately, after full overlap was obtained. Afterwards, the system could relax for a time period τ_0 before the measurement started.

$\tau_0 = 10^6$, a different behavior is observable, see Fig. 4.17(a). For $\omega_\mathrm{p}^\mathrm{a} = 10^{-6}$, the force is almost constant for $0 < \ell < N$, whereas it vanishes for full and negligible overlaps. This is comparable to the force dependence obtained by solving the meanfield equations, see section 4.1 and Fig. 4.7(a).
In the case of smaller attachment rates, $\omega_\mathrm{p}^\mathrm{a} = 10^{-7}$ and 10^{-8}, the force decreases with increasing overlap. As already discovered by Walcott and Sun [152], the force-overlap dependence measured in a system of passive cross-linkers between microtubules in general depends on the drag velocity, at which the filaments are pulled, compared to the typical relaxation time and length scales of the system and is either piecewise constant or linear for small velocities. This is in agreement with the data shown in Fig. 4.17(a). If the experimental time scale is large compared to particle dissociation, which is the case for $\omega_\mathrm{p}^\mathrm{a} = 10^{-6}$, the force is indeed almost constant, similar to the prediction of our meanfield theory for steady state. Deviations from the meanfield steady state profile increase for smaller values of $\omega_\mathrm{p}^\mathrm{a}$, because the relaxation time of the system scales approximately inversely proportional to the smallest rate, which is $\omega_\mathrm{p}^\mathrm{a}$ here.
The error bars in Fig. 4.17(a) are larger than in the case of faster experiments as a consequence of the larger impact of particle fluctuations in a system which is closer to steady state and not governed anymore by the mechanical stresses exerted by cross-linkers' spring extensions.
Simulations for molecular motors only show that the force on the filaments is negative, trying to reduce the overlap and almost proportional to the overlap length, see Fig. 4.17(b). However, there is a small positive force measured for vanishing overlap due to the asymmetry in cross-linking at the filament ends, as already discussed in section 4.1. Same as for passive cross-linkers, this is in line with the predictions of our meanfield theory, see Fig. 4.7(b). Notably, the slope of the force-overlap graph does not necessarily decrease with increasing motor concentration. On the contrary, if the particle concentration is too large, steric interactions between motors lead to a reduced current and consequently a smaller force generated by molecular motors.

As presented in section 2.1, the behavior of a pair of cross-linked filaments can crucially depend on boundary conditions for the cross-linking proteins [151]. Passive cross-linkers always generate a full overlap in presence of a diffusive barrier at the filament ends. If now diffusive cross-linkers are allowed to hop off, the overlap length can fluctuate between full and vanishing overlaps, as can be seen from the steady-state overlap distribution $P(\lambda)$, see Fig. 4.18.
Yet, if passive cross-linkers hopped off the filament ends at the same rate as they hop between sites in the bulk, they would need additional energy to

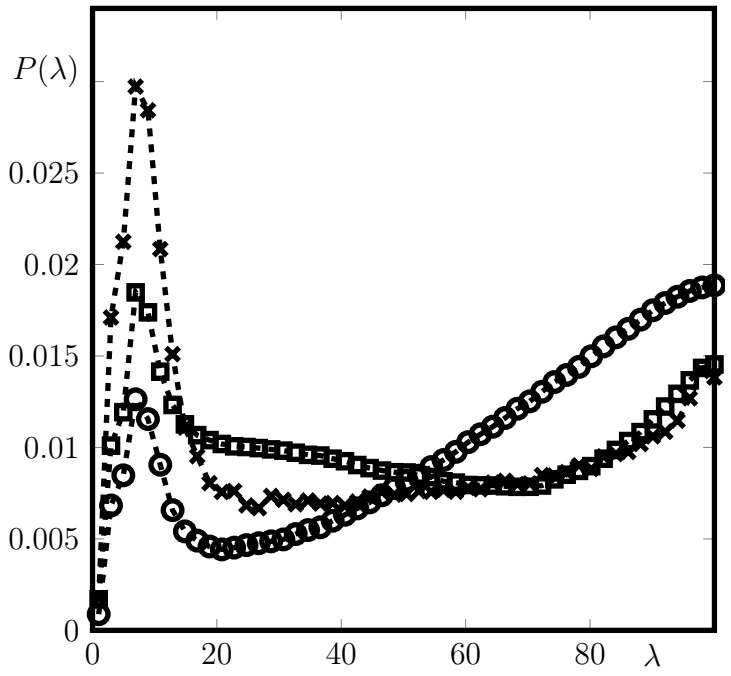

Figure 4.18: **Overlap distribution in absence of a diffusive barrier** for diffusive cross-linkers only, parameters as in table 4.1 and $\omega_{\mathrm{p}}^{\mathrm{a}} = 10^{-6}$ ($\times$), 10^{-5} ($\circ$), 10^{-4} ($\square$). Dashed lines serve as guide to the eye.

switch from a bound to an unbound state. As a consequence, these diffusive particles could not be considered passive anymore.

The observations discussed in this section support our meanfield theory, introduced in section 4.1. Our theoretical description can be compared to experiments [154], see section 2.3 and is in line with previous theories [151, 152], see sections 2.1 and 2.2.

We prove that also with explicitly considering molecular dynamics of motors and passive cross-linkers, finite overlaps between microtubules can be generated and that the force generated by molecular motors scales linear with the overlap length. Based on the observations on forces discussed above, we extend those results towards filament bundles, investigating the collective dynamics of several filaments of different polarization.

4.4 Extending the description to one-dimensional bundles of filaments

So far, we have only considered a single pair of filaments. Since we intend to provide a better understanding of spindle formation, we use the results of the previous sections to introduce a coarse-grained description for the behavior of a bundle of several parallel and antiparallel microtubules interacting via molecular motors and passive cross-linkers.

To start, we consider two populations of microtubules with opposite orientation and constant length L in a system of length B. If x_m is the position of a microtubule's minus-end and x_p of its plus-end then, we denote the densities of plus-ends of microtubules as $c^+(x)$, if $x_\mathrm{m} < x_\mathrm{p}$ and $c^-(x)$, if $x_\mathrm{m} > x_\mathrm{p}$. The densities evolve according to

$$\partial_t c^+(x) = D\partial_x^2 c^+(x) - \partial_x \left(J^{++}(x) + J^{+-}(x) \right) \tag{4.35}$$

and

$$\partial_t c^-(x) = D\partial_x^2 c^-(x) - \partial_x \left(J^{--}(x) + J^{-+}(x) \right) \ . \tag{4.36}$$

The total filament densities $C^\pm(x)$ are given by

$$C^\pm(x) = \int_0^L c^\pm(x \mp \xi)\ d\xi \ . \tag{4.37}$$

In Eqs. (4.35) and (4.36), D is the diffusion constant accounting for spatial fluctuations of the filaments, caused by thermal fluctuations and the stochasticity of the underlying microscopic processes. The terms J^{++}, J^{+-}, J^{--} and J^{-+} describe the currents induced by passive cross-linkers and motors, leading to a relative displacement of the filaments. They are calculated according to

$$J^{++}(x) = c^+(x) \int_{-L}^{L} f_\mathrm{p}(\xi) c^+(x+\xi)\ d\xi \ , \tag{4.38}$$

$$J^{--}(x) = c^-(x) \int_{-L}^{L} f_\mathrm{p}(\xi) c^-(x+\xi)\ d\xi \ , \tag{4.39}$$

$$J^{+-}(x) = -c^+(x) \int_{0}^{2L} \left(f_\mathrm{p}(\xi - L) + f_\mathrm{a}(\xi - L) \right) c^-(x-\xi)\ d\xi \ , \tag{4.40}$$

and

$$J^{-+}(x) = c^{-}(x) \int_0^{2L} \left(f_{\mathrm{p}}(\xi - L) + f_{\mathrm{a}}(\xi - L)\right) c^{+}(x + \xi)\, d\xi \ . \tag{4.41}$$

The dependences of f_{p} and f_{a} on the oriented filament displacement ξ are motivated by the results of the meanfield theory, see 4.1 that is supported by our investigation of forces in section 4.3.
Antiparallel pairs of filaments feel a force that tries to increase the overlap between the filaments caused by the asymmetry of cross-linker configurations at the filament ends, see Fig. 4.6(b). This force is independent of the overlap length, see Fig. 4.7(a), hence the interaction is given by

$$f_{\mathrm{p}}(\xi) = \alpha \operatorname{sign}(\xi) \ , \tag{4.42}$$

with the phenomenological parameter α describing the amplitude of the effective contractile stress. For antiparallel filaments, there is an additional contribution due to the sliding of motors. The force generated by motors is approximately proportional to the overlap length, see Fig. 4.7(b). Consequently, the force

$$f_{\mathrm{a}}(\xi) = \beta |L - \xi| \tag{4.43}$$

is maximized if the overlap is maximized and scales linearly with the overlap length. The parameter β accounts for the strength of the sliding stress.
Parallel filaments are always driven towards full overlap, see Fig. 4.14. For this reason, we assume that only the passive contribution f_{p} to the force has an effect on the overlap between parallel filaments.

We consider both reflective boundary conditions — corresponding to a closed reaction channel in which the bundle interaction takes place — as well as periodic boundary conditions — resembling a circular reaction channel. The reflective boundary conditions are defined via

$$c^{+}(x) = 0 \qquad \forall x > B - L \ , \tag{4.44}$$

$$J^{+}(B - L) = J^{+}(0) = 0 \ , \tag{4.45}$$

$$c^{-}(x) = 0 \qquad \forall x < L \tag{4.46}$$

and

$$J^{-}(L) = J^{-}(B) = 0 \ , \tag{4.47}$$

where

$$J^{\pm}(x) = -\partial_x c^{\pm}(x) + J^{\pm\pm}(x) + J^{\pm\mp}(x) \tag{4.48}$$

is the total filament current including diffusive currents. These conditions represent the geometric constrictions of allowed positions of filament plus-ends.
For periodic boundary conditions, it is sufficient to define

$$c^{\pm}(x \pm B) = c^{\pm}(x) \ . \tag{4.49}$$

We scale length by the box size B and time by B^2/D. Densities transform as $\tilde{c}^{\pm}(\tilde{x}) = Bc^{\pm}(x)$ and parameters as $\tilde{L} = L/B$, $\tilde{\alpha} = B^2\alpha/D$ and $\tilde{\beta} = B^3\beta/D$. To keep notation simple, we only refer to rescaled quantities in the rest of the text and neglect tildes. The full dimensionless equations are given in appendix B.
The partial integro-differential equations (4.35) and (4.36) are solved using a standard forward Euler scheme together with an adaptive step size control and compared to the linear stability analysis for periodic boundary conditions.

We first consider the case of periodic boundary conditions. Here, any constant solution $c^{\pm}(x) \equiv c_0^{\pm}$ is a steady state of Eqs. (4.35) and (4.36). A linear stability analysis[6] is performed by considering small perturbations $\delta^{\pm}(x)$ of the constant solution. These perturbations are Fourier decomposed as

$$\delta^{\pm}(x) = \sum_{n=1}^{\infty} \left(a_n^{\pm}(t)\cos(k_n x) + b_n^{\pm}(t)\sin(k_n x) \right) \ . \tag{4.50}$$

Note that $a_0^{\pm}$ vanishes, because $\delta^{\pm}$ is by definition a small perturbation with vanishing mean value. Inserting this *ansatz* into Eqs. (4.35) and (4.36) enables us to extract a system of four linear differential equations, which can be rewritten as

$$\frac{\mathrm{d}}{\mathrm{d}t} \begin{pmatrix} a_n^+ \\ b_n^+ \\ a_n^- \\ b_n^- \end{pmatrix} = \mathrm{M} \begin{pmatrix} a_n^+ \\ b_n^+ \\ a_n^- \\ b_n^- \end{pmatrix} \ , \tag{4.51}$$

with $\mathrm{M} \in \mathbb{R}^{4\times 4}$. The constant steady state solution $c^{\pm}(x) \equiv c_0^{\pm}$ is unstable, if the largest real part of the Eigenvalues of M is positive. The exact solution of these Eigenvalues is cumbersome and hence not given here explicitly.

[6] The complete calculations for the linear stability analysis can be found in appendix B. In the main text, only the most important ideas together with the results are presented.

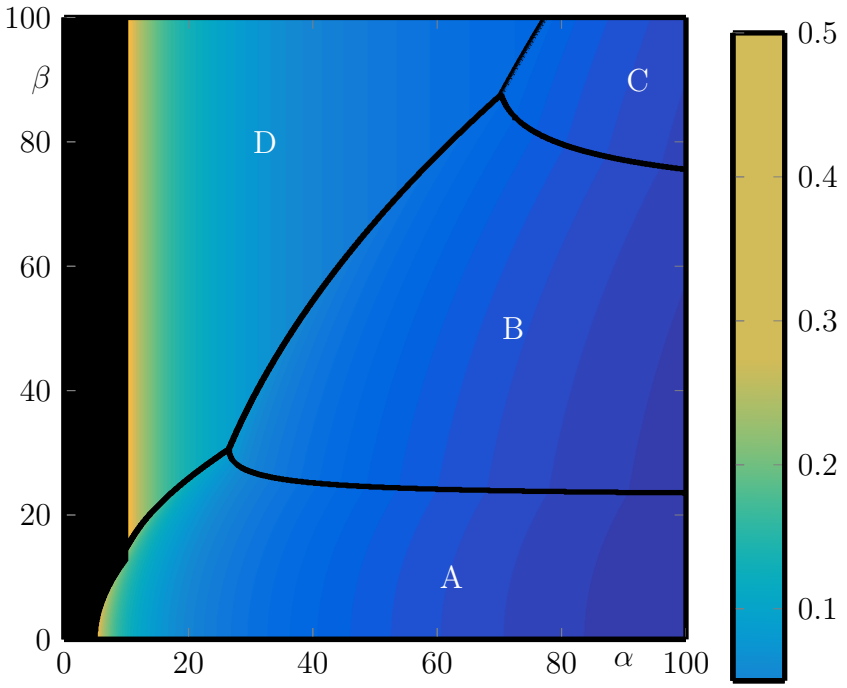

Figure 4.19: **Phase diagram** of a one dimensional bundle from linear stability analysis. Colors indicate the critical length L_c, above which the constant steady state is unstable. For the black regions, no critical length exists. Lines separate regions with different first critical mode $n = 1$ (A), 2 (B) and 3 (C). For D, $n = 1$ and the largest Eigenvalue larger than zero has a non-vanishing complex part.

The phase diagram 4.19, which is obtained by analyzing the Eigenvalues of M, shows that a critical length L_c, above which the system is unstable for given α and β does not exist for all values of α and β. Additionally, the first critical mode in this system is not necessarily the one with $n = 1$, in contrary to previous descriptions of filament bundles [185]. Instead, the smallest value of n, for which the perturbation is unstable, can have larger values. For periodic boundary conditions the numerical solution of Eqs. (4.35) and (4.36) shows that in steady state only a single peak is stable for each c^+ and c^-, see Fig. 4.20(a). This corresponds to filaments of opposite polarization having a finite overlap, thereby generating a bipolar structure. The distance d between the positions of maxima of c^+ and c^- is limited by the length L, see Fig. 4.20(b) and increases with decreasing β.

The results in the case of reflective boundary conditions qualitatively differ from the ones obtained with periodic boundaries, see Eqs. (4.44)–(4.47). No

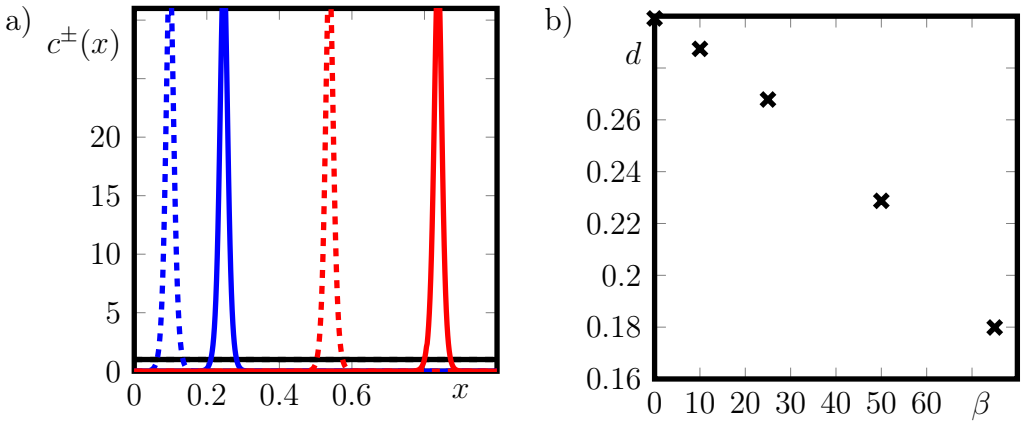

Figure 4.20: **Steady state solutions** of Eqs. (4.35) and (4.36) for periodic boundaries. (a) Steady state densities c^+ (solid line) and c^- (dashed line) for $\alpha = 74$, $c_0^+ = c_0^- = 1$, $\beta = 25$ and $L = 0.05$ (black), 0.15 (blue), 0.3001 (red). (b) Peak distance d between the maxima of c^+ and c^- for $\alpha = 15$, $c_0^+ = c_0^- = 1$ and $L = 0.3001$ for varying values of β.

analytic steady state solution can be given in this case. But still for short filaments, the filament distribution is almost homogeneous, see Fig. 4.21. For larger filaments, bundle formation can be observed. Similar to periodic boundary conditions, reflective boundary conditions also lead to formation of one bipolar filament bundle, see Fig. 4.21. Additionally, the total filament density C is always symmetric to the cell center $x = 1/2$, see Fig. 4.21. If the initial concentrations of filaments of opposite orientation are not equal anymore, the total filament density is still symmetric to the center, see Fig. 4.21(c). This symmetry essentially arises from the symmetry in the equations of time of c^+ and c^- together with the symmetry imposed by the boundary conditions.

The description introduced in this section shows that passive cross-linkers and molecular motors are not only able to generate stable finite overlaps between antiparallel filament. More than that, their action suffices to explain the formation of bipolar bundles. With proper boundary conditions, they are even able to localize the overlap region of antiparallel filaments in the center of a reaction chamber or a cell.

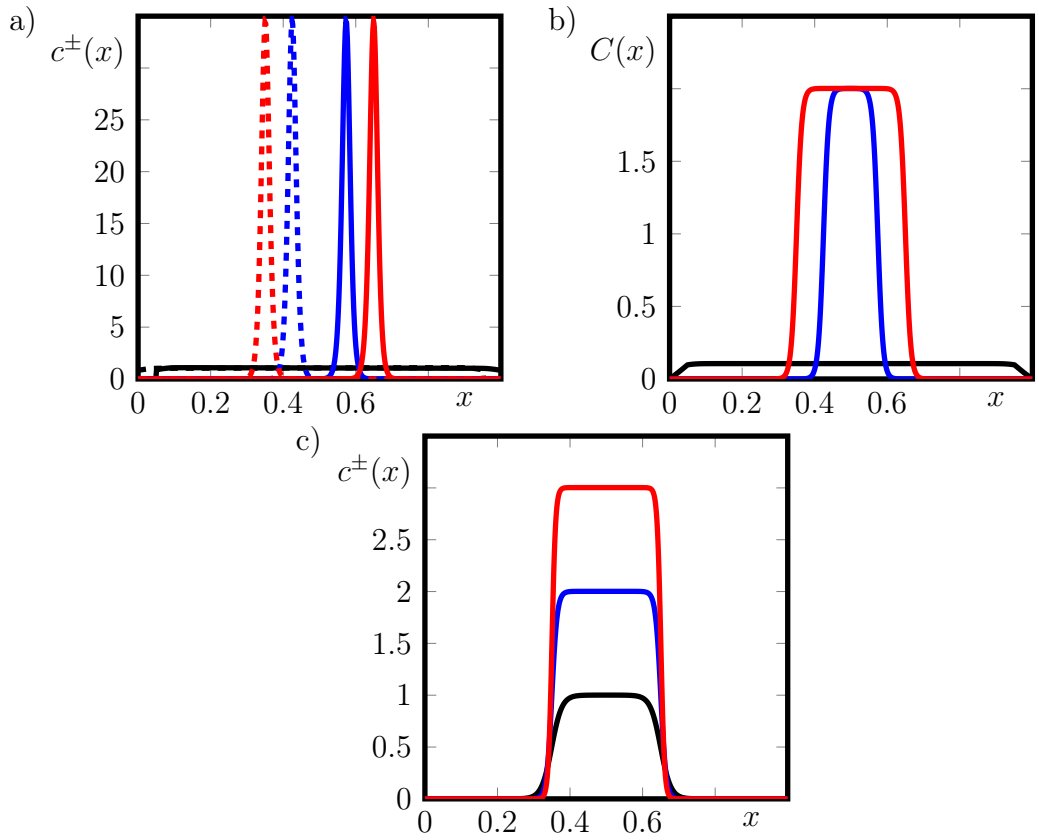

Figure 4.21: **Steady state solutions** of Eqs. (4.35) and (4.36) for reflective boundary conditions. (a) Densities c^+ (solid line) and c^- (dashed line) and (b) total filament density C for $\alpha = 74$, $c_0^+ = c_0^- = 1$, $\beta = 25$ and $L = 0.05$ (black), 0.15 (blue), 0.3001 (red). (c) Total filament density C for $\alpha = 74$, $\beta = 25$, $c_0^+ = 1$ and $c_0^- = 0$ (black), 1 (blue), 2 (red).

4.5 Discussion

In this chapter, we present a stochastic description of diffusive cross-linkers and motor particles, explaining the formation of stable overlaps between antiparallel microtubules. We find that overlaps can be generated in absence of steric interactions between particles of different species, while the size of the overlap can be tuned via the concentration of passive cross-linkers and molecular motors. The results can be reproduced by a meanfield theory.

If particles of different species interact sterically, motors can induce a drift of passive cross-linkers that enables the generation of stable overlaps with and without cross-linking of motors. In absence of passive cross-linkers or in presence of steric interactions, cross-linking motors at high concentrations

can induce fluctuations of the overlap length in the order of the filaments' length.
Stochastic simulations of the model are able to reproduce experiments on passive cross-linkers *in vitro*. A previous study [154] suggests that the force exerted by passive cross-linkers is purely entropic. We show that entropic effects are not sufficient to explain all phenomena observed in a system with passive cross-linkers only. Instead the spring stiffness of the cross-links and hence energetic aspects of the components must be taken into account as well as force-dependent particle dynamics. Our meanfield theory is able to describe the forces measured in the simulations.
Finally, we extend our observations on filament pairs to a one-dimensional theory for bundles of filaments with different orientation. We find that bipolar structures can be generated, with the filaments' polarity similar to that of mitotic spindles. Additionally, the overlap region of the bundles is always centered in space. With this result, our mechanism also helps to understand, how the spindle apparatus can be formed and positioned within cells.

Our theoretical study does not involve the length dynamics of filaments. Possible issues here are for example finding a well-defined steady state. For constant polymerization and depolymerization rates, filaments can either grow infinitely, if the growth rate is larger than the shrinkage rate, or shrink to a vanishing length in the opposite case. In order to fix this problem, future studies could consider the influence of proteins attached to the filaments on the removal and addition of filamentous subunits [62, 63], providing a possibility to regulate the overlap size while maintaining a constant filament length. Especially in the case of microtubule catastrophes, this involves a thorough investigation of what happens to proteins attached to a monomer, when the latter is removed from the filament.
Future *in-vitro* experiments on antiparallel microtubule overlaps should focus on further force measurements on filaments with passive cross-linkers and molecular motors. Reproducing the predictions of the stochastic simulations, especially the dependence of the force on the duration of the experiment as well as the force-overlap function in the case of molecular motors only in experiments would support our current understanding of the system. We are in contact with the labs of Stefan Diez in Dresden and Marcel Janson in Wageningen to perform respective experiments.
Our coarse-grained theory on filament bundles so far is one-dimensional. Since the spindle is a three-dimensional structure, a full understanding of its formation needs a description accounting for the additional degrees of freedom. Here, a first analysis should investigate the behavior of pairs and

triples of microtubules in two and three dimensions, which are tangent to each other and only connected via a small number of cross-linkers. In this situation, also the bending stiffness of microtubules needs to be taken into account.

Chapter 5

Final discussion and Outlook

Summing up the results in this work, we investigate implications of the interactions of different particle species on linear polar filaments, motivated by *in-vitro* experiments on microtubules with molecular motors and passive cross-linkers.

First of all, this study focuses on a single filament, on which motors and passive particles can interact sterically. A passive particle in this context is defined as a diffusive particle moving unbiasedly towards any end of the filament, whereas motors move directionally towards the plus-end.
We find a segregation of the particle species along the filaments. Motor particles hereby accumulate close to the minus-end of the filament, whereas the passive particles are driven in direction of the plus-end. Although the segregation can be maximized depending on the given parameter values, is always present in such a system. Besides interspecies steric interactions, we are able to identify a diffusive barrier for passive particles as a necessary prerequisite for segregation by analyzing the impact of boundary conditions. Experiments on the passive cross-linker Ase1 and the molecular motor Dk4mer provide a possibility to observe the influence of steric interactions *in vitro*.

With our current experimental setup, a reduced velocity of molecular motors as well as accumulation of Ase1 close to filament ends can be clearly identified. This is in qualitative agreement with our theoretical analysis. At high particle densities, necessary to clearly observe segregation on the filament and quantitatively compare theory and experiment, Ase1 forms immobile clusters that do not allow for a phase separation of the different particle types anymore. Additionally, large concentrations of Dk4mer lead to buckling of the

microtubules, caused by mechanical stresses induced by the molecular motor. Upcoming experiments could hence try to identify alternative pairs of sterically interacting proteins.
Future theoretical studies could consider the impact of modeling filaments as a compound of several parallel protofilaments, which is the case for microtubules. This *ansatz* may be relevant to quantitatively match experimental results on the segregation phenomenon with the theoretical description. Apart from that, additional interactions between particles — like cooperative binding, cluster formation or oligomerization — could be taken into account.

The second part of this work explains how molecular motors together with passive cross-linkers are able to generate stable partial overlaps between antiparallel microtubules. This problem is for example relevant *in vivo*, during the formation and maintenance of the mitotic spindle, a vital structure during cell division of eukaryotes.
We introduce a mechanism, that allows for the generation of stable partial overlaps. Without steric interactions between molecular motors and passive cross-linkers, the overlap is always stable. The results from stochastic simulations can be reproduced by a meanfield theory, providing a quantitative understanding of the antagonistic forces that lead to overlap regulation. Passive cross-linkers generate a force that is essentially independent of the overlap length and increases the overlap between the filaments, while motors generate a force proportional to the overlap length sliding the filaments apart.
With interspecies steric interactions, we find a large range of parameters, where again overlap regulation is stable. For these parameters, we can show that stable overlaps can be generated even if motors do not form cross-links. In this case, the motor-induced drift of passive cross-linkers — as analyzed above for a single filament — is sufficient to compensate for the action of cross-linking motors. In addition, with steric interactions there are parameter regimes, for which the overlap length exhibits large fluctuations.
The stochastic model of the underlying molecular processes is able to reproduce experiments *in vitro*. The authors of this study [154] claim that the force generated by passive cross-linkers is a result of steric interactions and purely entropic. We show that additional phenomena exist that cannot be described by entropic principles. Other contributions to the total force, like finite spring-stiffness of cross-linkers or disbanding of cross-links, must be taken into consideration. Our meanfield description, which incorporates molecular dynamics, approximates the forces measured in steady state.
Based on the results of the meanfield theory, we present coarse-grained equa-

tions to capture the behavior of bundles of parallel and antiparallel microtubules. The solution of these equations indicates that molecular motors and passive cross-linkers together with stabilized microtubules provide a molecular machinery, that may be sufficient to create bipolar spindles.

The stochastic model for overlap generation is able to explain *in-vitro* experiments. In addition, we predict a dependence of the force on the time-scales used in the measurements. This has not been checked experimentally so far, but we are in contact with the labs of Stefan Diez in Dresden and Marcel Janson in Wageningen in order to verify our predictions. A positive result would strongly support our current understanding of the molecular details of overlap generation between microtubules. Other than that, filaments are three-dimensional objects, therefore future work could try to include the spatial structure of the filaments. Together with length dynamics and mechanical properties of microtubules in presence of molecular motors and passive cross-linkers, this enables us to understand how a mitotic spindle is formed and maintained.

Appendix A

Gillespie's algorithm

In this appendix, Gillespie's algorithm is sketched. This first passage time Monte Carlo method was first introduced in 1976 by Daniel Gillespie to simulate coupled chemical reactions [186]. However, its principles are also applicable to other systems described via a master equation.

At every time step, two equally distributed random numbers $(\xi_1, \xi_2) \in [0,1) \times [0,1)$ must be generated. Furthermore, N processes p_i with respective rates λ_i, where $1 \leq i \leq N$, are given. With this, the the total transition rate of the system

$$\Omega = \sum_{i=1}^{N} \lambda_i \tag{A.1}$$

can be calculated. The duration τ of the time step is now exponentially distributed with characteristic timescale Ω^{-1} and given by

$$\tau = -\frac{\log(\xi_1)}{\Omega} \ . \tag{A.2}$$

From the definition of λ_i and Ω follows, that the probability of process p_i to happen during the time τ is given by λ_i/Ω. Consequently, process i is performed, if

$$\sum_{k=1}^{i} \lambda_k \leq \Omega\xi_2 < \sum_{k=1}^{i+1} \lambda_k \ . \tag{A.3}$$

These rules are applied in any time step.

In the simulations performed here, the overlap ℓ between the filaments is a continuous quantity changed by a force f. Hence, it also changes its value during a time step, affecting the rates λ_i.
To ensure, that the rates remain approximately constant during the time τ, an additional constraint to the time step length is added by introducing $\Delta_{\max} = \Delta/P$ with the lattice constant Δ, see chapters 3 and 4, and $P \in \mathbb{R}^+$. The relative change in the rates is negligible as long as $f\tau < \Delta_{\max}$. If $f\tau > \Delta_{\max}$, the time is cut off at $\tau = \Delta_{\max}/f$ and continues without any process happening, otherwise a process p_i is chosen as given by Eq. (A.3). For the simulations in chapter 4, we choose $P = 5$.

Appendix B

Linear stability analysis of a one-dimensional bundle of filaments with mixed orientation

In this appendix, we present the linear stability analysis of the dimensionless versions of Eqs. (4.35) and (4.36),

$$\partial_t c^+(x) = \partial_x^2 c^+(x) - \partial_x \left(J^{++}(x) + J^{+-}(x) \right) \ , \tag{B.1}$$

and

$$\partial_t c^-(x) = \partial_x^2 c^-(x) - \partial_x \left(J^{--}(x) + J^{-+}(x) \right) \ . \tag{B.2}$$

The currents are

$$J^{++}(x) = c^+(x) \int_{-L}^{L} f_{\mathrm{p}}(\xi) c^+(x+\xi) \ d\xi \ , \tag{B.3}$$

$$J^{--}(x) = c^-(x) \int_{-L}^{L} f_{\mathrm{p}}(\xi) c^-(x+\xi) \ d\xi \ , \tag{B.4}$$

$$J^{+-}(x) = -c^+(x) \int_{0}^{2L} \left(f_{\mathrm{p}}(\xi - L) + f_{\mathrm{a}}(\xi - L) \right) c^-(x-\xi) \ d\xi \ , \tag{B.5}$$

$$J^{-+}(x) = c^-(x) \int_{0}^{2L} \left(f_{\mathrm{p}}(\xi - L) + f_{\mathrm{a}}(\xi - L) \right) c^+(x+\xi) \ d\xi \ . \tag{B.6}$$

For periodic boundary conditions, any constant distribution $c^{\pm}(x) \equiv c_0^{\pm}$ is a stationary solution of Eqs. (B.1) and (B.2). The time evolution of a perturbation $\delta^{\pm}(x,t)$ is given by

$$\partial_t \delta^{\pm} = \partial_x^2 \delta^{\pm} - \partial_x \left(j^{\pm\pm}(x) + j^{\pm\mp}(x) \right) \ , \tag{B.7}$$

where

$$j^{\pm\pm}(x) = \alpha c_0^{\pm} \left(\int_0^L \delta^{\pm}(x+\xi)\ d\xi - \int_{-L}^0 \delta^{\pm}(x+\xi)\ d\xi \right) \tag{B.8}$$

and

$$\begin{aligned} j^{\pm\mp}(x) = {} & \mp \alpha c_0^{\pm} \left(\int_L^{2L} \delta^{\mp}(x \mp \xi)\ d\xi - \int_0^L \delta^{\mp}(x \mp \xi)\ d\xi \right) \\ & \mp \beta c_0^{\pm} \left(\int_L^{2L} (2L - \xi) \delta^{\mp}(x \mp \xi)\ d\xi + \int_0^L \xi \delta^{\mp}(x \mp \xi)\ d\xi \right) \\ & \mp \beta L c_0^{\mp} \delta^{\pm}(x) \ . \end{aligned} \tag{B.9}$$

If we define $k_n = 2\pi n$ and rewrite[1]

$$\delta^{\pm}(x,t) = \sum_{n=1}^{\infty} \left[a_n^{\pm}(t) \cos(k_n x) + b_n^{\pm}(t) \sin(k_n x) \right] \tag{B.10}$$

in terms of Fourier components, the currents $j^{\pm\pm}$ and $j^{\pm\mp}$ can be expressed up to linear order in $\delta^{\pm}$ as

$$j^{\pm\pm}(x) = 2\alpha c_0^{\pm} \sum_{n=0}^{\infty} \frac{1 - \cos(k_n L)}{k_n} \left(b_n^{\pm} \cos(k_n x) - a_n^{\pm} \sin(k_n x) \right) \ , \tag{B.11}$$

$$\begin{aligned} j^{+-}(x) = \sum_{n=1}^{\infty} \Bigg[& - \beta L c_0^{-} \left(a_n^{+} \cos(k_n x) + b_n^{+} \sin(k_n x) \right) + \frac{c_0^{+}}{k_n^2} \{ \\ & (\beta a_n^{-} - \alpha k_n b_n^{-})(\cos(k_n x)(1 + \cos(2k_n L) - 2\cos(k_n L)) \\ & \quad + \sin(k_n x)(\sin(2k_n L) - 2\sin(k_n L))) \\ & + (\alpha k_n a_n^{-} + \beta b_n^{-})(\cos(k_n x)(2\sin(k_n L) - \sin(2k_n L)) \\ & \quad + \sin(k_n x)(1 + \cos(2k_n L) - 2\cos(k_n L))\} \Bigg] \end{aligned} \tag{B.12}$$

[1] Because $\delta^{\pm}$ is a perturbation with vanishing mean value, by construction already $a^{\pm}(t) = 0$.

and

$$
\begin{aligned}
j^{-+}(x) = \sum_{n=1}^{\infty} \Bigg[& \beta L c_0^+ \left(a_n^- \cos(k_n x) + b_n^- \sin(k_n x) \right) - \frac{c_0^-}{k_n^2} \{ \\
& (\beta a_n^+ + \alpha k_n b_n^+)(\cos(k_n x)(1 + \cos(2k_n L) - 2\cos(k_n L))) \\
& \quad + \sin(k_n x)(2\sin(k_n L) - \sin(2k_n L))) \\
& + (\beta b_n^+ - \alpha k_n a_n^+)(\cos(k_n x)(\sin(2k_n L) - 2\sin(k_n L)) \\
& \quad + \sin(k_n x)(1 + \cos(2k_n L) - 2\cos(k_n L))) \} \Bigg] . \qquad \text{(B.13)}
\end{aligned}
$$

Inserting Eqs. (B.11)–(B.13) into Eq. (B.7) allows to write down the differential equations governing the evolution of $a_n^{\pm}$ and $b_n^{\pm}$

$$
\begin{aligned}
\partial_t a_n^+ = & -k_n^2 a_n^+ + 2\alpha c_0^+ \left(1 - \cos(k_n L)\right) a_n^+ + \beta L c_0^- k_n b_n^+ \\
& - \frac{c_0^+}{k_n} \left[(\sin(2k_n L) - 2\sin(k_n L)) \left(\beta a_n^- - \alpha k_n b_n^- \right) \right. \\
& \left. + \left(1 + \cos(2k_n L) - 2\cos(k_n L)\right) \left(\alpha k_n a_n^- + \beta b_n^- \right) \right] , \qquad \text{(B.14)} \\
\partial_t b_n^+ = & -k_n^2 b_n^+ + 2\alpha c_0^+ \left(1 - \cos(k_n L)\right) b_n^+ - \beta L c_0^- k_n a_n^+ \\
& + \frac{c_0^+}{k_n} \left[(1 + \cos(2k_n L) - 2\cos(k_n L)) \left(\beta a_n^- - \alpha k_n b_n^- \right) \right. \\
& \left. + \left(2\sin(k_n L) - \sin(2k_n L)\right) \left(\alpha k_n a_n^- + \beta b_n^- \right) \right] , \qquad \text{(B.15)} \\
\partial_t a_n^- = & -k_n^2 a_n^- + 2\alpha c_0^- \left(1 - \cos(k_n L)\right) a_n^- - \beta L c_0^+ k_n b_n^- \\
& + \frac{c_0^-}{k_n} \left[(2\sin(k_n L) - \sin(2k_n L)) \left(\beta a_n^+ + \alpha k_n b_n^+ \right) \right. \\
& \left. + \left(1 + \cos(2k_n L) - 2\cos(k_n L)\right) \left(\beta b_n^+ - \alpha k_n a_n^+ \right) \right] \qquad \text{(B.16)}
\end{aligned}
$$

and

$$
\begin{aligned}
\partial_t b_n^- = & -k_n^2 b_n^- + 2\alpha c_0^- \left(1 - \cos(k_n L)\right) b_n^- + \beta L c_0^+ k_n a_n^- \\
& - \frac{c_0^-}{k_n} \left[(1 + \cos(2k_n L) - 2\cos(k_n L)) \left(\beta a_n^+ + \alpha k_n b_n^+ \right) \right. \\
& \left. + \left(\sin(2k_n L) - 2\sin(k_n L)\right) \left(\beta b_n^+ - \alpha k_n a_n^+ \right) \right] . \qquad \text{(B.17)}
\end{aligned}
$$

This system of ordinary linear differential equations can be written in the form

$$
\partial_t \mathbf{Y} = \mathrm{M} \mathbf{Y} \qquad \text{(B.18)}
$$

with $\mathbf{Y} = (a_n^+, b_n^+, a_n^-, b_n^-)^{\mathrm{T}}$ and $M \in \mathbb{R}^{4\times 4}$. The Eigenvalues of M can be calculated numerically and the system's stability can be inferred from the one

with the largest real part. If it is positive, the perturbation initially grows and the constant steady state solution is instable, otherwise the perturbation will decrease again and the constant steady state is stable.

Bibliography

[1] Denis Johann, Debajit Goswami, and Karsten Kruse. Segregation of diffusible and directionally moving particles on a polar filament. *Physical Review E*, 89:042713, 2014.

[2] Denis Johann, Debajit Goswami, and Karsten Kruse. Generation of stable overlaps between antiparallel filaments. *Physical Review Letters*, 115(11):118103, 2015.

[3] Bruce Alberts, Dennis Bray, Karen Hopkin, Alexander Johnson, Julian Lewis, Martin Raff, Keith Ronerts, and Peter Walter. *Essential Cell Biology*. 0-8153-3481-8. Garland Science, New York, 2nd edition, 2004.

[4] Michael Madigan and John Martinko. *Biology of Microorganisms*. 0-13-196893-9. Pearson Education, Old Tapan, 11th edition, 2006.

[5] Bruce Alberts, Alexander Johnson, Peter Walter, Julian Lewis, Martin Raff, Keith Roberts, and Nigel Orme. *Molecular Biology of the Cell* . 978-0815341062. Taylor & Francis Ltd., 5th revised edition, 2007.

[6] Marina Chicurel, Christopher Chen, and Donald Ingber. Cellular control lies in the balance of forces. *Current Opinion in Cell Biology*, 10(2):232–239, 1998.

[7] Sharyn Endow. Microtubule motors in spindle and chromosome motility. *European Journal of Biochemistry*, 262:12–18, 1999.

[8] Berhard Hinner, Markus Tempel, Erich Sackmann, Klaus Kroy, and Erwin Frey. Entanglement, elasticity, and viscous relaxation of actin solutions. *Physical Review Letters*, 81:2614–2617, 1998.

[9] Alexander Zumdieck, Karsten Kruse, Henrik Bringmann, Anthony Hyman, and Frank Jülicher. Stress Generation and Filament Turnover during Actin Ring Constriction. *PLoS ONE*, 2:696, 2007.

[10] Song Li, Jun-Lin Guan, and Shu Chien. Biochemistry and biomechanics of cell motility. *Annual Review of Biomedical Engineering*, 7:105–150, 2005.

[11] Paul Janmey, Joyce Peetermans, Ken Zaner, Thomas Stossel, and Toyoichi Tanaka. Structure and mobility of actin filaments as measured by quasielastic light scattering, viscometry, and electron microscopy. *The Journal of biological chemistry*, 261(18):8357–8362, 1986.

[12] Jingyuan Xu, William Schwarz, Josef Käs, Thomas Stossel, Paul Janmey, and Thomas Pollard. Mechanical Properties of Actin Filament Networks Depend on Preparation, Polymerization Conditions, and Storage of Actin Monomers. *Biophysical Journal*, 74:2731–2740, 1998.

[13] Werner Franke, Erika Schmid, Stefanie Winter, Mary Osborn, and Klaus Weber. Widespread occurrence of intermediate-sized filaments of the vimentin-type in cultured cells from diverse vertebrates. *Experimental Cell Research*, 123(1):25–46, 1979.

[14] Doris Dahl, David Rueger, Amico Bignami, Klaus Weber, and Mary Osborn. Vimentin, the 57 000 molecular weight protein of fibroblast filaments, is the major cytoskeletal component in immature glia. *European Journal of Cell Biology*, 24(2):191–196, 1981.

[15] Christopher Chen and Donald Ingber. Tensegrity and mechanoregulation: from skeleton to cytoskeleton. *Osteoarthritis and Cartilage*, 7(1):81–94, 1999.

[16] Brian Helfand, Lynne Chang, and Robert Goldman. The dynamic and motile properties of intermediate filaments. *Annual Review of Cell and Developmental Biology*, 19:445–647, 2003.

[17] Fern Tablin and David Taube. Platelet intermediate filaments: detection of a vimentinlike protein in human and bovine platelets. *Cell Motility and the Cytoskeleton*, 8(1):61–67, 1987.

[18] Sergei Strelkov, Harald Herrmann, and Ueli Aebi. Molecular architecture of intermediate filaments. *Bioessays*, 25(3):243–251, 2003.

[19] Anastasia Chernyatina, Dmytro Guzenko, and Sergei Strelkov. Intermediate filament structure: the bottom-up approach. *Current Opinion in Cell Biology*, 32C:65–72, 2015.

[20] Harald Herrmann, Harald Bär, Laurent Kreplak, Sergei Strelkov, and Ueli Aebi. Intermediate filaments: from cell architecture to nanomechanics. *Nature Reviews Molecular Cell Biology*, 8(7):562–573, 2007.

[21] Harald Herrmann, Markus Häner, Monika Brettel, Shirley Müller, Kenneth Goldie, Bettina Fedtke, Ariel Lustig, Werner Franke, and Ueli Aebi. Structure and assembly properties of the intermediate filament protein vimentin: the role of its head, rod and tail domains. *Journal of Molecular Biology*, 264(5):933–53, 1996.

[22] Sarah Köster, David Weitz, Robert Goldman, Ueli Aebi, and Harald Herrmann. Intermediate filament mechanics in vitro and in the cell: from coiled coils to filaments, fibers and networks. *Current Opinion in Cell Biology*, 32C:82–91, 2015.

[23] Kenneth Holmes, David Popp, Werner Gebhard, and Wolfgang Kabsch. Atomic model of the actin filament. *Nature*, 347(6288):44–49, 1990.

[24] Albrecht Ott, Marcelo Magnasco, Adam Simon, and Albert Libchaber. Measurement of the persistence length of polymerized actin using fluorescence microscopy. *Physical Review E*, 48:1642, 1993.

[25] Timothy Mitchison and Louise Cramer. Actin-Based Cell Motility and Cell Locomotion. *Cell*, 84(3):371, 1996.

[26] Thomas Pollard and Gary Borisy. Cellular motility driven by assembly and disassembly of actin filaments. *Cell*, 113:549–549, 2003.

[27] Lewis Tilney and David DeRosier. Actin filaments, stereocilia, and hair cells of the bird cochlea. *Developmental Biology*, 116(1):119, 1986.

[28] Nir Gov. Dynamics and Morphology of Microvilli Driven by Actin Polymerization. *Physical Review Letters, vol. 97, Issue 1, id. 018101*, 97:018101, jul 2006.

[29] Guillaume Salbreux, Guillaume Charras, and Ewa Paluch. Actin cortex mechanics and cellular morphogenesis. *Trends Cell Biology*, 22(10):536–545, 2012.

[30] Frederick Gittes, Brian Mickey, Jilda Nettleton, and Jonathon Howard. Flexural rigidity of microtubules and actin filaments measured from thermal fluctuations in shape. *The Journal of Cell Biology*, 120(4):923, 1993.

[31] Laurent Gauthier, Bénédicte Charrin, Maria Borrell-Pagès, Jim P Dompierre, Hélène Rangone, Fabrice P Cordelières, Jan De Mey, Marcy MacDonald, Volkmar Lessmann, Sandrine Humbert, and Frédéric Saudou. Huntingtin controls neurotrophic support and survival of neurons by enhancing BDNF vesicular transport along microtubules. *Cell*, 118(1):127–138, 2004.

[32] Michael Welte. Bidirectional transport along microtubules. *Current Biology*, 14(13):R525–537, 2004.

[33] Christoph Erlenkaemper and Karsten Kruse. Uncorrelated changes of subunit stability can generate length-dependent disassembly of treadmilling filaments. *Physical Biology*, 6:046016, 2009.

[34] David Begg, Richard Rodewald, and Lionel Rebhun. The visualization of actin filament polarity in thin sections. Evidence for the uniform polarity of membrane-associated filaments. *The Journal of Cell Biology*, 79(3):846, 1978.

[35] Thomas Pollard. Rate Constants for the Reactions of ATP- and ADP-Actin with the Ends of Actin Filaments. *The Journal of Cell Biology*, 103:2747–2754, 1986.

[36] Christoph Erlenkämper and Karsten Kruse. Treadmilling and length distributions of active polar filaments. *Journal of Chemical Physics*, 139:4907, 2013.

[37] Hugo Bowne-Anderson, Marija Zanic, Monika Kauer, and Jonathon Howard. Microtubule dynamic instability: a new model with coupled GTP hydrolysis and multistep catastrophe. *Bioessays*, 35(5):452–461, 2013.

[38] Kenneth Sawin, Katherine Leguellec, Michel Philippe, and Timothy Mitchison. Mitotic spindle organization by a plus-end-directed microtubule motor. *Nature*, 359:540–543, 1992.

[39] Torsten Wittmann, Anthony Hyman, and Arshad Desai. The spindle: a dynamic assembly of microtubules and motors. *Nature Cell Biology*, 3:E28–E34, 2001.

[40] Marc Edwards, Adam Zwolak, Dorothy Schafer, David Sept, Roberto Dominguez, and John Cooper. Capping protein regulators fine-tune actin assembly dynamics. *Nature Reviews Molecular Cell Biology*, 15(10):677–689, 2014.

[41] Laurent Blanchoin, Rajaa Boujemaa-Paterski, Cécile Sykes, and Julie Plastino. Actin dynamics, architecture, and mechanics in cell motility. *Physiological Reviews*, 94(1):235–263, 2014.

[42] Thomas Pujol, Olivia du Roure, Marc Fermigier, and Julien Heuvingh. Impact of branching on the elasticity of actin networks. *Proceedings of the National Academy of Sciences*, 109:10364–10369, 2012.

[43] Mark J. Dayel and R. Dyche Mullins. Activation of Arp2/3 complex: addition of the first subunit of the new filament by a WASP protein triggers rapid ATP hydrolysis on Arp2. *PLoS Biol.*, 2(4):E91, 2004.

[44] Coumaran Egile, Isabelle Rouiller, Xiao-Ping Xu, Niels Volkmann, Rong Li, and Dorit Hanein. Mechanism of filament nucleation and branch stability revealed by the structure of the Arp2/3 complex at actin branch junctions. *PLoS Biology*, 3(11):e383, 2005.

[45] Dean Astumian. Thermodynamics and Kinetics of Molecular Motors. *Biophysical Journal*, 98:2401–2409, 2010.

[46] Geoffrey Cooper. *The Cell: A Molecular Approach.* 0-87893-106-6. Sinauer Associates, Sunderland, 2nd edition, 2000.

[47] Hiroshi Tokuo and Mitsuo Ikebe. Myosin X transports Mena/VASP to the tip of filopodia. *Biochemical and Biophysical Research Communications*, 319(1):214–220, 2004.

[48] Mirco Castoldi and Isabelle Vernos. Chromokinesin Xklp1 contributes to the regulation of microtubule density and organization during spindle assembly. *Molecular Biology Of The Cell*, 17:1451–1460, 2006.

[49] Austin Hepperla, Patrick Willey, Courtney Coombes, Breanna Schuster, Maryam Gerami-Nejad, Mark McClellan, Soumya Mukherjee, Janet Fox, Mark Winey, David Odde, Eileen O'Toole, and Melissa Gardner. Minus-end-directed Kinesin-14 motors align antiparallel microtubules to control metaphase spindle length. *Developmental Cell*, 31(1):61–72, 2014.

[50] Mary Porter and Winfield Sale. The 9 + 2 Axoneme Anchors Multiple Inner Arm Dyneins and a Network of Kinases and Phosphatases that Control Motility. *The Journal of Cell Biology*, 151(5):F37–42, 2000.

[51] Harvey Lodish, Arnold Berk, Chris Kaiser, Monty Krieger, Matthew Scott, Anthony Bretscher, Hidde Ploegh, and Paul Matsudaira. *Molecular Cell Biology*. 0716776014. W. H. Freeman and Company, New York, 6th edition, 2007.

[52] Jedidiah Gaetz and Tarun Kapoor. Dynein/dynactin regulate metaphase spindle length by targeting depolymerizing activities to spindle poles. *The Journal of Cell Biology*, 166(4):465–471, 2004.

[53] Yoshihisa Kurasawa, William Earnshaw, Yuko Mochizuki, Naoshi Dohmae, and Kazuo Todokoro. Essential roles of KIF4 and its binding partner PRC1 in organized central spindle midzone formation. *Embo Journal*, 23:3237–3248, 2004.

[54] Jesse Gatlin and Kerry Bloom. Microtubule motors in eukaryotic spindle assembly and maintenance. *Semininars in Cell and Developmental Biology*, 21(3):248–254, 2010.

[55] Linda Wordeman. How kinesin motor proteins drive mitotic spindle function: Lessons from molecular assays. *Seminars in Cell and Developmental Biology*, 21(3):260–268, 2010.

[56] Zachary Olmsted, Andrew Colliver, Timothy Riehlman, and Janet Paluh. Kinesin-14 and kinesin-5 antagonistically regulate microtubule nucleation by gamma-TuRC in yeast and human cells. *Nature Communications*, 5:5339, 2014.

[57] Sharyn Endow, Sang Kang, Lisa Sattwerwhite, Mark Rose, Victoria Skeen, and Edward Salmon. Yeast Kar3 Is A Minus-End Microtubule Motor Protein That Destabilizes Microtubules Preferentially At The Minus Ends. *Embo Journal*, 13:2708–2713, 1994.

[58] Claire Walczak. The Kin I kinesins are microtubule end-stimulated ATPases. *Molecular Cell*, 11(2):286–288, 2003.

[59] Ayana Moore and Linda Wordeman. The mechanism, function and regulation of depolymerizing kinesins during mitosis. *Trends in Cell Biology*, 14(10):537–546, 2004.

[60] Vladimir Varga, Jonne Helenius, Kozo Tanaka, Anthony A Hyman, Tomoyuki U Tanaka, and Jonathon Howard. Yeast kinesin-8 depolymerizes microtubules in a length-dependent manner. *Nature Cell Biology*, 8(9):957–962, 2006.

[61] Vladimir Varga, Cecile Leduc, Volker Bormuth, Stefan Diez, and Jonathon Howard. Kinesin-8 motors act cooperatively to mediate length-dependent microtubule depolymerization. *Cell*, 138(6):1174–1183, 2009.

[62] Denis Johann, Christoph Erlenkämper, and Karsten Kruse. Length Regulation of Active Biopolymers by Molecular Motors. *Physical Review Letters*, 108:258103, 2012.

[63] Anna Melbinger, Louis Reese, and Erwin Frey. Microtubule Length Regulation by Molecular Motors. *Physical Review Letters*, 108:258104, 2012.

[64] Christoph Erlenkämper, Denis Johann, and Karsten Kruse. Impact of motor molecules on the dynamics of treadmilling filaments. *Physical Review E*, 86:051906, 2012.

[65] Jingyuan Xu, James Casella, and Thomas Pollard. Effect of capping protein, CapZ, on the length of actin filaments and mechanical properties of actin filament networks. *Cell Motility And The Cytoskeleton*, 42:73–81, 1999.

[66] Ronald Vale. The Molecular Motor Toolbox for Intracellular Transport. *Cell*, 112(4):467, 2003.

[67] Jonathan Howard. *Mechanics of Motor Proteins and the Cytoskeleton*. 978-0-87893-333-4. Sinauer Associates, Inc., Sunderland, First edition, 2001.

[68] Anatoly Kolomeisky and Michael Fisher. Molecular Motors: A Theorist's Perspective. *Annual Review of Physical Chemistry*, 58:675–695, 2007.

[69] Anatoly Kolomeisky and Michael Fisher. A Simple Kinetic Model Describes the Processivity of Myosin-V. *Biophysical Journal*, 84:1642–1650, 2003.

[70] Karel Svoboda, Christoph Schmidt, Bruce Schnapp, and Steven Block. Direct observation of kinesin stepping by optical trapping interferometry. *Science*, 365:721–727, 1993.

[71] William Hancock and Jonathon Howard. Kinesin's processivity results from mechanical and chemical coordination between the ATP hydrolysis cycles of the two motor domains. *Proceedings of the National Academy of Science*, 96(23):13147–13152, 1999.

[72] Koen Visscher, Mark Schnitzer, and Steven Block. Single kinesin molecules studied with a molecular force clamp. *Nature*, 400:184–189, 1999.

[73] Bin Guo and William Guilford. Mechanics of actomyosin bonds in different nucleotide states are tuned to muscle contraction. *Proceedings of the National Academy of Sciences*, 103(26):9844–9849, 2006.

[74] Sabyasachi Rakshit, Yunxiang Zhang, Kristine Manibog, Omer Shafraz, and Sanjeevi Sivasankar. Ideal, catch, and slip bonds in cadherin adhesion. *Proceedings of the National Academy of Sciences*, 109:18815–18820, 2012.

[75] Hendrik Kramers. Brownian Motion in a Field of Force and the Diffusion Model of Chemical Reactions. *Physica*, 7:284–304, 1940.

[76] Peter Hänggi, Peter Talkner, and Michal Borkovec. Reaction-rate theory: fifty years afer Kramers. *Reviews of Modern Physics*, 62:251–342, 1990.

[77] Wendy Thomas, Viola Vogel, and Evgeni Sokurenko. Biophysics of catch bonds. *Annual Review of Biophysycs*, 37:399–416, 2008.

[78] Ahmet Yildiz, Michio Tomishige, Ronald Vale, and Paul Selvin. Kinesin Walks Hand-Over-Hand. *Science*, 303:676–679, 2004.

[79] William Schief and Jonathon Howard. Conformational changes during kinesin motility. *Current Opinion in Cell Biology*, 13(1):19–28, 2001.

[80] Edgar Meyhofer and Jonathon Howard. The Force Generated by a Single Kinesin Molecule Against an Elastic Load. *Proceedings of the National Academy of Sciences*, 92:574–578, 1995.

[81] Masayoshi Nishiyama, Hideo Higuchi, and Toshio Yanagida. Chemomechanical coupling of the forward and backward steps of single kinesin molecules. *Nature Cell Biology*, 4(10):790–797, 2002.

[82] Thomas Guérin, Jacques Prost, and Jean-Francois Joanny. Dynamical behavior of molecular motor assemblies in the rigid and crossbridge models. *European Physical Journal E*, 34(6):1–21, 2011.

[83] Carolyn MacDonald, Julian Gibbs, and Allen Pipkin. Kinetics of biopolymerization on nucleic acid templates. *Biopolymers*, 6(1):1–5, 1968.

[84] Bernard Derrida, Martin Evans, Vincent Hakim, and Vincent Pasquier. Exact solution of a 1D asymmetric exclusion model using a matrix formulation. *Journal of Physics A: Mathematical and General*, 26:1493–1517, 1993.

[85] Joachim Krug. Boundary-induced phase transitions in driven diffusive systems. *Physical Review Letters*, 67:1882–1885, 1991.

[86] Satoshi Yukawa, Macoto Kikuchi, and Shin-Ichi Tadaki. Dynamical Phase-Transition In One-Dimensional Traffic Flow Model With Blockage. *Journal Of The Physical Society Of Japan*, 63:3609–3618, 1994.

[87] Dirk Helbing. Traffic and related self-driven many-particle systems. *Reviews of Modern Physics*, 73:1067–1141, 2001.

[88] Tobias Reichenbach, Erwin Frey, and Thomas Franosch. Traffic jams induced by rare switching events in two-lane transport. *New Journal of Physics*, 9:159, 2007.

[89] Cecile Appert-Rolland, Julien Cividini, and Henk Hilhorst. Intersection of two TASEP traffic lanes with frozen shuffle update. *Journal of Statistical Mechanics: Theory and Experiment*, 10:014, 2011.

[90] Chikashi Arita and Andreas Schadschneider. Exclusive queueing processes and their application to traffic systems. *Mathematical Models and Methods in Applied Sciences*, 25(03):401, 2015.

[91] Martin Evans, Róbert Juhász, and Ludger Santen. Shock formation in an exclusion process with creation and annihilation. *Physical Review E*, 68:026117, 2003.

[92] Andrea Parmeggiani, Thomas Franosch, and Erwin Frey. Phase Coexistence in Driven One-Dimensional Transport. *Physical Review Letters*, 90:086601, 2003.

[93] Róbert Juhász and Ludger Santen. Dynamics of an exclusion process with creation and annihilation. *Journal of Physics A: Mathematical and Theoretical*, 37:3933–3944, 2004.

[94] Andrea Parmeggiani, Thomas Franosch, and Erwin Frey. Totally asymmetric simple exclusion process with Langmuir kinetics. *Physical Review E*, 70:046101, 2004.

[95] Maximilian Ebbinghaus and Ludger Santen. A model for bidirectional traffic of cytoskeletal motors. *Journal of Statistical Mechanics: Theory and Experiment*, 03:030, 2009.

[96] Gernot Klein, Karsten Kruse, Gianaurelio Cuniberti, and Frank Jülicher. Filament Depolymerization by Motor Molecules. *Physical Review Letters*, 94:108102, 2005.

[97] Kate Sugden and Michael Evans. A dynamically extending exclusion process. *Journal of Statistical Mechanics: Theory and Experiment*, 11:13, 2007.

[98] Deborah Wessels, David Soll, David Knecht, William Loomis, Arturo De Lozanne, and James Spudich. Cell motility and chemotaxis in Dictyostelium amebae lacking myosin heavy chain. *Developmental Biology*, 128(1):164, 1988.

[99] Robert Eddy, Lynda Pierini, Fumio Matsumura, and Frederick Maxfield. Ca2+-dependent myosin II activation is required for uropod retraction during neutrophil migration. *Journal of Cell Science*, 113:1287–1298, 2000.

[100] Konstantin Doubrovinski and Karsten Kruse. Self-Organization of Treadmilling Filaments. *Physical Review Letters*, 99:228104, nov 2007.

[101] Falko Ziebert, Sumanth Swaminathan, and Igor Aranson. Model for self-polarization and motility of keratocyte fragments. *Journal of the Royal Society Interface*, 9(70):1084–92, 2012.

[102] Alexander Dreher, Igor Aranson, and Karsten Kruse. Spiral actin-polymerization waves can generate amoeboidal cell crawling. *New Journal of Physics*, 16(5):055007, 2014.

[103] Pirta Hotulainen and Casper Hoogenraad. Actin in dendritic spines: connecting dynamics to function. *The Journal of Cell Biology*, 189(4):619–629, 2010.

[104] Theodor Schwann. *Mikroskopische Untersuchungen über die Übereinstimmung in der Struktur und dem Wachsthum der Thiere und Pflanzen.* Sander, Berlin, First edition, 1839.

[105] Wilhelm von Waldeyer-Hartz. Über Karyokinese und ihre Beziehungen zu den Befruchtungsvorgängen. *Archiv für mikroskopische Anatomie und Entwicklungsgeschichte*, 32:1–122, 1888.

[106] Tim Yen and Bruce Schaart. Kinetochore function: molecular motors, switches and gates. *Current Opinion in Cell Biology*, 8:381–388, 1998.

[107] P. Todd Stukenberg and Daniel J. Burke. Connecting the microtubule attachment status of each kinetochore to cell cycle arrest through the spindle assembly checkpoint. *Chromosoma*, 2015.

[108] Mohan Balasubramanian, Erfei Bi, and Michael Glotzer. Comparative analysis of cytokinesis in budding yeast, fission yeast and animal cells. *Current Biology*, 14(18):R806–818, 2004.

[109] Inês Mendes Pinto, Boris Rubinstein, Andrei Kucharavy, Jay R Unruh, and Rong Li. Actin depolymerization drives actomyosin ring contraction during budding yeast cytokinesis. *Developmental Cell*, 22(6):1247–1260, 2012.

[110] Inês Mendes Pinto, Boris Rubinstein, and Rong Li. Force to Divide: Structural and Mechanical Requirements for Actomyosin Ring Contraction. *Biophysical Journal*, 105:547–554, 2013.

[111] Viktoria Wollrab. *Active gels in vivo : patterns and dynamics in cytokinetic rings and their functions in cell division*. PhD thesis, École doctorale Sciences chimiques, Strasbourg, 2014.

[112] Claire Walczak and Rebecca Heald. *International Review of Cytology*, volume 265 of *978-0-12-374332-9* , chapter 3 – Mechanisms of Mitotic Spindle Assembly and Function, page 111. Elsevier, 2008.

[113] Michael Glotzer. The 3Ms of central spindle assembly: microtubules, motors and MAPs. *Nature Reviews Molecular Cell Biology*, 10(1):9–20, 2009.

[114] Alexey Khodjakov, Richard Cole, Berl Oakley, and Conly Rieder. Centrosome-independent mitotic spindle formation in vertebrates. *Current Biology*, 10(2):59, 2000.

[115] Renata Basto, Joyce Lau, Tatiana Vinogradova, Alejandra Gardiol, C Geoffrey Woods, Alexey Khodjakov, and Jordan W Raff. Flies without centrioles. *Cell*, 125(7):1375–86, 2006.

[116] Amity Manning and Duane Compton. Structural and regulatory roles of nonmotor spindle proteins. *Current Opinion in Cell Biology*, 20(1):101–106, 2008.

[117] Oliver Gruss, Malte Wittmann, Hideki Yokoyama, Rainer Pepperkok, Thomas Kufer, Herman Silljé, Eric Karsenti, Iain W Mattaj, and Isabelle Vernos. Chromosome-induced microtubule assembly mediated by TPX2 is required for spindle formation in HeLa cells. *Nature Cell Biology*, 4(11):871–879, 2002.

[118] Christoph Schatz, Rachel Santarella, Andreas Hoenger, Eric Karsenti, Iain W Mattaj, Oliver Gruss, and Rafael Carazo-Salas. Importin alpha-regulated nucleation of microtubules by TPX2. *The EMBO Journal*, 22(9):2060–2070, 2003.

[119] Roy Wollman, Eric Cytrynbaum, Jonathan Jones, Tobias Meyer, Jonathan Scholey, and Alexander Mogilner. Efficient chromosome capture requires a bias in the 'search-and-capture' process during mitotic-spindle assembly. *Curr. Biol.*, 15(9):828–832, 2005.

[120] Alex Mogilner and Erin Craig. Towards a quantitative understanding of mitotic spindle assembly and mechanics. *Journal of Cell Science*, 123:3435–3445, 2010.

[121] Akira Yamashita, Masamitsu Sato, Akiko Fujita, Masayuki Yamamoto, and Takashi Toda. The roles of fission yeast ase1 in mitotic cell division, meiotic nuclear oscillation, and cytokinesis checkpoint signaling. *Molecular Biology of the Cell*, 16(3):1378–95, 2005.

[122] Tetsuya Horio and Takashi Murata. The role of dynamic instability in microtubule organization. *Frontiers in Plant Science*, 5:511, 2014.

[123] Lukas Kapitein, Marcel Janson, Siet van den Wildenberg, Casper Hoogenraad, Christoph Schmidt, and Erwin Peterman. Microtubule-driven multimerization recruits ase1p onto overlapping microtubules. *Current Biology*, 18(21):1713–1717, 2008.

[124] Heather McDonald, Russell Stewart, and Lawrence Goldstein. The kinesin-like ncd protein of Drosophila is a minus end-directed microtubule motor. *Cell*, 63(6):1159–1165, 1990.

[125] Hernando Sosa, Prabha Dias, Andreas Hoenger, Michael Whittaker, Elizabeth Wilson-Kubalek, Elena Sablin, Robert Fletterick, Ronald Vale, and Ronald Milligan. A Model for the Microtubule-Ncd Motor Protein Complex Obtained by Cryo-Electron Microscopy and Image Analysis. *Cell*, 90:217–224, 1997.

[126] Machiko Hatsumi and Sharyn Endow. The Drosophila ncd microtubule motor protein is spindle-associated in meiotic and mitotic cells. *Journal of Cell Science*, 103:1013–1020, 1992.

[127] Heinrich Matthies, Heather McDonald, Lawrence Goldstein, and William Theurkauf. Anastral meiotic spindle morphogenesis: role of the non-claret disjunctional kinesin-like protein. *Journal of Cell Biology*, 134(2):455–464, 1996.

[128] Lukas Kapitein, Erwin Peterman, Benjamin Kwok, Jeffrey Kim, Tarun Kapoor, and Christoph Schmidt. The bipolar mitotic kinesin Eg5 moves on both microtubules that it crosslinks. *Nature*, 435(7038):114–8, 2005.

[129] Peter Bieling, Ivo Telley, and Thomas Surrey. A minimal midzone protein module controls formation and length of antiparallel microtubule overlaps. *Cell*, 142(3):420–32, 2010.

[130] Tim Mitchison, Louise Evans, Eric Schulze, and Marc Kirschner. Sites of microtubule assembly and disassembly in the mitotic spindle. *Cell*, 45(4):515, 1986.

[131] Timothy Mitchison and Kenneth Sawin. Tubulin flux in the mitotic spindle: where does it come from, where is it going? *Cell Motility and the Cytoskeleton*, 16(2):93–98, 1990.

[132] Daniel Buster, Dong Zhang, and David Sharp. Poleward tubulin flux in spindles: regulation and function in mitotic cells. *Molecular Biology of the Cell*, 18(8):3094–3104, 2007.

[133] Eric Karsenti and Isabelle Vernos. The Mitotic Spindle: A Self-Made Machine. *Science*, 294:543–547, 2001.

[134] David Sharp, Gregory Rogers, and Jonathan Scholey. Microtubule motors in mitosis. *Nature*, 407(6800):41–47, 2000.

[135] Natalie Prigozhina, Richard Walker, C. Elizabeth Oakley, and Berl Oakley. Gamma-tubulin and the C-terminal motor domain kinesin-like protein, KLPA, function in the establishment of spindle bipolarity in Aspergillus nidulans. *Molecular Biology of the Cell*, 12(10):3161–3174, 2001.

[136] Gohta Goshima and Jonathan Scholey. Control of mitotic spindle length. *Annual Review of Cell and Developmental Biology*, 26:21–57, 2010.

[137] Tarun Kapoor and Timothy Mitchison. Eg5 is static in bipolar spindles relative to tubulin: evidence for a static spindle matrix. *Journal of Cell Biology*, 154(6):1125–1133, 2001.

[138] Marcel Janson, Rose Loughlin, Isabelle Loïodice, Chuanhai Fu, Damian Brunner, François Nédélec, and Phong Tran. Crosslinkers and motors organize dynamic microtubules to form stable bipolar arrays in fission yeast. *Cell*, 128(2):357–368, 2007.

[139] Erwin Peterman and Jonathan Scholey. Mitotic microtubule crosslinkers: insights from mechanistic studies. *Current Biology*, 19(23):R1089–1094, 2009.

[140] Alex Mogilner and George Oster. Cell motility driven by actin polymerization. *Biophysical Journal*, 71(6):3030–3045, dec 1996.

[141] Hidetake Miyata, Shuji Nishiyama, Ken-Ichirou Akashi, and Jr. Kinosita, Kazuhiko. Protrusive Growth from Giant Liposomes Driven by Actin Polymerization. *Proceedings of the National Academy of Sciences of the United States of America*, 96:2048–2053, 1999.

[142] Alex Mogilner and George Oster. Force Generation by Actin Polymerization II: The Elastic Ratchet and Tethered Filaments. *Biophysical Journal*, 84:1591–1605, mar 2003.

[143] Aley Mogilner and B Rubinstein. The physics of filopodial protrusion. *Biophysical Journal*, 89:782–795, 2005.

[144] Erdinc Atilgan, Denis Wirtz, and Sean Sun. Mechanics and Dynamics of Actin-Driven Thin Membrane Protrusions. *Biophysical Journal*, 90:65–76, jan 2006.

[145] Hyeran Kang, Qi Wen, Paul Janmey, Jay Tang, Enrico Conti, and Fred MacKintosh. Nonlinear elasticity of stiff filament networks: strain stiffening, negative normal stress, and filament alignment in fibrin gels. *Journal of Physical Chemistry B*, 113(12):3799–3805, 2009.

[146] Wilbur Channels, François Nédélec, Yixian Zheng, and Pablo Iglesias. Spatial Regulation Improves Antiparallel Microtubule Overlap during Mitotic Spindle Assembly. *Biophysical Journal*, 94:2598–2609, 2008.

[147] Rose Loughlin, Rebecca Heald, and François Nédélec. A computational model predicts Xenopus meiotic spindle organization. *Journal of Cell Biology*, 191(7):1239–1249, 2010.

[148] David Zwicker, Markus Decker, Steffen Jaensch, Anthony A. Hyman, and Frank Julicher. Centrosomes are autocatalytic droplets of pericentriolar material organized by centrioles. *Proceedings of the National Academy of Sciences*, 111:E2636–E2645, 2014.

[149] Garrett Greenan, Clifford Brangwynne, Steffen Jaensch, Jöbin Gharakhani, Frank Jülicher, and Anthony Hyman. Centrosome size sets mitotic spindle length in Caenorhabditis elegans embryos. *Current Biology*, 20(4):353–358, 2010.

[150] Gijsje Koenderink, Zvonimir Dogic, Fumihiko Nakamura, Poul Bendix, Frederick Mackintosh, John Hartwig, Thomas Stossel, and David Weitz. Special Feature: Liquids and Structural Glasses Special Feature: An active biopolymer network controlled by molecular motors. *Proceedings of the National Academy of Sciences*, 106:15192–15197, 2009.

[151] Karsten Kruse and Ken Sekimoto. Growth of fingerlike protrusions driven by molecular motors. *Physical Review E*, 66:031904, 2002.

[152] Sam Walcott and Sean Sun. Active force generation in cross-linked filament bundles without motor proteins. *Physical Review E*, 82:050901, 2010.

[153] Marcus Braun, Zdenek Lansky, Gero Fink, Felix Ruhnow, Stefan Diez, and Marcel Janson. Adaptive braking by Ase1 prevents overlapping microtubules from sliding completely apart. *Nature Cell Biology*, 13(10):1259–1264, 2011.

[154] Zdenek Lansky, Marcus Braun, Annemarie Lüdecke, Michael Schlierf, Pieter Rein ten Wolde, Marcel Janson, and Stefan Diez. Diffusible crosslinkers generate directed forces in microtubule networks. *Cell*, 160(6):1159–1168, 2015.

[155] Richard Neumann. The entropy of a single Gaussian macromolecule in a noninteracting solvent. *Journal of Chemical Physics*, 66:870–871, 1977.

[156] Richard M. Neumann. Entropic approach to Brownian movement. *American Journal of Physics*, 48:354–357, 1980.

[157] Gerhard Glatting, Roland Winkler, and Peter Reineker. Partition Function and Force Extension Relation for a Generalized Freely Jointed Chain. *Macromolecules* , 26:6085–6091, 1993.

[158] Nico Roos. Entropic forces in Brownian motion. *American Journal of Physics*, 82:1161–1166, 2014.

[159] Erik Verlinde. On the origin of gravity and the laws of Newton. *Journal of High Energy Physics*, 04:29, 2011.

[160] Tower Wang. Coulomb force as an entropic force. *Physical Review D, vol. 81, Issue 10, id. 104045*, 81:104045, may 2010.

[161] Jin-Ho Cho and Hyosung Kim. An entropic understanding of Coulomb force. *Journal of Physics: Conference Series*, 343:012024, 2012.

[162] Seyed Hendi and Ahmad Sheykhi. Entropic Corrections to Coulomb's Law. *International Journal of Theoretical Physics*, 51:1125–1136, apr 2012.

[163] Alexander Wissner-Gross and Cameron Freer. Causal Entropic Forces. *Physical Review Letters*, 110:168702, 2013.

[164] Archil Kobakhidze. Once more: gravity is not an entropic force. *arXiv*, 1108:4161, 2011.

[165] The Journal of Physiology. The potassium permeability of a giant nerve fibre. *Hodgkin, Alan and Keynes, Richard*, 128(1):61–88, 1955.

[166] Robert Macey and Robert Oliver. The Time Dependence of Single File Diffusion. *Biophysical Journal*, 7:545–554, 1967.

[167] Kwinten Nelissen, Veaceslav Misko, and Francois Peeters. Single-file diffusion of interacting particles in a one-dimensional channel. *Europhysics Letters*, 80:56004, 2007.

[168] Pavel Krapivsky, Kirone Mallick, and Tridib Sadhu. Large Deviations in Single-File Diffusion. *Physical Review Letters*, 113:078101, 2014.

[169] Sergey Aityan and V. I. Protnov. Analysis of Models of Single-File Diffusion. *General Physiology and Biophysics* , 7:591–611, 1988.

[170] Binhua Lin, Mati Meron, Bianxiao Cui, Stuart A. Rice, and Haim Diamant. From Random Walk to Single-File Diffusion. *Physical Review Letters*, 94:216001, 2005.

[171] Theodore Harris. Diffusion with "Collisions" between Particles. *Journal of Applied Probability*, 2:323–338, 1965.

[172] Henk van Beijeren, Klaus Kehr, and Ryszard Kutner. Diffusion in concentrated lattice gases. III. Tracer diffusion on a one-dimensional lattice. *Physical Review B*, 28:5711–5723, 1983.

[173] Donald Jepsen. Dynamics of a Simple Many-Body System of Hard Rods. *Journal of Mathematical Physics*, 6:405–413, 1965.

[174] Lewi Tonks. The Complete Equation of State of One, Two and Three-Dimensional Gases of Hard Elastic Spheres. *Physiccal Review*, 50(10):955–963, 1936.

[175] Salima Rafaï, Levan Jibuti, and Philippe Peyla. Effective Viscosity of Microswimmer Suspensions. *Physical Review Letters*, 104:098102, 2010.

[176] M. Cristina Marchetti, Jean-Francois Joanny, Sriram Ramaswamy, Tanniemola Liverpool, Jacques Prost, Madan Rao, and R. Aditi Simha. Hydrodynamics of soft active matter. *Reviews of Modern Physics*, 85:1143–1189, 2013.

[177] Joakim Stenhammar, Raphael Wittkowski, Davide Marenduzzo, and Michael Cates. Activity-Induced Phase Separation and Self-Assembly in Mixtures of Active and Passive Particles. *Physical Review Letters*, 114:018301, 2015.

[178] Alexander Grosberg and Jean-Francois Joanny. Activity induced phase separation. *Physical Review E*, 92:032118, 2015.

[179] Ran Ni, Martien Cohen Stuart, and Peter Bolhuis. Tunable Long Range Forces Mediated by Self-Propelled Colloidal Hard Spheres. *Physical Review Letters*, 114:018302, 2015.

[180] Megan Valentine, Polly Fordyce, and Steven Block. Eg5 steps it up! *Cell Division*, 1:31, 2006.

[181] Christina Thiede, Stefan Lakämper, Alok Weßel, Stefanie Reiter, and Christoph Schmidt. Tetrameric Chimera DK4mer is a Tool to Study Mechanisms Of Kinesin-5 Regulation. A Tetrameric Chimera of a Kinesin 1 and a Kinesin 5 is a Fast Microtubule Sliding Motor. *Biophysical Journal*, 98:165, 2010.

[182] Felix Ruhnow, David Zwicker, and Stefan Diez. Tracking Single Particles and Elongated Filaments with Nanometer Precision. *Biophysical Journal,*, 100:2820–2828, 2011.

[183] Samuel McCandlish, Aparna Baskaran, and Michael F. Hagan. Spontaneous segregation of self-propelled particles with different motilities. *Soft Matter*, 8:2527, n/a 2012.

[184] René Schneider, Till Korten, Wilhelm Walter, and Stefan Diez. Kinesin-1 Motors Can Circumvent Permanent Roadblocks by Side-Shifting to Neighboring Protofilaments. *Biophysical Journal*, 108:2249–2257, 2015.

[185] Karsten Kruse and Frank Jülicher. Self-organization and mechanical properties of active filament bundles. *Physical Review E*, 67:051913, 2003.

[186] Daniel Gillespie. General Method for Numerically Simulating the Stochastic Time Evolution of Coupled Chemical Reactions. *Journal of Computational Physics*, 22:403–434, 1976.

List of Figures

Acknowledgement

At the end of this thesis, it is my pleasure and privilege to thank all people, that have contributed in some way to this work.
First of all, I thank Karsten Kruse, who has been an excellent supervisor for many years and largely influenced my scientific work. Also I appreciate the contribution of the labs of Marcel Janson, Stefan Diez, and Gohta Goshima to my work, as they were all involved in some way in the project. Not to forget of course my dear colleagues at Saarland University.
Furthermore, I want to thank my parents Fredi and Rita, my sister Yvonne and her family, my girlfriend Sarah, and all of my friends who have always provided support and showed patience.
To come to an end, I thank the collaborative research center 1027 and the graduate school 1276 of Deutsche Forschungsgemeinschaft for funding.

Danksagung

Am Ende dieser Arbeit ist es mir sowohl eine Freude als auch Ehre, mich bei all jenen zu bedanken, die entweder direkt oder indirekt an der Entstehung meiner Doktorarbeit beteiligt waren.
Zuallererst möchte ich mich bei Karsten Kruse bedanken, der mir seit vielen Jahren als exzellenter Betreuer zur Seite steht. Ferner bin ich dankbar für die Beiträge der Arbeitsgruppen von Marcel Janson, Stefan Diez und Gohta Goshima, die in vielfältiger Weise an dem Projekt beteiligt waren. Nicht vergessen möchte ich natürlich meine hochgeschätzten Kollegen an der Universität des Saarlandes.
Darüberhinaus möchte ich mich bei meinen Eltern Fredi und Rita, meiner Schwester Yvonne und ihrer Familie, meiner Freundin Sarah sowie all meinen Freunden bedanken, die mir stets Unterstützung boten und Geduld entgegenbrachten.
Zu guter Letzt bedanke ich mich beim Sonderforschungsbereich 1027 sowie dem Graduiertenkolleg 1276 der Deutschen Forschungsgemeinschaft für finanzielle Unterstützung.